Dissertation

Role of lysosomal acid lipase in skeletal muscle formation, metabolism, and functions

submitted by

Akhmetshina Alena, BSc. MSc.

for the Academic Degree of

Doctor of Philosophy

(PhD)

at the

Medical University of Graz

Gottfried Schatz Research Center for Cell Signaling, Metabolism and Aging

Molecular Biology and Biochemistry

under the supervision of

Univ. Prof.in Mag.a Dr.in rer. nat.

Dagmar Kratky

2024

Statutory Declaration

I hereby declare that this thesis is my own original work and that I have fully acknowledged by name all of those individuals and organizations that have contributed to the research for this thesis. Due acknowledgement has been made in the text to all other material used. Throughout this thesis and in all related publications I followed the “Standards of Good Scientific Practice and Ombudsmen Committee at the Medical University of Graz.

Graz 30.04.2024

.....

Alena Akhmetshina

Disclosures

Please note that parts of this thesis have been published or are under preparation for future publications:

Loss of lysosomal acid lipase results in mitochondrial dysfunction and fiber switch in skeletal muscles of mice.

Akhmetshina, A., Bianco, V., Bradic, I., Korbelius, M., Pirchheim, A., Kuentzel, K. B., Eichmann, T. O., Hinteregger, H., Kolb, D., Habisch, H., Liesinger, L., Madl, T., Sattler, W., Radovic, B., Sedej, S., Birner-Gruenberger, R., Vujic, N., & Kratky, D. (2024). Loss of lysosomal acid lipase results in mitochondrial dysfunction and fiber switch in skeletal muscles of mice. Molecular Metabolism, 79, Article 101869. https://doi.org/10.1016/j.molmet.2023.101869

During my PhD, thesis I also contributed to the following publications:

1. Amor, M., Bianco, V., Buerger, M., Lechleitner, M., Vujić, N., Dobrijević, A., **Akhmetshina, A.**, Pirchheim, A., Schwarz, B., Pessentheiner, A. R., Baumgartner, F., Rampitsch, K., Schauer, S., Klobučar, I., Degoricija, V., Pregartner, G., Kummer, D., Svecla, M., Sommer, G., Kolb, D., Holzapfel, G. A., Hoefler, G., Frank, S., Norata, G. D., & Kratky, D. (2023). Genetic deletion of MMP12 ameliorates cardiometabolic disease by improving insulin sensitivity, systemic inflammation, and atherosclerotic features in mice. Cardiovascular Diabetology, 22(1), Article 327. https://doi.org/10.1186/s12933-023-02064-3

2. Bianco, V., Korbelius, M., Vujic, N., **Akhmetshina, A.**, Amor, M., Kolb, D., Pirchheim, A., Bradic, I., Kuentzel, K. B., Buerger, M., Schauer, S., Phan, H. T. T., Bulfon, D., Hoefler, G., Zimmermann, R., & Kratky, D. (2023). Impact of (intestinal) LAL deficiency on lipid metabolism and macrophage infiltration. Molecular Metabolism, 73, Article 101737. https://doi.org/10.1016/j.molmet.2023.101737

3. Nandy, A., Richards, A., Thapa, S., **Akhmetshina, A.**, Narayani, N., & Rendina-Ruedy, E. (2023). Altered osteoblast metabolism with aging results in lipid accumulation and oxidative stress mediated bone loss. Aging and Disease. Advance online publication. https://doi.org/10.14336/AD.2023.0510

4. Akhmetshina, A., Kratky, D., & Rendina-Ruedy, E. (2023). Influence of cholesterol on the regulation of osteoblast function. Metabolites, 13(4), Article 578. https://doi.org/10.3390/metabo13040578

5. Zhou, Q., Kerbl-Knapp, J., Zhang, F., Korbelius, M., Kuentzel, K. B., Vujić, N., **Akhmetshina, A.**, Hörl, G., Paar, M., Steyrer, E., Kratky, D., & Madl, T. (2021). Metabolomic profiles of mouse tissues reveal an interplay between aging and energy metabolism. Metabolites, 12(1), Article 17. https://doi.org/10.3390/metabo12010017

6. Zhou, Q., Zhang, F., Kerbl-Knapp, J., Korbelius, M., Kuentzel, K. B., Vujić, N., **Akhmetshina, A.**, Hörl, G., Paar, M., Steyrer, E., Kratky, D., & Madl, T. (2022). Phosphatidylethanolamine N-methyltransferase knockout modulates metabolic changes in aging mice. Biomolecules, 12(9), Article 1270. https://doi.org/10.3390/biom12091270

7. Helderman, R. C., Whitney, D. G., Duta-Mare, M., **Akhmetshina, A.**, Vujic, N., Jayapalan, S., Nyman, J. S., Misra, B. B., Rosen, C. J., Czech, M. P., Kratky, D., & Rendina-Ruedy, E. (2021). Loss of function of lysosomal acid lipase (LAL) profoundly impacts osteoblastogenesis and increases fracture risk in humans. Bone, 148, Article 115946. https://doi.org/10.1016/j.bone.2021.115946

8. Kuentzel, K. B., Bradić, I., **Akhmetshina, A.**, Korbelius, M., Rainer, S., Kolb, D., Gauster, M., Vujić, N., & Kratky, D. (2021). Defective lysosomal lipolysis causes prenatal lipid accumulation and exacerbates immediately after birth. International Journal of Molecular Sciences, 22(19), Article 1041. https://doi.org/10.3390/ijms22191041

9. Zhang, F., Kerbl-Knapp, J., **Akhmetshina, A.**, Korbelius, M., Kuentzel, K. B., Vujić, N., Hörl, G., Paar, M., Kratky, D., Steyrer, E., & Madl, T. (2021). Tissue-specific landscape of metabolic dysregulation during aging. Biomolecules, 11(2), Article 235. https://doi.org/10.3390/biom11020235

10. Zhang, F., Kerbl-Knapp, J., Rodriguez Colman, M. J., Meinitzer, A., Macher, T., Vujic, N., Fasching, S., Jany-Luig, E., Korbelius, M., Kuentzel, K. B., Mack, M., **Akhmetshina, A.**, Pirchheim, A., Paar, M., Rinner, B., Hörl, G., Steyrer, E., Stelzl, U., Burgering, B., Eisenberg, T., Pertschy, B., Kratky, D., & Madl, T. (2021). Global analysis of protein arginine methylation. Cell Reports Methods, 1(2), Article 100016. https://doi.org/10.1016/j.crmeth.2021.100016

Co-authors who contributed to this thesis and my publication:

Valentina Bianco[1], Ivan Bradić[1], Melanie Korbelius[1], Anita Pirchheim[1], Katharina B. Kuentzel[1,2], Thomas O. Eichmann[3,4,5], Helga Hinteregger[1], Dagmar Kolb[5,6,7], Hansjoerg Habisch[1], Laura Liesinger[8], Tobias Madl[1,5], Wolfgang Sattler[1], Branislav Radović[1], Simon Sedej[5,9,10], Ruth Birner-Gruenberger[5,8,11], Nemanja Vujić[1], Dagmar Kratky[1,5]

[1]Gottfried Schatz Research Center, Molecular Biology and Biochemistry, Medical University of Graz, Graz, Austria;

[2]present address: Department of Biomedical Science, University of Copenhagen, Copenhagen, Denmark;

[3]Institute of Molecular Biosciences, University of Graz, Graz, Austria;

[4]present address: Core Facility Mass Spectrometry, Center for Medical Research, Medical University of Graz, Graz, Austria;

[5]BioTechMed-Graz, Graz, Austria;

[6]Core Facility Ultrastructural Analysis, Medical University of Graz, Graz, Austria;

[7]Gottfried Schatz Research Center, Cell Biology, Histology and Embryology, Medical University of Graz, Graz, Austria;

[8]Institute of Chemical Technologies and Analytics, TU Wien, Vienna, Austria;

[9]Department of Internal Medicine, Division of Cardiology, Medical University of Graz, Graz, Austria.

[10]Institute of Physiology, University of Maribor, Slovenia

[11]Diagnostic and Research Institute of Pathology, Medical University of Graz, Graz, Austria;

Hereby I acknowledge the contribution of the following persons to my research work:

-Valentina Bianco, Melanie Korbelius, Katharina B. Kuentzel, and Nemanja Vujić: assistance with mouse work and radioactive experiments.

-Ivan Bradić, Laura Liesinger, and Ruth Birner-Gruenberger: performance and analysis of proteomics data.

-Anita Pirchheim: operation of the high-resolution Oxygraph-2k respirometer.

-Thomas O. Eichmann: analysis of acylcarnitines and ATP by mass spectrometry.

-Helga Hinteregger and Wolfgang Sattler: quantification of amino acids in plasma.

-Hansjoerg Habisch and Tobias Madl: metabolomic analysis by nuclear magnetic resonance.

-Dagmar Kolb: electron microscopy.

-Simon Sedej: assistance with peak effort testing experiments.

Additional co-authors who contributed to this thesis:

- ELISA measurement was performed by A. Ibovnik
- Assistance with experiments using Seahorse, during my research stay abroad was provided by Elizabeth Rendina-Ruedy and her team at Vanderbilt University Medical Center.

All co-authors were asked for permission to use their data in this thesis. Respondents provided written comments to the Medical University of Graz's research management unit, with their consent.

Acknowledgement

First of all, I would like strongly appreciate my supervisor, Dagmar Kratky. Thank you for your exceptional guidance and mentorship throughout my time in the research lab. Your support has been invaluable to me, and I am truly grateful for the opportunity to work under your supervision. From the moment I joined the lab, you welcomed me with open arms and provided me with the necessary guidance to navigate through the complexities of scientific research. Your expertise and insight have greatly enriched my understanding of lipid metabolism and muscle biology and I have grown both personally and professionally under your mentorship.

Furthermore, I would like to thank my dissertation committee members Günter Hämmerle and Gabriele Schoiswohl for their suggestions and comments. Thanks to Branislav Radovic for the ideas that formed the basis of my project and for the insightful discussions.

In addition, I would like to thank our collaborators, in particular Wolfgang Sattler, Helga Hinteregger, Dagmar Kolb, Dominique Pernitsch, Thomas O. Eichmann, Tobias Madl and his team, Ruth Birner-Grünberger and her team, Katharina Leitner and Simon Sedej for their assistance in experiments and helpful discussions.

I would also like to thank Elizabeth Rendina-Rudy for the opportunity to work with her team at Vanderbilt University Medical Center during my research stay abroad and to visit beautiful Nashville.

I would like to appreciate the funding institutions FWF and Medical University of Graz. Special thanks to the International Doctoral Program Metabolic and Cardiovascular Diseases (DK-MCD) and the Marshall Plan for financial support during my research stay abroad. Thanks to Karin Osibow for all her help and administration of student affairs.

Additionally, I want to thank all current and former members of the Kratky lab for their help and support. Thanks to Anton, Birgit, Irmi, Silvia, Jonas, Stefan, Ivan, Madeleine, Sarah, Laszlo, Suravi, Malena, Ariane, Vanessa, Martin for their moral and physical support in experiments and life. Thank you, Valentina, for being my lab buddy all this time. I would like to thank Nemo for his scientific ideas and suggested experiments. I deeply appreciate Melly, Kati, Anita, and Meli for their responsiveness and help in the most difficult experiments. And thank you all, guys, for your patience and encouragement during challenging times.

Special thanks to my parents for always being on my side and believing in me. Thanks to my partner Barny, without you I wouldn't have even considered pursuing a PhD.

Table of Contents

Abbreviations and Definitions

4E-BP1 eukaryotic translation initiation factor 4E-binding protein 1
4-MU 4-methylumbelliferone esters
A-KG α-ketoglutarate
A1AG alpha-1-acid glycoprotein
AA amino acid
ACAT acetyl-coenzyme A acetyltransferase
ACBD6 acyl- coenzyme A -binding domain-containing protein 6
ActR activin type receptors
ACS acyl- coenzyme A synthetases
ACSL1 acyl- coenzyme A synthetase long chain family member 1
ADP adenosine diphosphate
AIDS acquired immunodeficiency syndrome
Akt protein kinase B
Ala alanine
ALK anaplastic lymphoma kinase
AMP adenosine monophosphate
AMPK AMP-activated (dependent) protein kinase
ATPD ATP synthase subunit delta, mitochondrial
Atg autophagy-related
ATGL adipose triglyceride lipase
ATP adenosine triphosphate
BAT brown adipose tissue
BCAA branch chained amino acids
BCAT2 branched-chain aminotransferase 2
BCKDC branched-chain α ketoacid dehydrogenase complex
BMP bone morphogenetic proteins
BW body weight
CATS cathepsin S
CE cholesteryl ester
CERU ceruloplasmin
CESD cholesteryl ester storage disease
CGI-58 comparative gene identification-58
CHREBP carbohydrate responsive element binding protein

CK creatine kinase

CoA coenzyme A

CO3A collagen alpha-1(III) chain

COA7 cytochrome c oxidase assembly factor 7

COX5A cytochrome c oxidase subunit 5A, mitochondrial

CPT1 carnitine palmitoyl acyl-CoA transferase 1

DG diacylglycerol

EDL extensor digitorum longus

ELC essential light chain

ER endoplasmic reticulum

ERK1 extracellular signal-regulated kinase 1

ERT enzyme replacement therapy

FA fatty acid

FABP fatty acid binding protein

FAO FA oxidation

FAT/CD36 caveolins fatty acid translocase

FATP fatty acid transporters

FAS fatty acid synthase

FC free cholesterol

FG free glycerol

FGF ffibroblast growth factors

FoxO1 forkhead box protein O1

G-1-P glucose-1-phosphate

G-6-P glucose 6-phosphate

GA gastrocnemius

GAPDH glyceraldehyde 3-phosphate dehydrogenase

Gln glutamine

Glu glutamic acid

GLUT glucose transporter

Gly glycine

GO gene ontology

GS2 gene sequence 2

H&E hematoxylin and eosin staining

HDAC histone deacetylase

HDL high-density lipoprotein

HFABP heart FA Binding Proteins
HFHC high fat/high cholesterol
HIF2α hypoxia-inducible factor 2 α
HK hexokinase
HMG-CoA 3-hydroxy-3-methyl-glutaryl-coenzyme A
HSL hormone sensitive lipase
IGF1 insulin-like growth factor 1
IGF1R insulin-like growth factor 1 receptor
KB ketone body
KCRS creatine kinase S-type, mitochondrial
LC-MS/MS liquid chromatography-tandem mass spectrometry
IL-6 interleukin-6
Ile Isoleucine
LAL lysosomal acid lipase
Lal-/- LAL knockout
LAL-D lysosomal acid lipase deficiency
LCAT lecithin-cholesterol acyltransferase
LCFA very long-chain FA
LD lipid droplet
LDL low-density lipoprotein
LDLR low-density lipoprotein receptor
LSD lysosomal storage diseases
MAFbx F-box only protein 32
MCP1 monocyte chemoattractant protein 1
MCSF macrophage colony stimulating factor
MDH malate dehydrogenase
MEF2 myocyte enhancer factor 2
MG monoglyceride
MGL monoglyceride lipase
MLC myosin light chain
MRI magnetic resonance imaging
mTOR mechanistic target of rapamycin
MTP microsomal triglyceride transfer protein
MYH myosin heavy chain (gene)
MyHC myosin heavy chain

NADH nicotine amide dinucleotide

NAFLD non-alcoholic fatty liver disease

NFAT nuclear factor of activated T-cells

NMR nuclear magnetic resonance

NPC1L1 Niemann-Pick C1-like 1

NDUF2 NADH dehydrogenase [ubiquinone] 1 alpha subcomplex assembly factor 2

ORO Oil Red O

PA palmitic acid

PC phosphatidylcholine

PCA principle component analysis

pCr phosphocreatine

PCX pyruvate carboxylase

PDH pyruvate dehydrogenase

PEP phosphoenolpyruvate

PEPCK phosphoenolpyruvate carboxykinase

PGC1α peroxisome proliferator-activated receptor gamma coactivator 1-alpha

PFK phosphofructokinase

PI phosphatidylinositol

PI3K phosphoinositide-3-kinase

PKA protein kinase A

PL phospholipid

PNPLA phospholipase domain containing

PPARα peroxisome proliferator-activated receptor alpha

PPT1 palmitoyl-protein thioesteras 1

PYGL glycogen phosphorylase

qPCR quantitative polymerase chain reaction

QU quadriceps

RE retinyl ester

RLC regulatorily light chain

ROS reactive oxygen species

SIRT sirtuin

SM skeletal muscle

SO soleus

TA tibias anterior

TC total cholesterol

TCA tricarboxylic acid cycle

TFEB transcription factor EB

TG triglyceride

TGFβ transforming growth factor-beta

TNN troponin

TRAF tumor necrosis factor (α) receptor adaptor protein

TRIM tripartite motif-containing

TNFα tumor necrosis factor alpha

ULK unc-51-like autophagy-activating kinases

Val valine

VPS vacuolar protein sorting

WAT white adipose tissue

WD Wolman disease

Wt wild type

Zusammenfassung

Abstract

Lysosomal acid lipase (LAL) hydrolyzes triglycerides (TG) and cholesteryl esters (CE) within lysosomes of multiple cells and tissues at an acidic pH. Despite a number of studies dealing with lysosomal function in skeletal muscle (SM), lipid hydrolysis by LAL in lysosomes of SM has not been well characterized. Recent data suggested that LAL may play an important role in SM development, function, and metabolism as a result of impaired lipid and/or carbohydrate metabolism.

SM mass, cross-sectional area, and the Feret diameter were markedly lower in mice with systemic LAL deficiency (Lal-/-), despite no evidence of proteolysis or impaired protein synthesis in all SM examined. In addition, we observed elevated CE concentration and impaired metabolic profile in all investigated SM samples, especially during fasting. Untargeted proteomic profiling of oxidative and glycolytic fibers of SM revealed upregulation of proteins associated with the transition between fast and slow fibers. In addition, we found significantly increased MyHCI expression in Lal-/- SM, which is specific for slow oxidative fibers. Gene ontology enrichment analysis indicated reduced mitochondrial function and impaired organization, particularly affecting oxidative phosphorylation, in Lal-/- SM, consistent with decreased oxidative capacity and ATP concentration.

Similar to our mouse model, C2C12 myoblasts treated with the LAL inhibitor Lalistat-2 and primary myoblasts isolated from Lal-/- mice in complete growth medium showed increased levels of CE. Myofiber formation, however, was comparable in both in vitro models studied. Moreover, we were unable to detect any changes in mitochondrial function upon Lalistat-2 treatment of C2C12 cells or primary myoblasts derived from Lal-/-.

Taken together, loss of LAL is associated with increased expression of slow oxidative fibers in SM, impaired mitochondrial function and muscle metabolism, but only in knockout mice *in vivo* and not *ex vivo*. The aforementioned changes, with the exception of increased CE levels, were not confirmed in the studied cell models with reduced LAL activity. The differences we found between *in vivo* and *ex vivo*/*in vitro* models are possibly related to nutrient unavailability and systemic inflammation in Lal-/- mice.

1. Introduction

1.1 Skeletal muscle: an overview

Skeletal muscle (SM) tissue exceeds any other tissue of the organism by its mass and is the most widespread type of muscle tissue of the human body. SM are responsible for the large number of vital functions in the body. They put bones in motion, actively change the position of the body in space, participate in the formation of the oral and abdominal cavity, chest, and pelvis, are part of the walls of the pharynx, the upper part of the esophagus, larynx, they carry out movements of the eyeball and auditory ossicles, respiratory and swallowing movements (1). There are about 600 muscles in the human body, most of which are paired. The mass of SM in an adult human reaches 30-40% of body weight. In old age, the mass of muscle tissue typically does not exceed 20-30% (2). SM consist of bundles of cylindrical, multinucleated muscle fibers, each with a diameter of 0.05-0.11 mm, held together by a system of connective tissue components. Specifically, the bundles of fibers of various sizes are surrounded and separated from each other by thin layers of connective tissue, which form the inner perimysium (1). Between the muscle fibers, there is a thin network of small blood vessels (capillaries) and nerves (approximately 10% of the total muscle mass) (3).

Myofibrils are the striated organelles within muscle cells (muscle fibers) that consist of repeating segments of sarcomeres aligned end to end, giving the muscles their striated appearance and allowing for coordinated contractions necessary for movement (4). The number of myofibrils varies enormously, ranging from several dozens to 2000 or more. Sarcomeres are the smallest functional units of the myofibrils and are made up of a precise arrangement of myosin (thick) and actin (thin) filaments (Fig. 1).

When examining muscle fibers under a light microscope, transverse striation can be observed, which are alternating dark and light areas known as disks. While dark disks are characterized by double optical refraction and are called anisotropic disks or A-discs (A-bands), light disks do not have double refraction and thus are called isotropic or I-discs (I-bands). Specifically, the A-discs are composed of the thick filaments, and the I-discs are formed from the thin filaments. The elastic filament in the sarcomere is primarily composed of the protein titin (connectin), which runs from the Z-disc to the M-line. Moreover, the A-disc contains a lighter area in the middle known as the H-zone with a darker M-line, the mesofragment. The M-line serves as the attachment site for the thick filaments and helps to maintain the precise alignment of the myosin filaments in the sarcomere. The central part of the I-disk is described as the telofragment or Z- disc (or line), which is built of fibrillar protein molecules (5). The Z-disc

serves as an attachment point for neighboring myofibrils using the desmin protein, assuring that all lines and Z-discs on neighboring myofibrils are aligned (6).

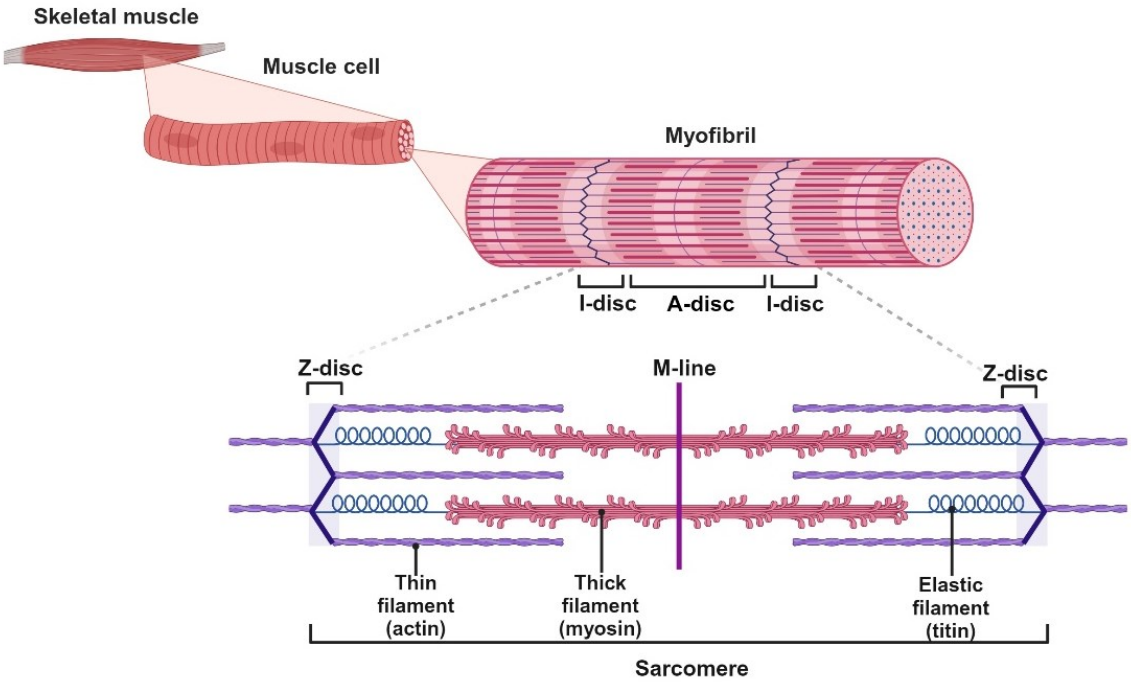

Figure 1: Structure of the sarcomere.
The structural unit of the myofibril is the sarcomere, the area between the two Z-discs. It is composed of thick, myosin-containing filaments, which are surrounded and interwoven with thin, actin-containing filaments. Created with Biorender.com.

1.2 Molecular physiology of myosin

Myosin is a molecular motor protein that plays a crucial role in muscle contraction and movement by hydrolyzing adenosine triphosphate (ATP). It is composed of two heavy chains (MyHC) and two pairs of myosin light chains (MLC), one of which is named essential (ELC) and the other one being the regulatory light chain (RLC) (Fig. 2).

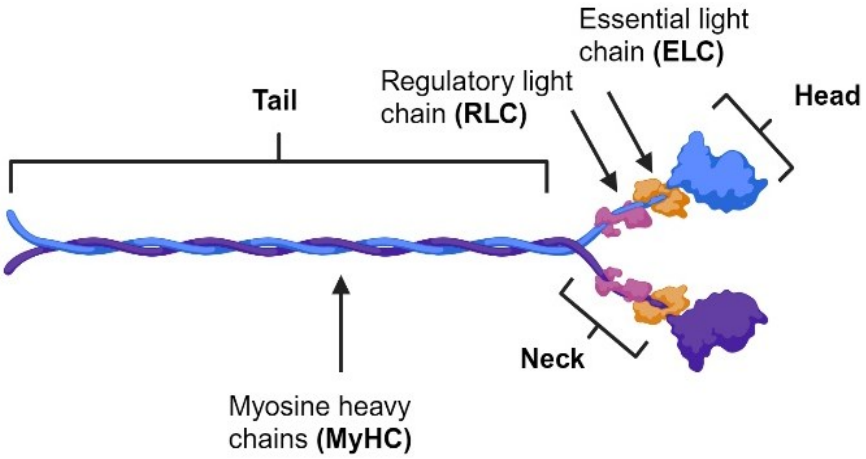

Figure 2: Schematic representation of the structure of muscle myosin.
Myosin consists of two heavy chains (MyHC) with intertwined tail domains (rods), a neck region, and globular catalytic heads. The essential (ELC) and regulatory (RLC) light chains are linked to the neck region of each MyHC. Created with BioRender.com.

The C-terminal ends of the MyHC intertwine to form a coiled-coil tail that acts as a backbone of the myosin filament. At the other end of the MyHC, the N-terminal region folds into a globular head, which contains the active sites for actin binding. The region connecting the globular head to the myosin tail is known as the neck region, commonly referred to as the lever arm (7, 8). Myosin acts like an actin-dependent ATPase. Each cycle involves ATP hydrolysis and a consequent increase in free energy, ensuring movement in one direction only, towards the plus-end of actin (9). Initially, the myosin head binds to ATP, hydrolyzing it into ADP and inorganic phosphate while remaining bound. Subsequently, it weakly binds also to an adjacent actin subunit, eliciting phosphate release and leading to a strong myosin-actin binding interaction. Following this, the myosin head undergoes a structural change that brings the thick filament closer to the free ends of thin filaments. Afterwards, ADP is released, causing detachment of the myosin head from the actin filament and allowing a new ATP molecule to bind. This cycle repeats until the concentration of calcium ions decreases or until ATP reserves are depleted, such as during cell death. Given the abundance of myosin molecules within the myosin filament, hundreds of myosin heads engage in synchronized activity, which leads to rapid and powerful muscle contractions (10, 11). Notably, the myosin type responsible for producing muscle contraction in SM in most animal cell types is myosin II or conventional myosin (12).

1.3 Myosin isoforms in SM

SM is composed of various fiber types, each expressing specific MyHC isoforms that determine their specific functional properties, including contractile speed and endurance. Scientists have been studying muscle fibers for more than a century and have revealed that muscle fibers are arranged in a mosaic pattern (13). Historically, the predominant MHC isoforms in SM are classified into two major types based on their functional speed and color: slow-twitch fibers (white) and fast-twitch fibers (red) (14). Fast fibers and slow fibers in SM are largely distinguished by their maximum rate of shortening, or contraction velocity, which is based on the activity of myosin ATPase (15). Alternatively, muscle fibers can be classified based on the main pathway of ATP formation, leading to their categorization as either oxidative or glycolytic fibers. Slow muscle fibers are equipped with a high number of mitochondria. The mitochondria contain enzymes that are crucial for the oxidation of both carbohydrates and fatty acids (FA), which enables these fibers to sustain long periods of activity. The mitochondrial content in these fibers allows for efficient aerobic respiration, essentially the use of oxygen to generate ATP through the breakdown of nutrients. Since this process requires a large amount of oxygen, the network of capillaries that surround slow muscle fibers is more developed and the oxygen supply delivered within the blood flow is more intense. These fibers have a limited supply of carbohydrates in the form of glycogen and low activity of glycolytic enzymes (16, 17). From the other hand, fast-twitch muscle fibers are characterized by their ability to contract quickly. They generate a high rate of force in a short period and have a well-developed and densely packed sarcoplasmic reticulum to facilitate rapid Ca^{2+} release and uptake. This allows for quicker and more powerful contractions compared to slow-twitch fibers (18, 19). Fast fibers can indeed be categorized as either oxidative or glycolytic based on their primary metabolic processes.

However, recent studies confirmed a more complex scenario regarding mitochondria in different SM fibers. It was established that mitochondria differ not only quantitatively but also qualitatively, with different subsets of mitochondrial proteins exhibiting fiber type-specific patterns of metabolic function (20, 21).

Over last 40 years, the concept of the diversity of muscle fiber types has evolved rapidly, leading to the identification of four major fiber types in adult mammalian SM: type I - “slow”; type IIA - “fast”; type IId/x - “fast”; and the “fastest” one, type IIB (19). Type IIB MyHC is not typically expressed in human SM. Some publications refer to it as a rodent type (22). The classification and comparison of different fibers types are shown in Table 1.

Table 1. Comparison of muscle fibers of different types.

	Type I	Type IIA	Type IId/x	Type IIB
Physical activity	Aerobic	Long-term anaerobic	Short-term anaerobic	Short-term anaerobic
Motoneuron size	Small	Medium	Large	Very large
Anatomical colors	Red	Red	White	White
Myosin ATPase activity	Slow	Fast	Fast	Fast
Sarcoplasmic reticulum	Poorly developed	Moderately developed	Well developed	Well developed
Capillary density	High	Intermediate	Low	Low
Quantity of myoglobin	High	Medium	Low	Low
Number of mitochondria	High	High	Medium	Low
Activity of mitochondrial enzymes	High	High	Low	Low
Resistance to fatigue	High	Fairly high	Intermediate	Low
Glycogen reserves	Low	Intermediate	High	High
Glycolytic capacity	Low	High	High	High
Contraction time/fatiguability	Slow	Medium	Fast	Very fast
Cross-sectional area of a muscle fiber	Small	Intermediate	High	High
Predominant type of MyHC (gene)	*MYH7*	*MYH2*	*MYH1*	*MYH4*
Predominant type of MyHC (protein)	MyHC-1	MyHC-2A	MyHC-2X	MyHC-2B

Hybrid muscle fibers contain two or more different types of MyHC isoforms. These fibers exhibit characteristics that are intermediate between the pure fiber types, allowing a more versatile range of muscle performance within a single muscle fiber. The combinations of MyHC isoforms such as MyHC-1+MyHC-2A, MyHC-2A + MyHC-2X, or MyHC-2X + MyHC-2B are indicative of a muscle's adaptive response to various stimuli or demands placed on it (23). Furthermore, specific MyHC isoforms such as MyHC-emb (embryonal, encoded by *Myh3*) can also be expressed in growing muscles, making them a valuable indicator for rejuvenating fibers (19).
The distribution of specific MyHC isoforms within SM varies among species. In humans, the *soleus* muscle (SO) is typically rich in type I (slow-twitch) fibers (22, 24) as well as in rats (25). On the other hand, in C57BL/6J mice, SO has a higher proportion of the IIa MyHC isoform, which is indicative of a fast-twitch fiber type that maintains a comparatively high oxidative capacity and fatigue resistance (26). In both mice and rats, the *extensor digitorum longus* (EDL), the *tibialis anterior* (TA), and the *gastrocnemius* (GA) are composed predominantly of fast-twitch fibers, specifically types IIB and IId/x (26).
Understanding these differences is crucial when interpreting the results of animal studies and when considering the translatability of these findings to human conditions. It also reflects the adaptability and plasticity of muscle tissue in response to a variety of factors, including evolutionary pressures, physical activity, and the environmental conditions.

1.4 Mechanisms of myosin phenotype remodeling in muscle fibers

Mature SM fibers have a stable myosin phenotype, which under certain conditions may exhibit plasticity and be altered in response to various stimuli. Factors triggering changes in MyHC isoform expression, thereby prompting a switch between slow and fast fibers, include neuromuscular activity, physical activity, aging, and diverse pathological conditions. For instance, alterations in neural stimulation patterns, such as heightened neuromuscular activity resulting from the chronic low-frequency stimulation, are associated with a shift from fast to slow MyHC isoforms (15, 27-29). In contrast, the stretch-overload model induced by SM immobilization in a lengthened position does not necessarily elevate neuromuscular activity but rather leads to an increase in the proportion of slow fibers (15, 30).
Hormones are also implicated in the shaping of the muscle fiber myosin phenotype. For instance, hypothyroidism tends to induce a shift from fast-twitch to slow-twitch fibers, thereby enhancing endurance capacity (31-33). Conversely, hyperthyroidism can lead to a transition from slow to fast fibers, which could decrease endurance performance but increase speed and power (15, 31-33). Moreover, testosterone is known to influence muscle hypertrophy and fiber

distribution and proportion. These effects have been confirmed across various species, including guinea pigs (34, 35), frogs (36), rabbits (37), and rats (38, 39). The anabolic effects of testosterone influence the satellite cells in SM, crucial for muscle repair and growth, and module various signaling pathways, including the protein kinase B or Akt/mechanistic target of rapamycin (mTOR) pathway involved in protein synthesis (40, 41). Consequently, it leads to an increase in the proportion of fast-twitch fibers (like type II), which are responsible for generating power and strength.

Aging is often associated with muscle atrophy, which is characterized by decreased muscle mass and a transition from fast-twitch to slow-twitch muscle fibers (42-44). In certain pathological conditions, atrophy occurs preferentially in specific fiber types and/or is accompanied by changes in the fiber type profile. Fasting (45), type 1 diabetes (46), sepsis (47), cancer- (48) and AIDS- associated cachexia (49) are associated with a transition from fast to slow fibers. Conversely, a reduction in neurological impact and mechanical strain, such as spinal cord injury (50), limb immobilization, and suspension (51), may result in a fiber type shift from slow to fast. In chronic heart failure and chronic obstructive pulmonary disease, changes in muscle fiber composition have also been observed, characterized by a shift from slow-twitch to fast-twitch fibers. This change could be attributed to several factors, including long-term medication use, systemic inflammation, hypoxia (i.e., low blood oxygen levels), and physical inactivity due to respiratory limitations (52).

Lastly, several studies have shown that exposure to microgravity induces changes in myofiber types. In mice and rats, microgravity-induced atrophy led to a shift in myofiber types, affecting those enriched in slow-type fiber SO (53, 54). Importantly, these transitions do not occur abruptly but rather progress gradually through a systematic sequence of MyHC isoform expression. Consequently, individual muscle fibers possess the capacity to express intermediate characteristics during their transition, frequently leading to the formation of hybrid fibers(15, 29).

The remodeling of the myosin phenotype of muscle fibers is a multifaceted process involving intricate mechanisms related to signaling, regulation of gene expression, and metabolic pathways (29). AMP-dependent protein kinase (AMPK) serves as a critical regulator of cellular energy balance and plays a pivotal role in influencing the activity of proteins and transcription factors associated with muscle metabolism. Activation of AMPK leads to phosphorylation of the histone deacetylases HDAC4 and HDAC5, which subsequently promotes the expression of the slow MyHC isoform and other genes involved in oxidative metabolism. This regulatory cascade underscores the link between cellular energy status and the expression of specific myosin isoforms. Moreover, various signaling pathways also affect muscle phenotype through

the regulation of fiber energy homeostasis. For example, activation of the mTORC1 pathway stimulates aerobic glycolysis in muscles fibers, thereby influencing the dynamic balance between glycolytic and oxidative metabolism (55).

Slow-twitch muscle fibers are characterized by high endurance, and their activity is associated with sustained levels of Ca^{2+} in the myoplasm and a lower content of energy-rich phosphates compared to fast-twitch fibers (19, 56). The calcineurin/nuclear factor of activated T-cells (NFAT) signaling pathway plays a key role in the regulation of gene expression in slow-twitch fibers, particularly for the slow MyHC isoforms (57-59). When activated by the Ca^{2+}-calmodulin complex, calcineurin dephosphorylates NFAT, which then translocates into the nucleus and initiates the transcription of slow MyHC genes, among others (13). This cascade is critical for the maintenance and adaptation of muscle fiber characteristics, especially under conditions of chronic activity.

In response to physical activity, the peroxisome proliferator-activated receptor-gamma coactivator 1 α (PGC-1α) serves as an essential regulator of SM gene expression programs just as hypoxia-inducible factor 2 α (HIF2α) does in primary myotubes by increasing the expression of genes linked to slow-twitch muscle fibers (60). In addition, an overexpression of the transcription factor forkhead box protein O1 (FoxO1) results in reduced muscle mass and a decrease in both slow and fast fiber types in transgenic mice, implicating muscle fiber degradation (61). Particularly, FoxO1 activation leads to a reduction in type I fiber-related genes and anti-fatigue characteristics, with higher expression of FoxO1 observed in fast-twitch fibers (62-64). Endurance training has been shown to induce a fast-to-slow fiber type transition and is associated with decreased FoxO1 expression, which may indicate that FoxO1 suppresses type I and supports fast-twitch fiber development (62). However, conditional deletion of FoxO1 has an opposite effect, as it decreases slow-twitch fibers and increases fast-twitch fibers, suggesting a complex relationship between FoxO1 and muscle fiber type composition (65).

Another important mechanism that contributes to the modulation of the MyHC phenotype is the involvement of microRNA (miR)-mediated pathways. In the heart, the *Myh6* gene, responsible for encoding a fast fiber-associated myosin, is co-expressed with miR-208a. This miR regulates the expression of two myosin isoforms specific for slow fibers along with their intronic miRs: Myh7/miR-208b and Myh7b/miR-499, respectively. Both miR-208b and miR-499 play overlapping roles in determining muscle fiber identity by activating slow and suppressing fast myofiber gene transcription programs (66, 67). The overexpression of miR-30e in C2C12 cells (immortalized mouse myoblast cell line) resulted in a significant decrease in *Pgc1α* levels

and increased specific MyHCII gene expression. This suggests that miR-30e is functionally associated with the formation of glycolytic myofibers (68).
Further studies and a deeper understanding of these mechanisms are paramount to unravel the complexity of the myosin phenotype of muscle fiber remodeling and its effects on muscle function and performance.

1.5 SM energy metabolism

SM contraction is a high energy-demanding function, which is based on its ability to store and regenerate ATP. To maintain an efficient contractile function in the SM, ATP levels should remain within a constant range between 2 and 5 mmol/kg (69). Therefore, ATP must be constantly replenished during muscle activity at the same rate at which it is utilized. The fast restoration of ATP is the result of degradation of the intramuscular store phosphocreatine (pCr) and glycogen. Medium-term supply is provided by anaerobic glycolysis, which converts glucose to ATP in the absence of oxygen; long-term supply is provided by oxidative phosphorylation, which converts glucose and FA to ATP with the consumption of oxygen, ultimately producing water and carbon dioxide as byproducts (70, 71).
The pCr reaction refers to the reversible enzymatic process by which energy is stored and released in muscle cells to meet their immediate energy needs. This reaction is catalyzed by the enzyme creatine kinase (CK) and occurs as follows: pCr + ADP ⇌ creatine + ATP.
When ATP (adenosine triphosphate) levels are high and the demand for energy is low, CK catalyzes the transfer of a phosphate group from ATP to creatine, generating pCr and ADP (72): ATP + creatine ⇌ ADP + phosphocreatine.
pCr stores have a limited capacity and can only fuel muscle contractions for 5 to 8 s (71). The volume of pCr in SM is 5 times lower than that of glycogen. Glycogen is actively catabolized during muscle contractions to generate the necessary ATP, resulting in the formation of lactate and hydrogen ions. Indeed, during high-intensity, short-duration activities such as sprinting or powerlifting, the primary source of ATP is the anaerobic breakdown of pCr and muscle glycogen (73, 74).

1.5.1 Carbohydrate energy metabolism in SM

The first studies linking carbohydrate metabolism and SM function were conducted in the 1920s. They showed that carbohydrates are necessary for SM functions and that blood glucose concentrations correlate with fatigue during a marathon (75).

SM play a key role in glucose metabolism and are critical for the clearance of glucose from the bloodstream, especially during the postprandial periods via insulin-dependent mechanisms. Following a meal, blood glucose levels rise, causing the release of insulin. Insulin induces glucose uptake into the SM, accounting for more than 80% of glucose clearance following an oral glucose load (76-78). Glucose transport across cell membranes is facilitated by various proteins of the SLC2A family, with over 14 different types identified in human cells (79). In SM, GLUT4, GLUT1, and GLUT3 play a crucial role in glucose uptake, with GLUT4 being the most prevalent (80). While GLUT1 is located on the plasma membrane, GLUT4 is mainly found in intracellular vesicles and translocates to the cell surface upon stimulation (81). Additionally, in SM, GLUT5-mediated fructose uptake can also contribute to the muscle's energy supply, particularly under conditions where glucose uptake is compromised or during periods when fructose is available from the diet (82). GLUT4 is an insulin-regulated glucose transporter highly expressed in SM and adipose tissue. Therefore, its intracellular localization under basal conditions limits glucose transport. However, upon stimulation by insulin or exercise, GLUT4 translocates to the plasma membrane, facilitating enhanced glucose uptake (81).

Glycolysis is a catabolic process that breaks down glucose in the cytoplasm of the cell (Fig.3). Under aerobic conditions, pyruvate, the final glycolysis product, is converted into acetyl-CoA. At rest, glycolysis provides almost half of the acetyl-CoA that enters the tricarboxylic acid (TCA) cycle within SM (72).

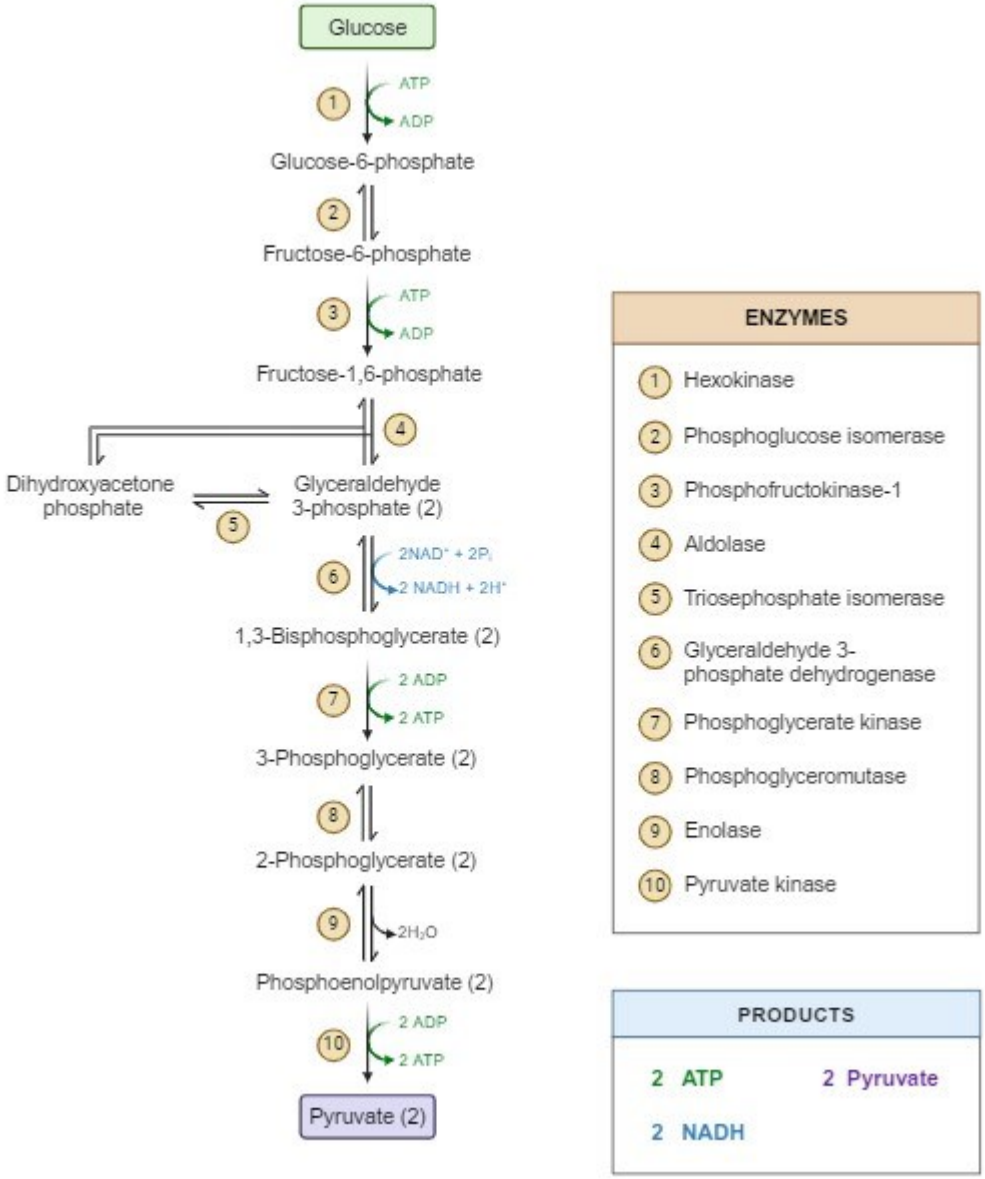

Figure 3: Glycolysis and glycolytic enzymes.
The process comprises a sequence of enzymatic reactions, starting with the phosphorylation of glucose to form glucose-6-phosphate, followed by subsequent transformations leading to the production of two molecules of pyruvate. Glycolysis generates ATP and NADH, providing cells with energy and reducing power. Additionally, key regulatory enzymes such as hexokinase, phosphofructokinase, and pyruvate kinase tightly control the flux through the pathway. Created with Biorender.com

Anaerobic glycolysis can quickly generate ATP from the breakdown of glucose to pyruvate, which is then converted to lactate by lactate dehydrogenase (LDH) (72, 83). Although this process can produce ATP rapidly, it is less efficient than aerobic glycolysis in terms of ATP yield per molecule of glucose. However, the conversion of pyruvate to lactate enables

glycolysis to continue by regenerating NAD^+, which is needed for one of the early steps in the glycolysis pathway.

The accumulation of lactate released during anaerobic glycolysis results in a subsequent drop of the SM pH. The decrease in intracellular pH inhibits key glycolytic enzymes, such as phosphofructokinase. This inhibition restricts ATP production rates, contributing to muscle fatigue and influencing both the intensity and duration of exercise. Lactate was classically viewed as a waste product, however nowadays, its role in gluconeogenesis, oxidative phosphorylation, and even in the regulation of gene expression has been accented (84, 85).

1.5.2 Lipid metabolism in SM

In addition to glucose, lipids represent an important source of fuel for SM, especially during prolonged exercise or low-intensity activities. Lipid metabolism involves the storage, breakdown, and utilization of lipids for energy production. The regulation of lipid metabolism in SM is influenced by various factors, such as exercise, diet, and hormonal signaling. The transport of FA from the bloodstream into SM fibers involves various proteins:

1. FA binding proteins (FABP) (86) and FA transport proteins (FATP) (87): assist in the solubilization and transport of FA across the cell membrane. Their expression and activity are regulated by the action of insulin, which facilitates glucose and FA uptake and thereby SM contractions, which can enhance nutrient delivery to active muscles (88, 89). Specific isoforms of FATPs, such as FATP1, FATP4, and FATP6, are expressed in SM, where they may serve dual roles in FA transport and activation (via esterification to CoA) (90). Among the FABP proteins, the predominant isoform in SM is FABP3 (also known as heart isoform, HFABP) (91). FABP4, which was previously reported as adipose tissue specific (92), was found to be highly expressed in SM during high-intensity aerobic training (93). While these proteins contribute to FA uptake, their exact roles and the significance of their enzymatic functions in muscle are continually being studied.
2. FA translocase/CD36: is a transmembrane glycoprotein that plays a critical role in the uptake of long-chain FA (94). During muscle contractions, CD36 translocates from intracellular pools to the cell surface, increasing its capacity to facilitate FA uptake into muscle fibers (89). High-fat diets can also upregulate CD36 expression, potentially as an adaptive response to increased FA availability (95).

An excessive amount of lipid uptake over its oxidation rate in SM fibers can lead to its accumulation and ultimately induce lipotoxic stress (96, 97). This excess manifests as intermuscular ectopic adipose tissue, which is associated with aging, weakened muscle strength, and decreased insulin sensitivity in SM. Intramyocellular lipids (IMCL) consist of triglycerides (TG) and other lipids like diglyceride (DG) and ceramides (98). Interestingly, IMCL are not exclusively linked to obesity. For instance, they have been observed in women without signs of obesity (99), as well as in endurance athletes who were even able to maintain insulin sensitivity, a scenario termed the "athlete's paradox" (100, 101). While increased lipid intermediates such as DG and ceramides typically correlate with impaired insulin response in SM (102-104), paradoxically, higher DG levels are found in trained athletes and are associated with improved insulin sensitivity. This indicates that the presence of these lipids does not always predict insulin signaling problems (105).

The breakdown of stored lipids under neutral conditions (specifically TG) occurs mainly through the action of three key enzymes: adipose triglyceride lipase (ATGL), hormone-sensitive lipase (HSL), and monoacylglycerol lipase (MGL) (106) (Fig. 4).

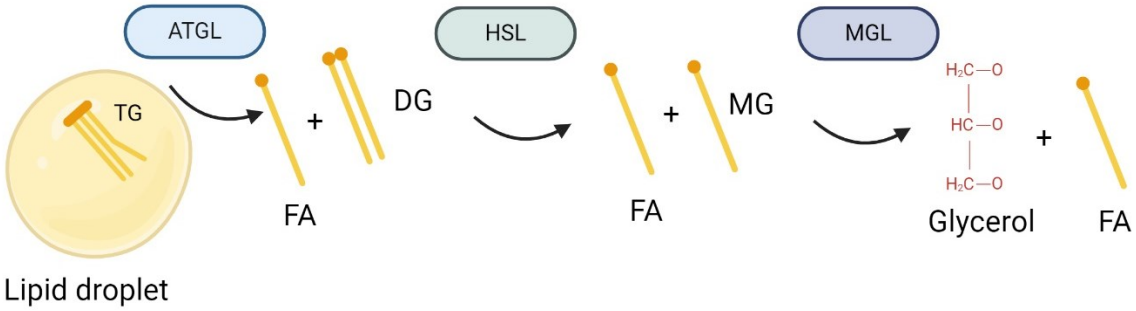

Figure 4: Schematic representation of neutral lipolysis.
This figure illustrates the enzymatic breakdown of stored triglycerides (TG) within cytosolic lipid droplets. The process of neutral lipolysis consists of a cascade of reactions catalyzed by a series of lipases. Adipose triglyceride lipase (ATGL) mediates the initial step, hydrolyzing TG into diglycerides (DG) and releasing a free fatty acid (FA). Subsequently, hormone-sensitive lipase (HSL) further breaks down DG into monoglycerides (MG) and another FA. The final step of the lipolytic pathway is catalyzed by monoacylglyceride lipase (MGL), which breaks down MG into glycerol and the final FA. Created with Biorender.com.

ATGL initiates TG breakdown to DG and FA, while demonstrating transacylation activity by forming TG and monoglyceride (MG) from two DG molecules (107-109). Loss-of-function mutations in the patatin-like phospholipase domain-containing 2 (*PNPLA2)* gene encoding ATGL in humans result in neutral lipid storage disease with myopathy (NLSDM), leading to steatosis development in various tissues, including SM and cardiac muscle (110). In mice,

ATGL deficiency replicates many clinical findings of NLSDM, emphasizing its critical role not only in different adipose tissue depots but also in vital energy-consuming organs like the heart (111, 112). Conversely, ATGL upregulation enhances TG catabolism, may increase mitochondrial biogenesis and subsequently SM oxidative capacity (113, 114). Interestingly, the expression of ATGL increases in response to endurance training, especially in type I fibers (115). Comparative gene identification-58 (CGI-58), also known as alpha/beta hydrolase domain-containing protein 5 (ABHD5), is an important protein that is associated with lipid droplets (LD) and mitochondria within cells. CGI-58/ABHD5 regulates TG hydrolysis by activating ATGL (116) and it is noteworthy that it is highly expressed in muscle with high oxidative capacity like the heart and SO (117). Inactivating CGI-58 in mice affects specifically oxidative SM and leads to fat accumulation in red SM, which aligns with CGI-58 mutations causing Chanarin-Dorfman syndrome, a disorder characterized by fat deposition in SM and skin ichthyosis (118, 119). Curiously, mice with muscle-specific loss of CGI-58 had improved glucose tolerance and insulin sensitivity on a high-fat diet, suggesting that fat storage in glycolytic muscle is harmful, but in oxidative muscle, it might be protective (119).

HSL, historically seen as the primary enzyme for breaking down TG and DG into FA and MG, is an 84 kDa serine hydrolase made up of a protein and lipid interaction domain, an active catalytic domain, and a regulatory domain with multiple phosphorylation sites (120). Clinical research involving patients with HSL deficiency showed less severe dyslipidemia, hepatic steatosis, and partial lipodystrophy in comparison to ATGL deficiency (121, 122). Additionally, HSL influences insulin sensitivity through its interaction with carbohydrate-responsive element-binding protein (CHREBP), although other regulatory mechanisms likely play a more significant role in controlling insulin sensitivity in humans (123). Studies on HSL-deficient mice show similar characteristics to those lacking ATGL, indicating shared functions in regulating lipolysis and nuclear receptors (122, 124, 125). However, a lack of HSL specifically in SM leads to DG build up, with TG breakdown remaining unaffected, suggesting a significant role of HSL in hydrolyzing muscle DG (126).

MGL is the first identified enzyme capable of hydrolyzing both sn-1 and sn-2 MG, releasing both glycerol and FA (122). While MGL primarily targets MG, it also acts on prostaglandin-glycerol esters and FA-ethyl ethers (127-129). MGL deficiency in mice leads to MG accumulation, impacting lipid metabolism, intestinal lipid absorption, and diet-induced obesity, with pronounced effects on neuroinflammation and cancer malignancy due to altered endocannabinoid signaling (129-134) . However, studies examining the regulation of SM's MGL activity are still scarce.

Recently, it has been described that PNPLA4, also known as gene sequence 2 (GS2), is expressed in several human tissues, including SM (135, 136). Since PNPLA4 is able to degrade TG and retinyl esters, it could also play a role in SM lipolysis and it is worth to be further investigated in this context.

A complex interplay of hormonal and intracellular signaling pathways tightly regulates neutral lipolysis. Hormones such as epinephrine and insulin play key roles in modulating lipolysis in rodents in response to changes in energy sources demand and availability (137). The utilization of FA derived from lipolysis as an energy source during SM contraction is a highly coordinated process involving the transport of FA to mitochondria, where they undergo β-oxidation to generate ATP. This complex network of metabolic reactions provides SM with a constant supply of energy to sustain prolonged physical activity (138). During low- to moderate-intensity exercise, as well as activities that last for long periods of time, most of the energy requirements of SM are met primarily by FA oxidation (FAO), with glucose oxidation playing a smaller role in providing energy (138).

To generate ATP during the final oxidation process, FA produced by the degradation of plasma lipids or intramuscular TG must enter the mitochondria. Initially, FA are activated into fatty acyl-CoA molecules by a set of enzymes known as acyl-CoA synthetases (ACS). ACS are located at several cellular sites including the plasma membrane, mitochondria, and LD (139). The enzyme isoform ACSL1 is particularly crucial for directing FA towards oxidation within SM, evidenced by the fact that muscle-specific ACSL1-deficient mice demonstrated reduced FA usage during physical activity compared to their wild-type (Wt) counterparts (140). Fatty acyl-CoA is transformed into fatty acyl-carnitine by the enzyme carnitine palmitoyl transferase (CPT1). CPT1 is found on the outer mitochondrial membrane and requires carnitine for this conversion process (72). The critical role of CPT1 in FAO in SM has been demonstrated by studies showing that CPT1 knockout mice in muscle exhibit decreased FAO and increased lipid accumulation (141). The pivotal role of CPT1 during exercise is highlighted by experiments showing that inhibition of CPT1 significantly reduced FAO rates by 50% in the EDL and by 90% in the SO muscles of mice (142).

Despite the reported evidence, the importance of intramuscular TG oxidation remains a matter of debate since the experimental data do not provide an unambiguous answer to this problem. Moreover, intramuscular TG oxidation processes are highly dependent on individual characteristics, such as training status, sex, muscle fiber type, and reserves of TG (71).

Taking together, the SM lipid and energy metabolism are complex processes that require the coordinated regulation of various pathways and substrates to meet the changing energy demands of muscular activity. It involves the catabolism of different energy sources, including

ATP, pCr, glycogen, glucose, and TG, each playing a role during distinct exercise intensities and durations. Figure 5 provides an overview of the principal steps in SM energy production. Understanding the dynamics of SM energy and lipid metabolism remains a key area of research to enhance performance, treat metabolic disorders, and improve overall health.

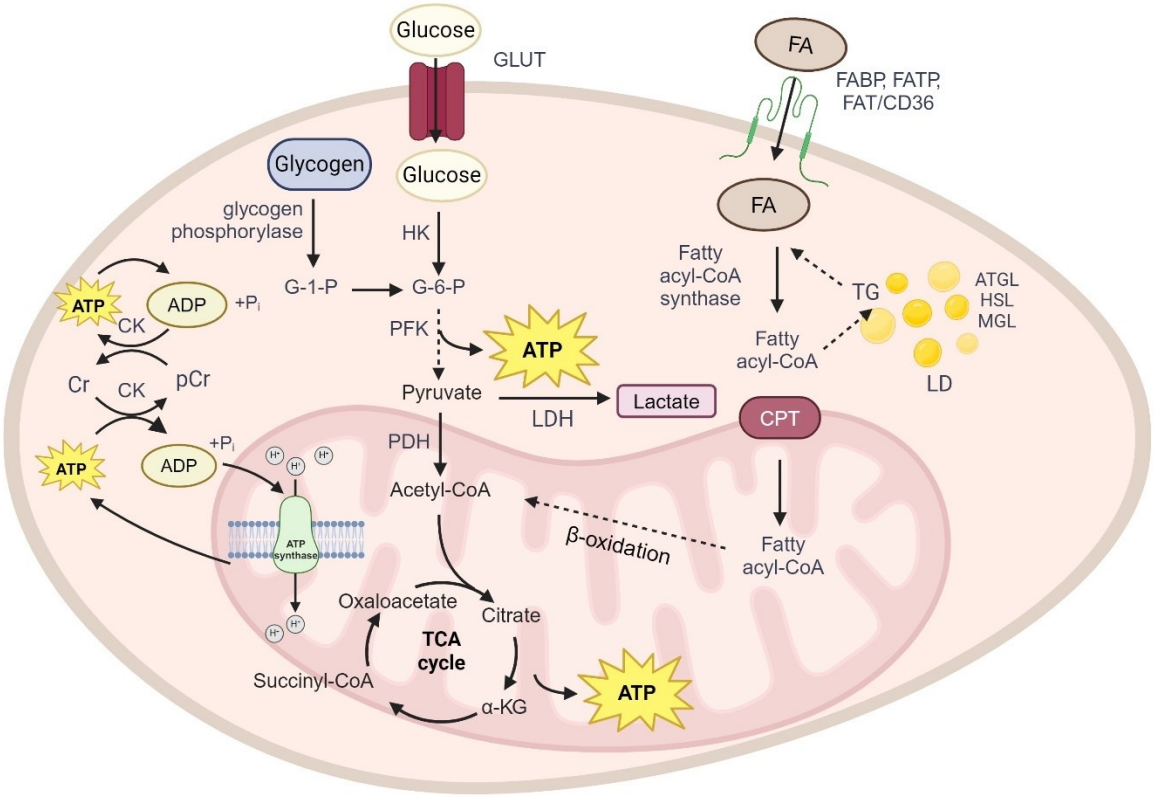

Figure 5: Interplay of carbohydrate and lipid metabolism in skeletal muscle (SM) energy production.
The comprehensive utilization of both extramuscular and intramuscular carbohydrate and lipid fuels to ensure a continuous supply of ATP for SM. Key regulatory enzymes and transport proteins are mentioned, demonstrating the intricate interactions between anaerobic and aerobic metabolic pathways, as well as between carbohydrate and lipid metabolism. Notable components include free fatty acids (FA) crossing the plasma membrane, facilitated by plasma membrane fatty acid–binding protein (FABP), fatty acid transport protein (FATP) and FA translocase (CD36). Carbohydrate metabolism is regulated by crucial enzymes, such as hexokinase (HK) for the production of glucose-6-phospate (G-6-P) and phosphofructokinase (PFK). The conversion of pyruvate to lactate in the absence of oxygen is catalyzed by lactate dehydrogenase (LDH), with creatine and mitochondrial creatine kinase (CK) managing high-energy phosphate storage and transfer across the mitochondrial outer and inner membranes. FA β-oxidation involves proteins including acyl-CoA transferase. The conversion of pyruvate to acetyl-CoA is mediated by pyruvate dehydrogenase (PDH), feeding into the electron transport chain for oxidative phosphorylation. Glucose transporter, GLUT; glucose-1-phosphate, G-1-P; α-ketoglutarate, α-KG; lipid droplet, LD; triglyceride, TG; adipose triglyceride lipase, ATGL; hormone sensitive lipase, HSL; monoglyceride lipase, MGL;

carnitine palmitoyltransferase, CPT; tricarboxylic acid cycle, TCA cycle. Created with Biorender.com.

1.5.3 Other sources of energy

SM cells have the ability to utilize amino acids (AA) as an energy source. During prolonged exercise, when muscle glycogen levels are depleted, SM can increase the oxidation of branched-chain AA (BCAA) like leucine (Leu), isoleucine (Ile), and valine (Val) for energy production (143). BCAA are metabolized by branched-chain aminotransferase 2 (BCAT2) and the branched-chain α-keto acid dehydrogenase complex (BCKDC) within mitochondria (144, 145). Additionally, AA can undergo transamination, a process of amino group transfer to form new AA or intermediates of the TCA cycle (146, 147).

Ketone bodies (KB) are water-soluble molecules generated from FA by the liver through a process known as ketogenesis in response to low carbohydrate availability. These compounds can be easily transported to SM, where they undergo conversion into acetyl-CoA (148, 149).

However, some alternative energy sources, such as AA, acetates and KB, cannot match carbohydrates in terms of energy production rate, nor can they be utilized for anaerobic energy production in the absence of oxygen (71).

1.6 Maintaining SM mass

The maintenance of SM mass involves a complex set of signaling pathways that regulate anabolism (muscle building) and catabolism (muscle breakdown). The delicate balance is crucial for cellular health and function, ensuring the timely production of proteins as required and the removal of damaged or unnecessary proteins. Maintaining this balance supports proper SM growth, repair, and functionality, whereas its disruption can result in various pathologies.

SM hypertrophy is characterized by an increased protein synthesis and/or decreased protein degradation. This process is usually mediated by exercise and activation of anabolic signaling pathways that promote protein synthesis (150-152). Specifically, the insulin-like growth factor 1 (IGF-1)/Akt/mTOR pathway is a crucial intracellular regulator of SM mass and plays a significant role in muscle hypertrophy and atrophy. Growth hormone regulates the synthesis of IGF1, primarily in the liver (153). Studies in transgenic mice have underscored the importance of locally produced IGF1. Muscle-specific overexpression of IGF1 can enhance muscle growth and regeneration even without normal levels of IGF1 in systemic circulation.

This suggests that localized IGF1 signaling regulates SM integrity, promotes recovery from injury, and counteracts muscle wasting conditions (154).

mTOR exerts its effects by phosphorylating key proteins such as p70S6 kinase 1 (p70S6K1) and eukaryotic translation initiation factor 4E-binding protein (4E-BP1). In addition, mTOR protects against excessive protein degradation by inhibiting the autophagy process, particularly through inactivation of unc-51-like kinase 1 (ULK1) (153, 155). mTOR forms two different complexes, mTORC1 and mTORC2. mTORC1 is involved in protein synthesis and cell organelle biogenesis, whereas mTORC2 regulates glucose and lipid metabolism (155). Disrupting mTORC1 components such as Raptor or mTOR itself impairs muscle growth and can lead to muscular dystrophy, whereas Rictor knockouts (mTORC2 complex component) do not show such dramatic effects (156-158). Furthermore, it has been demonstrated that the IGF-1/Akt/mTOR pathway reduces the expression of the muscle atrophy marker *Atrogin-1* and influences fiber size in adult muscle (159). Adrenergic signaling influences muscle mass by interacting with the AKT-mTOR pathway. Similarly, β2-adrenergic stimulation enhances AKT activation via the mTOR pathway, thereby promoting muscle enlargement (160).

Pharmacological inhibition of mTOR with rapamycin or its genetic knockdown reverse muscle growth gains which develop as a consequence of myostatin blocking. Myostatin is a member of the TGFβ superfamily and a key regulator of SM growth (153, 161, 162). Its loss leads to significant muscle gain, emphasizing its suppressive effect on muscle size and development (153, 163). Myostatin and related ligands bind to activin type IIB and type IIA (ActRIIB/IIA) and TGFβ receptors, activating anaplastic lymphoma (ALK) kinases 4, 5, and 7. This leads to Smad2/3 phosphorylation, which then forms a complex with Smad4, affecting gene expression related to protein turnover. Inhibition of Smad2/3 signaling alone can enhance SM growth (161, 162), indicating it controls protein synthesis and degradation. Interestingly, bone morphogenetic protein (BMP), another member of the TGFβ superfamily, activates Smad1/5/8 upon receptor binding, which in turn forms complexes with Smad4 and activates the transcription of genes involved in the regulation of muscle mass (164).

Fibroblast growth factors (FGF) signaling proteins produced by macrophages play major roles in vertebrate embryogenesis, including control of SM growth and differentiation (165). Recent research indicates that FGF19 administration can lead to SM hypertrophy and increased grip strength through extracellular signal-regulated kinase (ERK) activation (166). In contrast, FGF21 has been reported to cause muscle wasting (167).

Opposite to hypertrophy, SM atrophy is characterized by an increase in proteolysis and/or a decrease in protein synthesis. An example of pathologic atrophy is cachexia, an extreme muscle wasting observed in cancer, cardiovascular disease, chronic obstructive pulmonary

disease, renal failure, and severe burns (168). This condition exacerbates the severity of the patient's underlying illness and can also increase the likelihood of death. The FoxO1 signaling pathway assumes a critical role in the SM pathogenesis atrophy through the regulation of E3 ubiquitin ligases and certain autophagy factors (169-171). Despite some studies suggesting that FoxO1 promotes myotube fusion (172, 173), more recent evidence suggests its inhibitory effect on muscle differentiation (169, 173).

Atrogin-1/MAFbx, and MuRF1 are ubiquitin ligases, also known as E3s, and are key regulators of muscle atrophy (174). They are often upregulated in denervation, immobilization, fasting, sepsis, and cancer cachexia (175). MuRF1 primarily targets structural muscle proteins for proteasomal degradation, including those that make up the myofibrils. By tagging these proteins with ubiquitin, MuRF1 marks them for destruction by the proteasome, which contributes to muscle atrophy (176). However, MuRF1 knockout mice show only partial resistance to muscle loss due to denervation and are not protected from muscle atrophy induced by starvation or microgravity, but they are resistant to muscle loss by glucocorticoids (174, 177, 178). Moreover, inhibiting MuRF1 does not mitigate the decline in muscle strength associated with aging, although it assists in preventing muscle mass loss (179). Atrogin-1 not only targets proteins for ubiquitination and subsequent proteasomal degradation but is also associated with the regulation of muscle cell growth and survival pathways. It exhibits a wider range of substrates compared to MuRF1, thereby exerting a broader impact on cellular metabolism and the regulation of muscle mass. (180). Tripartite motif-containing 32 (TRIM32) is another member of the E3 protein family that is known to be involved in muscle diseases such as type 2H muscular dystrophy and sarcotubular myopathy (181). Furthermore, animal studies with TRIM32 dysfunction demonstrate myopathic and neurological defects, highlighting its significant role in muscle health (182, 183). Interestingly, signaling mediated by tumor necrosis factor α receptor adaptor protein 6 (TRAF6), an additional E3 ligase, serves to protect muscle from loss induced by cancer, denervation, and starvation (184).

1.7 Role of lysosomes in SM

Lysosomes are cell organelles surrounded by a single bilayer phospholipid membrane (185) and involved in a variety of biological processes, including cellular clearance, membrane repair, cell homeostasis, energy metabolism, and immunological response (186). Lysosomes contain transport proteins and different enzymes, which are generally known as acid hydrolases. There are roughly 60 different soluble hydrolases exclusively active at an acidic pH in the lysosomal lumen, such as sulfatases, glycosidases, peptidases, phosphatases,

lipases, and nucleases (187, 188). The lysosomal membrane is a specialized and dynamic phospholipid bilayer that encapsulates the organelle's acidic interior. Characterized by a distinct lipid composition, including a high concentration of lysobisphosphatidic acid and cholesterol, it provides stability and enables selective permeability. Integral membrane proteins, such as lysosome-associated membrane proteins (LAMP) and lysosomal integral membrane proteins (LIMP), are embedded within this bilayer, serving critical roles in the lysosome's biogenesis, enzyme transport, and fusion with other vesicles. A prominent feature of a lysosomal membrane is the rich glycocalyx, formed by the carbohydrate portions of glycoproteins, which protect from enzymatic self-digestion. This membrane also houses sophisticated transport mechanisms, like proton pumps, which maintain the organelle's acidic pH, facilitating optimal enzymatic activity (189).

One of the essential functions of lysosomes within cells is to facilitate autophagy, which is a key cellular process responsible for degrading and recycling cellular components (190). This process plays an important role in maintaining cell health by helping to eliminate old and damaged structures, as well as unused nutrient reserves (191). Autophagy is critical for muscle health. Both its hyperactivation and impairment can contribute to muscle degradation and weakness. In certain conditions, such as cancer cachexia, fasting, and sepsis, hyperactivation of autophagy leads to excessive protein degradation and muscle loss (192). Conversely, when autophagy is impaired, as seen in muscle-specific knockout mice for autophagy-related proteins like Atg5, Atg7 (193), VPS15 (194), ULK2 (195), AMPK (196), and mTOR (197), mice suffer from accumulation of damaged cellular components, increased oxidative stress, and mitochondrial dysfunction, all of which can result in SM degeneration and symptoms similar to aging sarcopenia (198). Furthermore, an excessive number of autophagic vacuoles is a characteristic feature of several SM diseases, including autophagic vacuolar myopathies (199). However, reactivation of autophagy, either genetically by re-expressing Atg7 or pharmacologically by using compounds like Urolithin A that promote mitophagy, has been shown to ameliorate muscle loss and improve muscle function in aged mice (200). This therapeutic approach underscores the potential for targeting autophagy pathways to treat muscle degeneration conditions related to aging and other diseases.

Acidic lipolysis, which occurs in lysosomes and is catalyzed by the enzyme lysosomal acid lipase (LAL), has not received as much research attention as neutral lipolysis in SM. Further study of this process may provide valuable insights into its contribution to SM energy metabolism and its importance in both health and disease.

1.8 LAL-mediated lipid degradation

LAL is an essential enzyme located within the lysosomal lumen and plays an essential role in lipid metabolism. It is responsible for the hydrolysis of cholesteryl esters (CE) and TG as well as other lipid derivatives such as retinyl esters (RE), DG, and MG (201). LAL is part of a family of acid lipases as it shares numerous features with lingual and gastric lipase (202, 203). When low-density lipoproteins (LDL) particles bind their receptor on the plasma membrane, they undergo receptor-mediated endocytosis and are internalized in clathrin-coated vesicles, (Fig. 6). The process of endocytosis in SM fibers begins near the I-bands, a region of the sarcomere within the muscle fibers (204). Following internalization, the endocytosed vesicles are directed to endosomes. Some endosomes are then recycled back to the cell surface, whereas others are transported to late endosomes and lysosomes for degradation (205). After hydrolysis of the more complex lipids, FA and cholesterol may undergo transesterification in the endoplasmic reticulum (ER) and accumulate in form of intracellular LD. Activation of autophagy also leads to the transport of LD to the lysosomes for LAL-mediated hydrolysis and generation of FA. This pathway is an alternative to the classic mobilization of LD-stored FA by neutral hydrolases (206) .

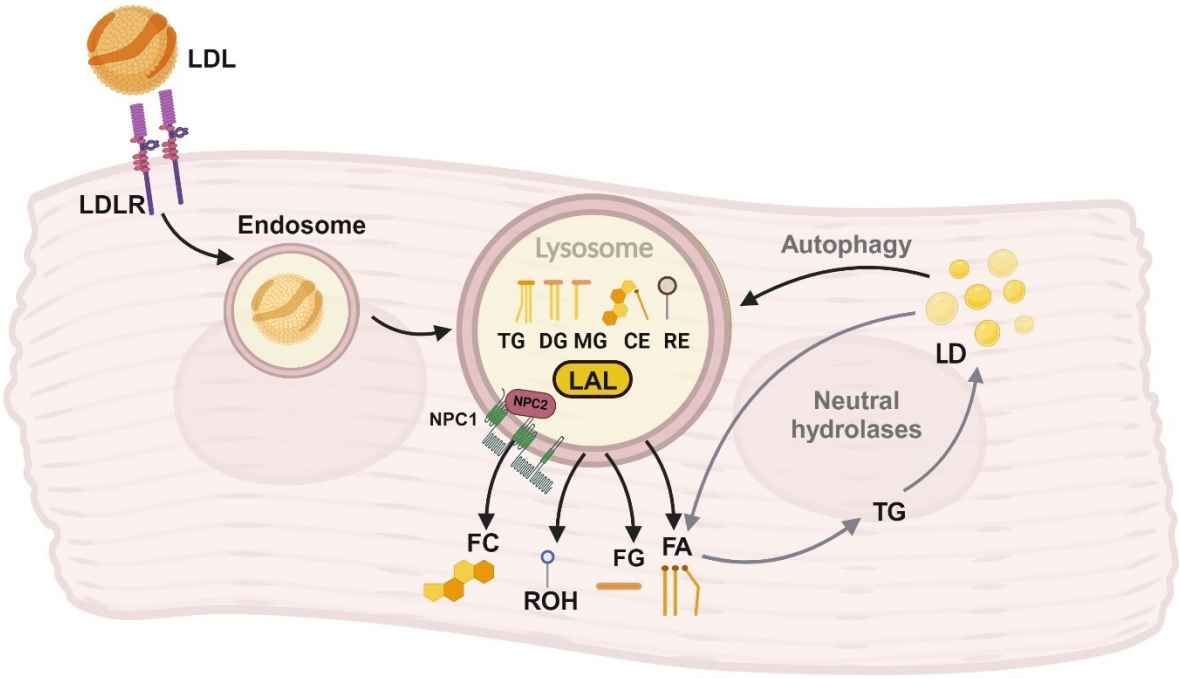

Figure 6: Schematic representation of lysosomal acid lipase (LAL)-mediated lipid hydrolysis.
Low-density lipoprotein (LDL) particles, which are internalized by receptor-mediated endocytosis, and lipid droplets (LD) delivered to the lysosome via autophagy provide LAL with substrates such as triglycerides (TG), diglycerides (DG), monoglycerides (MG), retinyl esters (RE), and cholesteryl esters (CE). These are then broken down into free cholesterol (FC), fatty

acids (FA), free glycerol (FG), and retinol (ROH). FC is released from the lysosomes by the action of NPC1 and NPC2. Created with Biorender.com

LIPA, the LAL encoding gene, has a size of approximately 36.5 kb and is located on the chromosome locus 10q23.2-23.3 in humans (207). The amino acid sequence of the mouse LAL demonstrates a high degree of similarity to its human counterpart, with 95% overall homology and 75% identity across the sequences. This includes the conservation of crucial motifs, such as the active serine site motif G-X-S-X-G, which is essential for the enzyme's catalytic function. Additionally, the enzyme retains five putative consensus sequences for N-glycosylation, which are involved in the post-translational modification of the protein, further reflecting the enzyme's conservation across species (208). It was confirmed that at least two of the six N-glycosylation sites (N134 and N246) are essential for LAL activity. LAL localizes to pre-lysosomal compartments following co-translational glycosylation in the ER and the acquisition of mannose-6-phosphate residues in the Golgi apparatus (209).

1.9 Regulation and activity of LAL

Particularly during starvation, lysosomal function is highly regulated to efficiently deliver macromolecules and organelles for degradation. Central to this regulatory network is the transcription factor EB (TFEB), which relocates to the nucleus under nutrient deprivation to promote lysosomal biogenesis and function. TFEB is able to indirectly increase the expression of hydrolytic enzymes including LAL through the PPAR-PGC1α signaling cascade (210-213). Simultaneously, starvation activates SIRT1, which deacetylates and assists in the nuclear translocation of FoxO1, leading to increased expression of LAL and ATGL for enhanced FA mobilization (214, 215). In LAL deficiency (LAL-D), a condition characterized by impaired lysosomal lipid breakdown, the release of FA into the cytosol is obstructed, leading to significant metabolic disruptions. The inactivation of PPARγ and the reduced interaction of FA with PPARα and its co-activator PGC1α result in a decline in peroxisomal FAO. This causes the impaired release of FA into the cytosol, leading to significant metabolic consequences. Specifically, LAL-D causes the accumulation of lipids in lysosomes that contributes to abnormal energy production and altered lipid signaling, underlining the critical role of LAL in cellular lipid homeostasis (216-218).
However, under pathological conditions such as in the presence of oxidized LDL, LAL activity can be negatively affected, resulting in a rise in lysosomal pH and accumulation of CE, ultimately disrupting the delicate balance of cholesterol homeostasis and lysosomal function (219-221). LAL demonstrates optimal activity within pH ranges of 4-5, and its activity can be

assessed using various methods, including the release of FA from radioactively labeled CE and TG or synthetic substrates such as 4-methylumbelliferone esters (4-MU) (202, 203, 222-224).

1.10 LAL deficiency in humans

Multiple soluble hydrolases that are active exclusively at acidic pH values can be found in the lumen of lysosomes (225). Mutations in genes encoding enzymes and proteins critical to lysosomal function are responsible for a group of over 70 autosomal recessive human genetic diseases known as lysosomal storage diseases (LSD) (226). Historically. LAL-D was referred to as two separate disorders, the first being a rapidly progressive form with an early onset (an infantile form of LAL-D, called Wolman's disease (WD)) (227, 228) and the second one being a form of LAL-D in children and adults, formerly known as cholesterol ester storage disease (CESD) (229). Lack (up to 10% residual LAL activity in CESD patients) or absence (≤1% of LAL activity in WD patients) leads to disruption of intralysosomal hydrolysis of CE and TG and their accumulation in target organs (218).

WD is the most severe form of LAL-D and typically presents in infancy with a range of serious symptoms. The hallmark of the disease is retarded growth and significant liver pathology, characterized by rapid and progressive liver enlargement (228). This is paired with elevated transaminases and high levels of bilirubin pointing to liver or bile duct dysfunction, hypoalbuminemia reflecting poor liver synthesis or malnutrition, and coagulopathy revealing impaired blood clotting abilities (229). Malabsorption symptoms in WD patients arise from the inability to properly digest and utilize lipids and other nutrients (218, 229). Adrenal calcification occurs in approximately half of WD patients (227-229). Prior to the development of enzyme replacement therapy (ERT), a treatment that compensates for the deficient enzyme, WD was invariably fatal within the first 4 months of life (230), underscoring the devastating impact of the disease and the critical role of LAL in lipid metabolism and overall health.

The LAL-D form in children and adults, or CESD, is the second form of LAL-D. CESD is characterized by accumulation of lipids in lysosomes which leads to hepatosplenomegaly and the development of liver fibrosis and/or cirrhosis and increased activity of transaminases in the blood. Additional dyslipidemia described as an increase in cholesterol (sometimes TG) levels due to LDL and decreased levels of HDL (231) may lead to early atherosclerosis (232, 233). Secondary complications are varied and can include portal hypertension, ascites, cachexia, esophageal varices, gastrointestinal bleeding, ischemic heart disease, aneurysm, stroke, anemia, and thrombocytopenia (232).

LAL-D is recognized as a rare disease with its prevalence varying significantly from one in 40,000 to one in 300,000 individuals, influenced by factors such as ethnic origin and geographic distribution (231). Diagnosis of LAL-D is challenging because the symptoms overlap with various cardiovascular, hepatic, and metabolic diseases (234). When LAL-D is suspected, the preferred screening method is dried blood spot testing, which is non-invasive and uses 4-MU to measure LAL activity (235). The test includes the use of the LAL inhibitor Lalistat-2 to prevent interference from other lipases in the blood. Although Lalistat-2 has been noted to have nonspecific effects at a neutral pH (236), it is a highly effective LAL inhibitor at the acidic pH of 4.5 (237, 238). This assay compares overall lipase activity with the activity in the presence of Lalistat-2, hence accurately estimating LAL function, and aids in identifying LAL-D patients, carriers, and non-affected individuals. Additionally, the evaluation of biomarkers in the blood, such as chitotriosidase, the C-C motif chemokine 18, and glycoprotein non-metastatic melanoma protein B, offers an ancillary and practical method for the detection of LAL-D (239).

Further research in populations with a high prevalence of undiagnosed LAL-D, such as those with familial hypercholesterolemia (FH), revealed that elevated transaminase levels serve as a significant clinical indicator in differentiating FH from LAL-D, especially in children (240). Patients with LAL-D often experience dyslipidemia, leading to the widespread use of lipid-lowering agents. Statins, particularly 3-hydroxy-3-methyl-glutaryl-coenzyme A (HMG-CoA) reductase inhibitors, are commonly prescribed but show varied efficacy in those patients (241-245). Additionally, ERT using Sebelipase alfa has demonstrated effectiveness in improving histology and clinical parameters in different tissues, particularly in late-onset CESD patients (246, 247). Clinical investigations and trials reveal positive outcomes in terms of liver function and lipid profiles (248-251). Long-term data from these studies suggest sustained improvements, raising the possibility of halting or even reversing liver damage with Sebelipase alfa therapy (250). Although Sebelipase alfa significantly improves the lives of those with LAL-D, several challenges constrain its usage. These include the requirement for regular intravenous administrations, the expectation of lifelong therapy (252), and the substantial financial burden associated with its cost (218). Moreover, the therapeutic use of Sebelipase alfa for early-onset LAL-D patients is often compromised by the development of anti-drug antibodies, especially neutralizing types that necessitate dosage modulation (248). Other hurdles of enzyme replacement therapy encompass potential egg allergies, the necessity for recurrent intravenous treatments (252).

1.11 LAL-D animal models

The first animal model of LAL-D, identified in 1990, arose due to a spontaneous mutation within a colony of Donryu rats (253). Further progress was made in the study of LAL-D with the development of a LAL-knockout (Lal-/-) mouse model through targeted disruption of the *Lipa* gene (254). The *Lipa* gene in the mouse genome is situated on chromosome 19 (255). Mouse LAL is highly expressed in various tissues such as kidney, adrenal glands, pancreas, liver, and small intestine (256), whereas expression of *Lipa* in SM and heart is low (257). Global Lal-/- mice exhibit viability with a median lifespan of around one year (256). These mice display abnormal lipid metabolism, characterized by the accumulation of TG and CE in the liver, resulting in growth retardation, absence of white adipose tissue (WAT), and gradual loss of brown adipose tissue (BAT) (256). Targeted deletion of the *Lipa* gene leads to significant changes in the hepatic phenotype including microvesicular steatosis, Kupffer cell infiltration forming nests of "fatty lysosomes", and extensive cholesterol crystal formation, associated with cellular integrity disruption and inflammatory responses (258). Additionally, Lal-/- mice manifest unique features like enlarged mesenteric lymph nodes with substantial lipid accumulation, indicating the systemic impact of LAL deficiency on various tissues and their lipid homeostasis (256).

Specifically, the intestinal phenotype of Lal-/- mice included the infiltration of lipid-associated macrophages into the lamina propria, accompanied by a substantial accumulation of neutral lipids in the small intestine (259, 260). Additionally, Lal-/- mice exhibited reduced absorption of dietary lipids, accelerated basolateral lipid uptake, diminished chylomicron secretion, and heightened fecal lipid loss. In the duodenum of older Lal-/- mice, inflammatory markers and genes associated with lipid metabolism were upregulated, a phenomenon not observed in younger animals. Notably, enterocyte-specific LAL knockout mice, despite a significant reduction in LAL activity, displayed comparable intestinal lipid concentrations, expression of lipid transporters and inflammatory genes, as well as lipoprotein secretion as control mice (259). Lal-/- mice have triggered pulmonary inflammation, leading to significant changes in the alveolar structure, the development of pulmonary emphysema, and notable hypertrophy and hyperplasia of Clara cells (261).

LAL promotes cholesterol homeostasis in BAT, potentially directing lysosomal cholesterol towards steroidogenesis. Moreover, LAL-D in mice impairs BAT thermogenesis and FA shuttling from circulating lipoproteins, compromising metabolic and thermoregulatory functions (262). Despite multiple dysregulations, Lal-/- mice exhibit improved insulin and glucose tolerance tests, indicating enhanced insulin sensitivity. Furthermore, these mice demonstrate

an increased glucose uptake into SM as compared to their Wt counterparts (263). This paradoxical improvement in glucose metabolism in LAL-D suggests complex metabolic adaptations.

1.12 Hypothesis and aims

The concept of a lysosomal acidic environment specifically contributing to the lipolytic process in SM is less documented and understood. Previous reports suggested decreased SM activity (264, 265) and mass (227, 266-268) in LAL-D patients, but the role of LAL in the metabolic balance of SM has never been thoroughly investigated. Given the high energy demand of SM, we hypothesized that changes in energy homeostasis caused by the loss of LAL might affect muscle biology. To test our hypothesis, we compared SM from Lal-/- mice with those of their Wt littermates.

My first aim was to characterize the structural, metabolic, and functional changes in the SM of Lal-/- mice. Accordingly, my second aim was to find out whether the observed changes in the SM of Lal-/- mice are related to the direct loss of LAL in SM or to systemic effects of the whole-body knockout using cellular models and the LAL inhibitor Lalistat-2.

2. Materials and methods

2.1 Materials

Plastic and cell culture ware were purchased from Greiner Bio-One (Kremsmünster, Austria).

2.2 Chemicals

[1-^{14}C] - oleic acid, Amersham Bioscience, Piscataway, NJ
[1-^{14}C] - palmitic acid, Hartmann Analytic, Braunschweig, Germany
2-Desoxy-D-Glucose, Lactan, Graz, Austria
^{3}H-2-Deoxy-D-Glucose, Hartmann Analytic, Braunschweig, Germany
[9,10-^{3}H(N)] - triolein, Perkin Elmer, Waltheim, MA
Adenosine-5′-diphosphate monopotassium salt dihydrate (ADP), Sigma-Aldrich, St. Louis, MO
Adenosine-5′-triphosphate disodium salt hydrate (ATP), Sigma-Aldrich, St. Louis, MO
Ammonium chloride, Carl Roth, Karlsruhe, Germany
Antimycin, Sigma-Aldrich, St. Louis, MO
APS, Sigma-Aldrich, St. Louis, MO
Bisacrylamide, Applichem, St. Louis, MO
Bromophenol blue, Solis BioDyne OÜ, Tartu, Estonia
BSA FA-free, Capricon scientific, Ebsdorfergrund, Germany
Calcium chloride ($CaCl_2$), Carl Roth, Karlsruhe, Germany
Carbonylcyanide-3-chlorphenylhydrazone (CCCP), Sigma-Aldrich, St. Louis, MO
Chloroform, Carl Roth, Karlsruhe, Germany
Citric acid monohydrate, Carl Roth, Karlsruhe, Germany
Cytochrome c, Sigma-Aldrich, St. Louis, MO
D-(-)-Mannit, Carl Roth, Karlsruhe, Germany
Di-Sodium hydrogen phosphate heptahydrate ($Na_2HPO_4*7H_2O$), Merck, Darmstadt, Germany
DMSO, Honeywell FlukaTM, Charlotte, NC
DTT, Carl Roth, Karlsruhe, Germany
EDTA, ThermoFisher Scientific, Waltham, MA
EGTA, GERBU Biotechnik GmbH, Germany
Eosin G, Carl Roth, Karlsruhe, Germany
Ethanol 99.9%, AustrAlco, Spillern, Austria
Ethidium bromide, Merck, Darmstadt, Germany
Formaldehyde, Merck, Darmstadt, Germany

Formalin, Carl Roth, Karlsruhe, Germany
Glutamine, ThermoFisher Scientific, Waltham, MA
Glycerol, Sigma-Aldrich, St. Louis, MO
Glycine, Carl Roth, Karlsruhe, Germany
HEPES, Sigma-Aldrich, St. Louis, MO
Hexane, Carl Roth, Karlsruhe, Germany
Hydrogen chloride (HCl), Carl Roth, Karlsruhe, Germany
Isopropanol, Carl Roth, Karlsruhe, Germany
L-glutamic acid monosodium salt hydrate (glutamate), Sigma-Aldrich, St. Louis, MO
L-(-)-malic acid (malate), Sigma-Aldrich, St. Louis, MO
Lactobionic acid, Lactan, Graz, Austria
Lalistat-2, Sigma-Aldrich, St. Louis, MO
Magnesium dichloride hexahydrate ($MgCl_2 \times 6H_2O$), Carl Roth, Karlsruhe, Germany
Methanol, Carl Roth, Karlsruhe, Germany
Milk powder, Carl Roth, Karlsruhe, Germany
Nonidet P-40 (NP-40), Honeywell Fluka™, Charlotte, NC
Oil Red O (ORO), Sigma-Aldrich, St. Louis, MO
Palmitoyl-L-carnitine, Sigma-Aldrich, St. Louis, MO
Phosphatidylcholine (PC), Sigma-Aldrich, St. Louis, MO
Phosphatidylinositol (PI), Sigma-Aldrich, St. Louis, MO
Potassium carbonate (K_2CO_3), Carl Roth, Karlsruhe, Germany
Potassium chloride (KCl), Carl Roth, Karlsruhe, Germany
potassium dihydrogenphosphate (KH_2PO_4), Carl Roth, Karlsruhe, Germany
Potassium hydroxide (KOH), Carl Roth, Karlsruhe, Germany
Potassium-4-morpholineethanesulfonic acid (MES), Merck, Darmstadt, Germany
Protease inhibitor cocktail (PIC), Sigma-Aldrich, St. Louis, MO
Proteinase K, Lactan, Graz, Austria
Rotenone, Sigma-Aldrich, St. Louis, MO
Saponin, Sigma-Aldrich, St. Louis, MO
SDS, Carl Roth, Karlsruhe, Germany
Sodium deoxycholate, Sigma-Aldrich, St. Louis, MO
Sodium bicarbonate ($NaHCO_3$), Carl Roth, Karlsruhe, Germany
Sodium chloride (NaCl), Merck, Darmstadt, Germany
Sodium succinate dibasic hexahydrate (Succinate), Sigma-Aldrich, St. Louis, MO
Sodium pyruvate, ThermoFisher Scientific, Waltham, MA

Sucrose, Carl Roth, Karlsruhe, Germany

Temed, Carl Roth, Karlsruhe, Germany

TES, Sigma-Aldrich, St. Louis, MO

Tris-HCl Carl Roth, Karlsruhe, Germany

Trisodium citrate ($Na_3C_6H_5O_7$), Merck, Darmstadt, Germany

Sodium hydroxide (NaOH), Carl Roth, Karlsruhe, Germany

TRISure™, Meridian Bioscience Cincinnati, OH

Triton X-100, Carl Roth, Karlsruhe, Germany

Trypsin, Millipore, Billerica, MA

Tween 20, Carl Roth, Karlsruhe, Germany

Xylene, Sigma-Aldrich, St. Louis, MO

β-Mercaptoethanol, Sigma-Aldrich, St. Louis, MO

2.3 Commonly used buffers and solutions

Table 2. Composition and storage conditions of commonly used buffers and solutions.

Used buffers and solutions Solution	Composition	pH	Storage
Ammonium-chloride-potassium (ASK) lysing buffer	10 mM $KHCO_3$ 155 mM NH_4Cl 0.1 mM EDTA	pH 7.2-7.4	4°C
Acrylamide mix 30% (100 mL)	30 g acrylamide 0.8 g bis- acrylamide		4°C
BiOPS	10 mM Ca^{2+}/EGTA 20 mM imidazole 50 mM MES 0.5 mM DTT 6.56 mM $MgCl_2$ 5.77 mM ATP 15 mM pCr	pH 7.1	-20°C
Blocking buffer for western blot	5% skim milk in TBST		4°C
Blotting buffer 1x	25 mM Tris 192 mM glycine 20% MeOH	pH 8.3	Freshly prepared
Citrate lysis buffer	54% 0.1 M citric acid monohydrate	pH 4.2	Freshly prepared

	46% 0.1 M trisodium citrate dehydrate		
DNA extraction buffer	100 mM NaCl 25 mM EDTA 10 mM Tris-Cl 0.5% SDS 1 mg/mL proteinase K	pH 8	4°C
Hank's Balanced Salt Solution (HBSS)	0.137 M NaCl 5.4 mM KCl 0.25 mM Na_2HPO_4 0.1 g glucose 0.44 mM KH_2PO_4 1.3 mM $CaCl_2$ 1.0 mM $MgSO_4$ 4.2 mM $NaHCO_3$	pH 7.4	4°C
Lysis buffer (for TGH activity assay)	0.25 M sucrose 0,1 M KH_2PO_4 1 mM EDTA 1 mM DTT	pH 7	4°C
Lysis buffer (for lipid extraction using Folch method)	100 mM KH_2PO_4 250 mM sucrose 1 mM EDTA	pH 7	4°C
Lysis buffer (for proteasomal assay)	40 mM Tris 50 mM NaCl 2 mM β-mercaptoethanol 2 mM ATP 5 mM $MgCl_2$ 10 % glycerol	pH 7.2	Freshly prepared
Mitochondrial Respiration Medium (MiRO6)	110 mM D-sucrose 60 mM lactobionic acid 0.5 mM EGTA 3 mM $MgCl_2$ 20 mM taurine 10 mM KH_2PO_4 20 mM HEPES 1 g/L BSA ~280 U/mL catalase	pH 7.1	-20°C
NMR buffer	0.08 M Na_2HPO_4 4.6 mM TSP 0.04% (w/v) NaN_3 in D_2O	pH 7.4	Freshly prepared

ORO (stock solution) (100 mL)	0.5 g ORO powder in isopropanol		RT
Phosphate-buffered saline (PBS)	137 mM NaCl 2.7 mM KCl 10 mM Na_2HPO_4 1.8 mM KH_2PO_4		RT
Potassium-phosphate buffer 0.1 M	61.5 mM K_2HPO_4 38.5 mM KH_2PO_4	pH 7	
Respiration buffer	125 mM sucrose 20 mM TES 2 mM $MgCl_2$ 1 mM EDTA 4 mM KH_2PO_4 3 mM malate 0.1% FA-free BSA	pH 7.2	-20°C
RIPA buffer	150 mM sodium chloride 1% NP-40 0.5% sodium deoxycholate 0.1% SDS 50 mM Tris	pH 8	4°C
SDS sample buffer 2x (loading buffer)	4% SDS 10% 2-mercaptoethanol 20% glycerol 0.004% bromophenol blue 0.125 M Tris-HCl	pH6.8	RT
Separating gel 12% (1 gel)	2.847 mL ddH2O 2.17 mL Tris buffer 3.583 mL 30% acrylamide mix 4.4 µL TEMEND 76 µL 10% APS	pH 8.8	Freshly prepared
Stacking gel (1 gel)	885 µL ddH2O 385 µL Tris buffer 350 µL 30% acrylamide mix 10 µL 10% SDS 3.8 µL TEMEND 38 µL 10% APS	pH 6.8	Freshly prepared
TBST 10x (Washing buffer)	1.5 M NaCL 0.5% Tween 20 0.1 M Tris HCL		RT

Tris-glycine buffer 10x	200 mM Tris 1.6 M glycine 0.83% SDS	pH 8.3	RT
Tris buffer for separating gel	0.5 M Tris HCl	pH 8.8	4°C
Tris buffer for stacking gel	0.5 M Tris HCl	pH 6.8	4°C

2.4 Commonly used kits

Table 3. Commonly used kits and their storage conditions.

Kit	Company	Storage
Clarity Western ECL Substrate	Bio Rad Laboratories, Hercules, CA	4°C
DC Protein Assay	Bio Rad Laboratories, Hercules, CA	RT
Fluorometric assay kit II	UBPBio, Aurora, CO	-80°C
Free Cholesterol FS	DiaSys, Holzheim, Germany	4°C
High Capacity cDNA Reverse Transcription Kit	Applied Biosystems, Carlsbad, CA	-20°C
MCP1 ELISA	R&D Systems, Minneapolis, MN	4°C
Total Cholesterol FS	DiaSys, Holzheim, Germany	4°C
Triglyceride FS	DiaSys, Holzheim, Germany	4°C

2.5 Devices and equipment

Table 4. Commonly used equipment.

Equipment	Company
CaloTreadmill	TSE Systems, Berlin, Germany
Centrifuge (5471R, 5810, 5810R)	Eppendorff, Hamburg, Germany
CFX96 Real Time System™	Bio Rad Laboratories, Hercules, CA
CLARIOstar	BMG LABTECH, Ortenberg, Germany
Eppendorf Thermomixer Comfort	Eppendorff, Hamburg, Germany
Epredia™ CryoStar™ NX50 Kryostat	Thermo Fisher Scientific, Waltham, MA

Microplate photometer HiPo MPP-96	Biosan, Riga, Latvia
Model 120 Sonic Dismembrator	Thermo Fisher Scientific, Waltham, MA
Olympus BX63 microscope Olympus	Olympus, Shinjuku, Japan
Oxygraph-2k high-resolution respirometer	Oroboros Instruments, Innsbruck, Austria
pH meter pH 3110	WTW electronics, Graz, Austria
Power supply (Power Pac 300)	Bio-Rad, Hercules, CA
Precellys	Bertin Instruments, Bretonneux, France
Liquid scintillation analyzer Tri-Carb 4910 TR	Perkin Elmer, Waltham, MA
Seahorse XFe analyzer	Agilent, Santa Clara, CA
Spectrophotometer NanoDrop ND1000	Peqlab, Darmstadt, Germany
Thermal cycler C1000Touch	Bio-Rad, Hercules, CA
Water bath SW21	JULABO, Seelbach, Germany

2.6 Animals

Lal-/- mice were accessible for experimentation in-house. The original animals of this line were generously supplied by Hong Du and Cong Yan from the Indiana University School of Medicine, IN. Subsequently, these mice underwent a process of backcrossing to achieve a genetic background consistent with C57BL/6J. In this thesis, I investigated the function of LAL across various SM: the *quadriceps* (QU), GA, TA, and SO. All mice were matched by age and sex for the experiments. SM of young (15-21 weeks) and mature (33-44 weeks) female mice both fed and fasted, and young (12-16 weeks) fed, juvenile (8-12 weeks) fasted, and old (40-50 weeks) fasted male Lal-/- mice were analyzed in comparison with their Wt counterparts.
The mice were housed in an environment that was kept clean and had a stable temperature (around 22°C), a humidity rate around 45%-65%, and a consistent light-dark cycle that lasted 12 h each. For those in the fed state, mice had continuous access to a chow diet that was low in fat (4%) and moderate in protein (9%) (Altromin, Lage, Germany), while fasting conditions varied between 4-6 or 12 h without food. Additionally, there was an experimental group subjected to a diet challenge, where mice were fed a diet high in fat (30%) and cholesterol (1%) (HF/HCD, Ssniff®, Soest, Germany).
All animal experiments conducted adhered strictly to the guidelines outlined in the European Directive 2010/63/EU, ensuring compliance with national regulations. Approval for these experiments was obtained from the Austrian Federal Ministry of Education, Science and

Research, Vienna, Austria. The specific approval numbers granted for the experiments were 2020-0.129.904, 2022-0.121.513, and BMWFW-66.010/0081-WF/V/3b/2017 (269).

2.7 Cells

2.7.1 Cell line

C2C12 (immortalized mouse myoblast cell line) cells were cultured in high-glucose Dulbecco's Modified Eagle's Medium (DMEM) (25 mM glucose, 4 mM glutamine, 1 mM sodium pyruvate) (Gibco, Thermo Fisher Scientific, Waltham, MA) supplemented with 10% fetal bovine serum (FBS) (Gibco, Thermo Fisher Scientific) and 1% penicillin/streptomycin (Gibco, Thermo Fisher Scientific) at 37°C and 5% CO_2. For differentiation, we used DMEM supplemented with 2% horse serum (Gibco, Thermo Fisher Scientific) and 1% penicillin/streptomycin. To inhibit LAL activity, cells were cultured in proliferation or differentiation medium for 4 or 6 days, respectively, with 0,1, 1 or 10 µM Lalistat-2 (Sigma-Aldrich, Saint Louis, MO) dissolved in ethanol (EtOH, final concentration: 0.1%).

2.7.2 Primary myoblasts

Juvenile mice were euthanized via cervical dislocation, followed by a wash with 70% ethanol. Hindlimb muscles were harvested and placed in a Petri dish with HBSS (Gibco, Thermo Fisher Scientific, Waltham, MA) containing 0.2% BSA and 0.5% penicillin/streptomycin. A digestion buffer consisting of 3 mg/mL dispase (Roshe, Basel, Switzerland) in HBSS (Gibco, Thermo Fisher Scientific) filtered through a 0.22 µm filter, 2 mg/mL collagenase A (Roshe), 8 mM $CaCl_2$ (Sigma-Aldrich, St. Louis, MO), 10 µg/mL DNAse I (Roshe), and 5 mM $MgCl_2$ (Sigma-Aldrich) was prepared directly before the experiment. SM were minced and transferred to Falcon tubes containing 40 mL (for Wt mice) or 20 mL (for Lal-/- mice) of digestion buffer. Resuspension with blazed glass Pasteur pipettes and manual stirring were performed every 15 or 20 min during a 45-60-min digestion period at 37°C. The digested cells were recovered, filtered through 40-µm cell strainers, and centrifuged. The obtained cell suspension was treated with ammonium-chloride-potassium (ASK) lysing buffer. Subsequent centrifugation steps and supernatant aspirations were conducted to obtain the desired cell populations for further analysis. Freshly isolated cells were plated at high density (4000 cells/cm^2) on gelatine-coated dish in growth medium comprised of high-glucose DMEM supplemented with 20% FBS, 10% horse serum, 1% Hepes (Gibco, Thermo Fisher Scientific), 1% sodium pyruvate (Gibco,

Thermo Fisher Scientific), and 1% penicillin/streptomycin, with the addition of 5 ng/mL basic FGF (Peprotech, Thermo Fisher Scientific) for 4-5 days. The medium was then switched to differentiation medium consisting of high-glucose DMEM supplemented with 10% horse serum and 1% penicillin/streptomycin for 3 days.

2.8 Methods

2.8.1 RNA isolation and real-time PCR

C2C12 cells were lysed directly in a 6-well plate by adding 1 mL of TRIsure reagent per 10 cm^2 growth area. Then the cells were retrieved using cell scrapers and pipetted several times to ensure sufficient cell disruption. SM (approximately 60 mg) were homogenized in 1 mL of TRIsure reagent using Precellys.

To initiate phase separation, 200 µL of chloroform per 1 mL of TRIsure was used and the samples were incubated for 5 min at RT. Subsequently, the samples were centrifuged at 6,289 *x g* for 15 min at 4 °C. The aqueous phase following phase separation was carefully transferred to a new tube without disturbing the interphase. RNA was precipitated by adding cold isopropyl alcohol (500 µL per 1 mL of TRIsure) and incubating the samples for 10 min at RT. Centrifugation at 6,289 *x g* for 10 min at 4 °C resulted in RNA precipitation. After discarding the supernatant, the RNA pellet was washed once with 75% ethanol and centrifuged to collect the rest of EtOH. The air-dried pellet was dissolved in 20-100 µL DEPC-treated water and the RNA concentration was estimated in 2 µL using a NanoDrop spectrophotometer at 260 nm (269). RNA from primary myoblasts was extracted with Monarch® total RNA miniprep kit (New England Biolabs, Ipswich, MA) followed the manufacturer's protocol.

Reverse transcription

Five hundred ng or one µg of RNA were reverse transcribed in 20 µL using the high capacity cDNA reverse transcription kit. The composition of the master mix for the reverse transcription kit is detailed in Table 5.

Table 5. Master mix for reverse transcription of RNA to cDNA.

Component	Volume (µL)/reaction
10X RT-buffer	2
dTNP Mix	0.8
10X Random primers	2
Reverse transcriptase	1
RNase inhibitor	0.7
Nuclease-free water	3.5

The reverse transcription conditions in the thermal cycler C1000Touch are listed in Table 6.

Table 6. The thermocycler program for reverse transcription.

Step	Step 1	Step 2	Step	Step 4
Temperature	25°C	37°C	85°C	4°C
Time	10 min	120 min	5 s	∞

Real-time PCR

The cDNA samples were diluted either 1:25 or 1:16.5 in nuclease-free ddH_2O when 1 µg or 500 ng of RNA were used for reverse transcription, respectively. Subsequently, 3 µL of the diluted cDNA, along with 1 µL each of forward and reverse primers (prepared from a stock solution of 100 µM and diluted 1:10 with nuclease-free ddH_2O), and 5 µL of GoTaq® qPCR Master Mix (Promega, Madison, WI) were pipetted into PCR plates (Bio-Rad Laboratories, Hercules, CA). After short centrifugation, the plate was loaded onto a CFX96 Real-Time PCR detection system for real-time PCR analysis, following the program conditions outlined in Table 7. The primers used are listed in Table 8 in alphabetical order. The expression profiles were determined utilizing the $2^{-\Delta\Delta CT}$ method, following normalization to the reference genes *Cyclophilin A* or *Gapdh*, established as housekeeping genes, ensuring reliable quantification of target gene expression levels (269).

Table 7. Real-time PCR program.

	Temperature	Time	Cycles
Denaturation and amplification	95°C 60°C	10 s 30 s	40
Melting curve	95°C 60°C 95°C	10 s 20 s continuous	1 1
Cool down	4°C	∞	

Table 8. Primer sequences used for real-time PCR.

Gene	Forward sequence (5'-3')	Reverse sequence (5'-3')
16S	CCGCAAGGGAAAGATGAAAGAC	TCGTTTGGTTTCGGGGTTTC
Acox1	TCCAGACTTCCAACATGAGGA	CTGGGCGTAGGTGCCAATTA
Acsl1	ACCAGCCCTATGAGTGGATTT	CAAGGCTTGAACCCCTTCTG
Atrogin1	CTTTCAACAGACTGGACTTCTCGA	CAGCTCCAACAGCCTTACTACGT
Cat	AGCGACCAGATGAAGCAGTG	TCCGCTCTCTGTCAAAGTGTG
Ccl2	TTAAAAACCTGGATCGGAACCAA	GCATTAGCTTCAGATTTACGGGT
Cd36	GCAGGTCTATCTACGCTGTG	GGTTGTCTGGATTCTGGAGG
Cpt1b	TTCAACACTACACGCATCCC	GCCCTCATAGAGCCAGACC
Cyclophilin A	CCATCCAGCCATTCAGTCTT	TTCCAGGATTCATGTGCCAG
Fabp3	ACCTGGAAGCTAGTGGACAG	TGATGGTAGTAGGCTTGGTCAT
Fabp4	AAGGTGAAGAGCATCATAACCCT	TCACGCCTTTCATAACACATTCC
Fatp1	CGCTTTCTGCGTATCGTCTG	GATGCACGGGATCGTGTCT
Foxo1	ATGCTCAATCCAGAGGGAGG	ACTCGCAGGCCACTTAGAAAA
Gapdh	ACCACAGTCCATGCCATCAC	CACCACCCTGTTGCTGTAGCC
Gpx1	AGTCCACCGTGTATGCCTTCT	GAGACGCGACATTCTCAATGA
Hk2	GCCAGCCTCTCCTGATTTTAGTGT	GGGAACACAAAAGACCTCTTCTGG

Igf1	CACATCATGTCGTCTTCACACC	GGAAGCAACACTCATCCACAATG
Igf1r	GTGGGGGCTCGTGTTTCTC	GATCACCGTGCAGTTTTCCA
Il1b	GAAATGCCACCTTTTGACAGTG	TGGATGCTCTCATCAGGACAG
Il6	CTGCAAGAGACTTCCATCCAG	AGTGGTATAGACAGGTCTGTTGG
Lipa	GCTGGCTTTGATGTGTGGATG	ATGGTGCAGCCTTGAGAATGA
Lipe	GATTTACGCACGATGACACAGT	ACCTGCAAAGACATTAGACAGC
Mgll	CGGACTTCCAAGTTTTTGTCAGA	GCAGCCACTAGGATGGAGATG
Murf1	GCTGGTGGAAAACATCATTGACAT	CATCGGGTGGCTGCCTTT
Myf5	GCCTTCGGAGCACACAAAG	TGACCTTCTTCAGGCGTCTAC
Myf6	ATTCTTGAGGGTGCGGATTTC	CCTTAGCAGTTATCACGAGGC
Myh1	CTCTTCCCGCTTTGGTAAGTT	CAGGAGCATTTCGATTAGATCCG
Myh2	GCACCCATCCTCATTTCGTGA	GGAATGGCACTTGCGTTTAACA
Myh3	CCAAAACCTACTGCTTTGTGGT	GGGTGGGTTCATGGCATACA
Myh4	CTTTGCTTACGTCAGTCAAGGT	AGCGCCTGTGAGCTTGTAAA
Myh7	AGACTGTCAACACTAAGAGGGT	TGCCCCAAAATGGATTCGGAT
Myod	CGGGACATAGACTTGACAGGC	TCGAAACACGGGTCATCATAGA
Myog	GAGACATCCCCCTATTTCTACCA	GCTCAGTCCGCTCATAGCC
Nrf1	AGTGGTATAGACAGGTCTGTTGG	TGTACGTGGCTACATGGACCT
Pgc1α	CCCTGCCATTGTTAAGACC	TGCTGCTGTTCTTGTTTTC
Pparg	GGAAGACCACTCGCATTCCTT	GTAATCAGCAACCATTGGGTCA
Sod2	CAGACCTGCCTTACGACTATGG	CTCGGTGGCGTTGAGATTGTT
Tfam	GGAATGTGGAGCGTGCTAAAA	ACAAGACTGATAGACGAGGGG
Tfb1m	AAGATGGCCCTTTCGTTTATGG	CGACTGTGCTGTTTGCTTCC
Tfb2m	GGCCCATCTTGCATTCTAGGG	CAGGCAACGGCTCTATATTGAAG
Tnfα	ACCCTCACACTCACAAACCA	GGCAGAGAGGAGGTTGACTT

2.8.2 Hematoxylin and eosin staining (H&E)

Snap frozen in 2-methyl butane, SM were sectioned (7 µm) with cryostat CryoStar™ NX50 (Thermo Fisher Scientific, Waltham, MA) and stored at -80°C. Prior staining, the sections were briefly thawed at RT, followed by fixation in ice-cold acetone for 10 min. After air-drying, the sections were rehydrated in PBS for 5 min and then stained with Mayer's hematoxylin solution (Carl Roth, Karlsruhe, Germany) for 2 min, followed by a brief rinse in running tap water. Next, the sections were counterstained with eosin solution (Carl Roth) for 45 s. After another rinse in running tap water, the sections were dehydrated in a graded series of EtOH (70%, 95%, 100%) and cleared in xylene. Finally, the sections were mounted with a coverslip using Dako mounting medium (Agilent Technologies, Santa Clara, CA). The slides were examined under an Olympus BX63 microscope equipped with Olympus DP73 camera for histological evaluation (both Olympus, Shinjuku, Japan).

2.8.3 Electron microscopy

SM samples from chow diet-fed Lal-/- and Wt mice, perfused with PBS, were harvested and fixed in a solution containing 2% paraformaldehyde and 2.5% glutaraldehyde for 2 h. Following fixation, the samples were post-fixed in cacodylate buffer/OsO_4 for an additional 2 h and then washed 4x10 min in phosphate buffer. Subsequently, the samples underwent dehydration and were infiltrated for 3 h with pure epoxy resin (TAAB) and propylene oxide. Afterwards, they were immersed in TAAB twice for 90 min each, transferred into embedding molds, and polymerized (72 h at 60°C). Seventy nm slices were obtained and stained with lead citrate and platinum blue (International Bio-Analytical Industries, Inc., Boca Raton, FL). These slices were then scanned at 120 kV using a Tecnai G2 transmission electron microscope (FEI, Eindhoven, The Netherlands) equipped with a Gatan ultrascan 1000 CCD camera (-20°C; Digital Micrograph acquisition software; Gatan, Munich, Germany). The sample preparations, sectioning, and electron microscopy were performed in collaboration with Prof. Dagmar Kolb, Medical University of Graz.

2.8.4 Immunostaining

Thawed SM cryosections were incubated for 20 min at RT and then dehydrated with PBS for 10 min. Subsequently, the sections were blocked with 0.05% TBST (0.05% Tween 20 in Tris-buffered saline (TBS)) solution containing 10% anti-goat serum to minimize non-specific

binding. The slides were then incubated overnight at 4°C with primary antibodies against anti-MyHCI (MYH7) (#M8421, 1:300; Sigma-Aldrich, St. Louis, MO) or anti-laminin antibodies (#PA1-16730, 1:500, Thermo Fisher Scientific, Waltham, MA) in TBST (269).
C2C12 cells were seeded on glass slides in 24-well plates and fixed with 4% formaldehyde at RT for 20 min. Thereafter, the cells were permeabilized with 0.1% TritonX-100 in PBS for 10 min, washed with TBST 3 times for 10 min and blocked in 5% BSA for 1 h. Then the slides were incubated with primary antibodies against MyHCIIx (MYH1) (#ab51263, 1:300, Abcam, Cambridge, MA) in TBST overnight at 4°C.
For both cryosections and cells in the slides after 3 x washing with TBS for 10 min, the sections were exposed to secondary goat anti-rabbit Alexa Fluor-488 (#A-11008, 1:250) and anti-rabbit Alexa Fluor-594 (#A-11012, 1:250, both Thermo Fisher Scientific) antibodies in blocking solution for 1 h at RT. Subsequently, the sections were incubated with DAPI for 10 min to stain the nuclei. Finally, the slides were mounted using Dako fluorescence mounting medium (Agilent Technologies, Santa Clara, CA) for examination under an Olympus BX63 fluorescence microscope. Images were taken using an Olympus DP73 camera (both Olympus, Shinjuku, Japan). The evaluation of myofiber characteristics involved a comprehensive analysis conducted using Fiji software, an advanced image processing platform that extends the capabilities of ImageJ® Version 1.52d. Within Fiji, the "Muscle morphometry" plugin was employed to meticulously determine parameters such as the cross-sectional area (CSA) and Feret diameter of the myofibers. Moreover, the quantification of the immunofluorescently stained fibers formed from the C2C12 cells was executed utilizing ImageJ software, specifically Version 1.53r (269).

2.8.5 Proteasome activity assay

To determine chymotrypsin-like, trypsin-like, and caspase-like activities of the proteasome activity, we used a fluorometric assay kit II according to the manufacturer's protocol. SM were placed in cold lysis buffer (40 mM Tris pH 7.2, 50 mM NaCl, 2 mM β-mercaptoethanol, 2 mM ATP, 5 mM $MgCl_2$, 10 % glycerol) and homogenized using Precellys. The lysates were then centrifuged at 17,000 *x g* for 20 min at 4℃, and protein concentrations were estimated by Bradford's assay (Bio-Rad Laboratories, Hercules, CA). One hundred fifty µL of 3 mg/mL of protein was added to a black 96-well plate (Greiner Bio-One, Kremsmünster, Austria) in duplicate for each sample. To each lysate-containing well, 50 µL of one of the three substrates (Suc-LLVY-AMC (chymotrypsin-like), Boc-LRR-AMC (Trypsin-like), and Z-LLE-AMC (caspase-like)) diluted to 100 µM in 1X assay buffer was added. A CLARIOstar plate reader

pre-warmed to 37 °C was employed to estimate the released 7-amino-4-methylcoumarin (AMC) fluorescence with excitation/emission filters set at 360/40 nm and 460/40 nm, respectively. The standard curve was used to calculate the absolute amounts of released AMC in each sample (269).

2.8.6 Western blotting

Cell lysates were sonicated twice for 10 s on ice in RIPA buffer containing NP40 (1%) and protease inhibitor cocktail (PIC) (Sigma-Aldrich, St. Louis, MO) to solubilize proteins while preserving their native conformation. SM from young fed mice were lysed in RIPA buffer with NP-40, PIC, and phosphatase inhibitor (Thermo Fisher Scientific, Waltham, MA) 2 x 20 s at 6,500 rpm using Precellys. Subsequently, samples were store on ice for 10 min and centrifuged at 18,000 *x g* and 4°C for 30 min.

Afterwards, 2 µL of each sample was used to estimate the protein concentrations using DC Protein Assay and microplate photometer HiPo MPP-96. Thirty-five µg of protein were then separated by SDS-PAGE and transferred to a PVDF membrane. Anti-mouse antibodies diluted in 5% milk in TBST were applied to block nonspecific binding sites on the membranes and incubated for 1 h. Following this blocking step, detection of the proteins of interest was carried out using monoclonal anti-myosin (MyHCI or MYH7) (#M8421, 1:500 dilution; Sigma-Aldrich, St. Louis, MO) and MyHCIIx (MYH1) antibodies (#ab51263, 1:500, Abcam, Cambridge, MA) to detect myosin expression, while antibodies against phosphorylated Akt (pAKT, Ser473) (#4051, 1:1,000 dilution), total Akt (#9272, 1:1,000 dilution), phosphorylated 4E-BP1 (p4E-BP1) (#2855, 1:1,000 dilution), total 4E-BP1 (#9644, 1:1,000 dilution), phosphorylated AMPKβ (#4181T, 1:1,000 dilution), total AMPKβ1/2 (#4150T, 1:1,000 dilution), and LC3B (#2775S, 1:1000 dilution) were obtained from Cell Signaling (Danvers, MA) for the assessment of signaling pathways. Additionally, GAPDH (#2118, 1:1,000 dilution;), calnexin (#2679T, 1:1,000 dilution, both Cell Signaling), and α-tubulin (NB100-690, 1:1,000 dilution; Novus, Centennial, CO) antibodies were utilized as loading controls to normalize protein expression levels. The secondary anti-rabbit (1:2500, Thermo Fisher Scientific) and anti-mouse antibodies (#P0260, 1:2000, Dako, Agilent Technologies, Santa Clara, CA) conjugated with HRP were used to obtain the protein bands on the membranes. The final images were received by applying the Clarity™ Western ECL Substrate Kit to the membranes and visualized with the ChemiDoc imaging system (both Bio-Rad Laboratories) (269).

2.8.7 Amino acid quantification by high-performance liquid chromatography

Seventy µL of plasma collected from chow-fed and 12 h fasted mature female Lal-/- and Wt mice was mixed with 50 µL of 1.5 M $HOCl_4$ and vortexed for 2 min at RT. Following this, 1.125 mL of water was added to the samples, along with 25 µL of 2 M K_2CO_3, and vortexed again. The mixture was centrifuged at 3,000 *x g* for 5 min, after which the supernatant was carefully removed and stored at -80°C. For derivatization, the o-phthalaldehyde (OPA) reagent was utilized. High-performance liquid chromatography (HPLC) was conducted with a liquid chromatograph (Shimadzu, Kyoto, Japan) with specific conditions. Mobile phase A consisted of 0.1 M sodium acetate (pH 7.2), prepared by combining sodium acetate, water, HCl, methanol, and tetrahydrofuran (THF); the mobile phase B was composed of methanol. The entire process was carried out using a Waters 717 plus autosampler (Waters, Milford, MA) and LC20AD Shimadzu pumps. The HPLC conditions were as follows: A gradient of mobile phases A and B was applied over time, with varying percentages of each. The flow rate was set at 1.1 ml/min. The gradient program is described in Table 9. Analysis was conducted using a Supelcosil LC18 3 µm, 150 x 4.6 mm column (Supelco™ Analytical, Sigma-Aldrich, Saint Louis, MO) with detection by a scanning fluorescence detector (excitation :340 nm, emission: 455 nm). An autosampler set to addition mode with a delay time of 1 min, mixed 25 µL of sample with 25 µL of OPA reagent (269). This experiment was performed in collaboration with Prof. Wolfgang Sattler and Helga Hinteregger, Medical University of Graz.

Table 9. The gradient program for amino acid separation by high-performance liquid chromatography.

	Time [min]										
Mobile Phase	0	15	20	24	26	34	38	40	42	42,1	49
A [%]	86	86	70	65	53	50	30	0	0	86	86
B [%]	14	14	30	35	47	50	70	100	100	14	14

2.8.9 Metabolome analysis using nuclear magnetic resonance (NMR) spectroscopy

Sample preparation

Metabolomics analysis by NMR spectroscopy was performed following the protocol described previously (270). Specifically, 30-50 mg of either enriched in oxidative “red” or glycolytic “white”

fibers segments of GA were lysed and mixed with ice-cold methanol and MilliQ H_2O (2:1). The samples were then homogenized 2x for 20 s using a Precellys. Following centrifugation at 12,300 *x g* for 30 min at 4 °C, the supernatants were carefully transferred to new tubes and lyophilized at <1 Torr, 850 rpm, 25°C for 10 h in a vacuum-drying chamber equipped with a cooling trap and vacuum pump (Savant Speedvac SPD210 vacuum concentrator, Savant RVT450 refrigerated vapor trap, VLP120 vacuum pump; Thermo Fisher Scientific, Waltham, MA, USA). Subsequently, the dried samples were reconstituted in 500 µL of NMR buffer, composed of D_2O and 0.08 M Na_2HPO_4, 4.6 mM 3-(trimethylsilyl) propionic acid-2,2,3,3-d4 sodium salt (TSP), 0.04% (w/v) NaN_3 (pH 7.4). NMR spectroscopy was performed using a Bruker AvanceTM Neo 600 MHz spectrometer equipped with a TXI probe head (Bruker, Rheinstetten, Germany), operating at a temperature of 310 K. One-dimensional proton (^1H) NMR spectra were acquired using the Carr–Purcell–Meiboom–Gill (CPMG) pulse sequence (cpmgpr1d), comprising 512 scans, 73728 points in F1, 12019.230 Hz spectral width, 1024 transients, and a recycle delay of 4 s, with pre-saturation for water suppression.

NMR data analysis

NMR spectra processing involved several steps: Fourier transformation of the free induction decay (FID), automatic phasing, and baseline correction using Bruker Topspin software version 4.0.2. Subsequently, in Matlab version 2014b, peaks near water, TSP, and methanol signals were removed, spectra were aligned, and probabilistic quotient normalization was applied. Chenomx NMR Suite 8.4 was utilized for metabolite identification, and signal integration of normalized spectra was performed for quantification (271). Representative peaks for each metabolite were selected, and integration areas were determined using an R script in RStudio 2023 with R version 4.1.3, providing values in arbitrary units (a.u.) proportional to metabolite concentrations. MetaboAnalyst 5.0 facilitated principal component analysis (PCA), orthogonal partial least squares discriminant analysis (O-PLS-DA), and partial least squares discriminant analysis (PLS-DA) (272). Quality evaluation, assessed by the Q2 statistics, confirmed the statistical significance of variations, with a maximum value of 1 indicating consistency between original and projected data, offering insights into cross-validation. This experiment was performed in collaboration with Prof. Tobias Madl and Hansjörg Habisch, Medical University of Graz.

2.8.10 Measurement of ATP by mass spectrometry

QU samples from young male mice, approximately 25 mg each, were homogenized in 500 µL of 80% methanol with internal standards (670 pmol of glutarate and 168 pmol of deuterium-labeled glycocholic acid (Sigma-Aldrich, St. Louis, MO) using a Bioruptor Pico sonicator (sonication conditions: 30 min at 4°C, alternating between 30 s on and off, at a high-frequency setting) (Diagenode, Denville, NJ). To this mixture, 300 µL of double-distilled water and 900 µL of methyl tert-butyl ether (MTBE) were added, followed by a 15-min incubation at 4°C. Afterwards, the samples were centrifuged at 18,213 *x g* for 10 min at 4°C. Subsequently, 800 µL of the resulting upper phase was carefully removed and replaced by 800 µL of a synthetic upper phase mixture made of MTBE, methanol, and water in a 9/4/4 volume ratio. Following a second round of incubation and centrifugation under the same conditions, the entire upper phase was collected. The lower phase of 800 µL was then harvested and dried using a SpeedVac concentrator (Thermo Fisher Scientific, Waltham, MA). For analysis by liquid chromatography/mass spectrometry, the water-soluble metabolites were reconstituted in 100 µL of 70% acetonitrile (ACN) containing 0.5 mM medronic acid. The remaining tissue was desiccated, dissolved in 0.3 N sodium hydroxide at 55°C for roughly 4 h, and the protein concentration was measured using the Pierce™ BCA assay kit (Thermo Fisher Scientific) according to the instructions provided by the manufacturer. For external calibration, a range of ATP solutions, from 20 pmoles to 200 nmoles (Sigma-Aldrich), were provided in 500 µL of 80% methanol solution that contained an internal ATP standard solution. The preparations were then subjected to the same processing steps as detailed earlier.

Separation of the metabolites was carried out on a Vanquish UHPLC+ system (Thermo Fisher Scientific). An ACQUITY UPLC BEH Amide column (2.1 x 150 mm, 1.7 µm particle size; Waters, Milford, MA) was utilized for this purpose. An 18-min gradient was applied at a flow rate of 400 µL per min, transitioning from 97% of solvent A (a mixture of ACN and ddH_2O (95:5, v:v)), with 10 mM ammonium formate and 10 mM ammonium) down to 65% of solvent B (which is ddH_2O and ACN, 95;5, v:v, containing 20 mM ammonium formate and 20 mM ammonium). A QExactive Focus mass spectrometer (Thermo Fisher Scientific), incorporating a heated electrospray ionization source, was utilized for the detection of metabolites. Operated in negative data-dependent acquisition mode scanning a mass-to-charge (m/z) range of 60 to 900, the equipment was used to identify ATP by matching the accurate mass-to-charge ratio of the [M-H]- ion (with a deviation less than 5 parts per million) to that of a synthetic reference (Sigma-Aldrich), alongside a comparison of retention times and MS2 spectral data.

In the analysis, blank values were subtracted from ATP peak areas, followed by normalization to the internal standard. Quantification was then carried out by comparing ATP/standard ratios to an external calibration curve. To standardize ATP concentrations across samples, the values were further normalized using the wet weight of each respective sample (269). This experiment was performed in collaboration with Thomas O. Eichmann, Core Facility Mass Spectrometry, Medical University of Graz.

2.8.11 2-Deoxy-D-glucose uptake

Lal-/- and their Wt littermates were fasted for 6 h, after which the animals were injected intraperitoneally with 10% 2-deoxy-D-glucose solution in PBS containing 2 µCi [^{3}H]-2-deoxy-D-glucose (Hartmann Analytic GmbH, Germany)/30 g body weight. Blood was taken at 15 and 60-min post-injection, the animals were sacrificed 60 min post-injection, and the organs were removed. Plasma was isolated from blood by centrifugation at 5,205 x *g* at 4°C for 7 min, and the radioactivity was measured from 20 µL of plasma by liquid scintillation counting (4 ml scintillation cocktail) using a liquid scintillation analyzer. The tissues were lyophilized for 48 h, after which the dry weight was measured. Subsequently, liver and SM were digested in 1 mL of 1 M NaOH overnight at 65°C. The digested material was transferred into scintillation vials containing 8 mL of scintillation cocktail, mixed properly, and kept at 4°C overnight. The radioactivity was determined by liquid scintillation counting and normalized to dry tissue weight (269).

2.8.12 Lipid extraction and biochemical analysis

SMs from mice were lysed using Precellys in lysis buffer (100 mM potassium phosphate, 250 mM sucrose, 1 mM EDTA, pH 7). The protein amount was determined after centrifugation according to the method of Lowry by using the DC Protein Assay. For lipid extraction, 1 (for QU, TA, and GA) or 0.5 mg (for SO) of protein were used following Folch's method. Briefly, 20-fold excess of chloroform/methanol (2:1) was added to the samples and the vials were rotated for 2.5 h at RT. After centrifugation at 1250 x *g* for 15 min at 4°C, PBS (0.2-fold) was added to the supernatant. The samples were mixed and centrifuged again at 1,250 x *g* for 15 min at 4°C. The lower phase was transferred to a new vial and dried under nitrogen gas after the addition of 200 µL 2% Triton X-100 in chloroform. The residue was dissolved in 100 µL ddH_2O for 20 min in an ultrasound water bath (269).

For lipid extraction from C2C12 cells, they were washed 3 times with ice cold PBS, which was then carefully removed. Lipids were extracted with 1 mL of ice cold hexane:isopropanol (3:2) at 4°C for 2 h, followed by the addition of 15 µL of 10% Triton-X100 (in isopropanol) to each sample vial. The liquid was evaporated under nitrogen gas, diluted in 150 µL of deionized water, vigorously mixed, and incubated in a water bath (45°C) for 40 min.
Thereafter, TG, TC, and FC concentrations were determined using enzymatic kits and a microplate photometer HiPo MPP-96 following the manufacturer's protocol. For lipid extracts from cells, the reagents were combined with sodium 3,5-dichloro-2-hydroxy-benzenesulfonate (SDHC) as enhancer of the reaction. CE concentrations were calculated by subtracting FC from TC. These values were normalized to protein concentrations (269).

2.8.13 Oil Red O (ORO) staining

For lipid staining, a stock solution was prepared by combining 0.5 g ORO (Sigma-Aldrich, St. Louis, MO) with 100 mL of isopropanol. The ORO working solutions (30 mL of filtered stock and 20 mL ddH_2O, mixed for 10 min, filtered) was freshly prepared before use and added for 1 h. Cryosections (7 µm) from snap frozen SM thawed at RT for 20 min were fixed in 10% formalin for 30 s and then briefly washed with distilled water. C2C12 cells were washed with PBS and fixed with 4% formaldehyde for 20 min at RT. Subsequently, slides were incubated in PBS for 5 min, followed by 90% isopropanol for another 5 min. The samples were then incubated with the working ORO solution for 1 h, followed by an incubation in 70% isopropanol for 1 min, and finally rinsed with distilled water. Nuclei were stained for 10 min with Mayer's Hematoxylin (Carl Roth, Karlsruhe, Germany) and afterwards slides were mounted with Dako mounting medium (Agilent Technologies, Santa Clara, CA). Images were taken on an Olympus BX63 microscope equipped with an Olympus DP73 camera (both Olympus, Shinjuku, Japan).

2.8.14 Fatty acylcarnitine analysis by mass spectrometry

Lipids were extracted from 5-15 mg of SM powder obtained from juvenile (8-12 weeks old) fasted male Lal-/- and Wt mice according to Matyash et al. (273). Briefly, samples were ground using a Mixer Mill with two 6-mm steel beads (Retsch, Haan, Germany) at high frequency for two intervals of 10 s. The homogenization medium was 700 µL of a solution containing methyl tert-butyl ether (MTBE) and methanol (3:1). This solution also included 500 pmol of butylated hydroxytoluene, 1% acetic acid, and 3 pmol of ^{13}C-labeled palmitoyl-L-carnitine (Sigma-Aldrich, Saint Louis, MO), all serving as internal standards. The samples underwent lipid

extraction through vigorous shaking for 30 min at RT. Subsequently, 140 µL of dH_2O was added and the samples were extensively vertexed, followed by centrifugation at 1,000 *x g* for 15 min. Thereafter, the upper organic layer, approximately 500 µL, was collected, and any solvents were evaporated using nitrogen gas. The lipids were then reconstituted in 500 µL of MTBE/methanol at the same ratio described above, then diluted 5-fold with a mixture of isopropanol, methanol, and distilled (7:2.5:1) for further analysis with an ultra-high-performance liquid chromatography triple quadrupole system (UHPLC-QqQ). The remaining protein sediments were dried, lysed in 300 µL of 0.3 N sodium hydroxide at 60°C, and its protein content was measured.

The chromatographic separation was carried out utilizing a 1290 Infinity II LC system (Agilent, Santa Clara, CA), featuring a Zorbax RRHD Eclipse Plus C18 column (2.1 x 50 mm, 1.8 µm; Agilent). A gradient elution approach spanning 10 min was employed, transitioning from 95% solvent A (H_2O; 10 mM ammonium acetate, 0.1% formic acid, 8 µM phosphoric acid) to 100% solvent B (2-propanol; 10 mM ammonium acetate, 0.1% formic acid, 8 µM phosphoric acid) at a flow rate of 500 µL/min. The column temperature was maintained at 50°C throughout the analysis. The lipid species were detected in positive ionization mode using a 6470 triple quadrupole mass spectrometer (Agilent) equipped with an electrospray ionization (ESI) source. Acylcarnitine species were analyzed by dynamic multiple reaction monitoring ([M+H] + to m/z 84.9, CE 28, Fragmentor 164, CAV 5). Data acquisition and data processing was done by MassHunter Data Acquisition software (Version 10.0 SR1, Agilent) and MassHunter Workstation Quantitative Analysis for QQQ (Version 10.0, Agilent), respectively. Data were normalized for recovery, extraction-, and ionization efficacy by calculating analyte/ internal standards ratios (AU) and expressed as AU/µg protein (269). Lipid extraction, separation and final quantifications were performed in collaboration with Thomas O. Eichmann, Medical University of Graz.

2.8.15 Assessment of mitochondrial respiration and FAO

Mitochondrial respirometry and FAO in permeabilized SM fibers was estimated by Oxygraph-2k (O2k) high-resolution respirometer following the manufacturer's protocol (274). The procedure began with the excision of the enriched in oxidative fibers from GA. The removed section of SM was then sliced into small parts, each weighing between 10 to 20 mg. These samples were placed into a Falcon tube containing 10 mL of an ice-cold BIOPS preservation solution (10 mM Ca^{2+}-EGTA buffer, 20 mM imidazole, 50 mM potassium-4-morpholineethanesulfonic acid (MES), 0.5 mM dithiothreitol, 6.56 mM $MgCl_2$, 5.77 mM ATP,

15 mM pCr, pH 7.1). The muscle sample in the BIOPS solution in a small Petri dish were placed on ice. All connective tissue was carefully removed using a pair of sharp forceps to ensure that only the muscle tissue is subjected to further analysis.

Afterwards, the dissected GA part was separated to small bundles (each approximately 0.5–1 mg) and then transferred into a plastic Petri dish, in which individual fibers were mechanically separated using 2 pairs of sharp forceps and a dissection microscope (Olympus SZ40; Olympus Optical, Tokyo, Japan). The separated fibers were transferred to BIOPS buffer containing saponin (50 µg/mL) and incubated for 30 min at 4°C on a shaker. Afterwards, saponin was washed off the permeabilized fibers for 10 min in respiration medium (MiRO6; 110 mM D-sucrose, 60 mM lactobionic acid, 0.5 mM EGTA, 3 mM $MgCl_2$, 20 mM taurine, 10 mM KH_2PO_4, 20 mM HEPES, 1 g/L bovine serum albumin and ~280 U/mL catalase) at 4°C. One to 3 mg of fibers were transferred into a calibrated respirometer containing 2 mL of respiration medium (MiRO6) at 37°C in each chamber to preserve mitochondrial activity.

To assess mitochondrial respiratory capacity using non-saturating substrates that support oxidative phosphorylation, the substrate-uncoupler-inhibitor titration (SUIT-011) protocol was applied. The use of substrates such as glutamate and malate (10 mM each) allows the study of the NADH-linked substrate pathway control state (non-phosphorylating electron transfer (LEAK) respiration). Once a stable state oxygen consumption rate was reached, the ADP-activated state of oxidative phosphorylation (OXPHOS) was measured in the presence of 5 mM ADP-Mg^{2+}. The integrity of the mitochondrial membrane was estimated after adding cytochrome C (10 µM). Thereafter, respiration was further stimulated by adding 10 mM succinate, activating the convergence of electrons from complex I + II, followed by 1 µM uncoupler carbonyl cyanide m-chlorophenylhydrazone (CCCP). Finally, inhibition of complex I with rotenone (0.5 µM) allowed us to measure electron transfer capacity through complex II, whereas antimycin A (2.5 µM), an inhibitor of complex III (all components from Sigma-Aldrich, St. Louis, MO), was utilized to assess and adjust residual oxygen consumption capacity, implying non-mitochondrial oxygen consumption.

To estimate mitochondrial function during FAO, we applied the SUIT-005 protocol with minor modifications. The following substrates and inhibitors were added sequentially after the oxygen slope was stable: 100 µM palmitoylcarnitine and 2 mM malate (basal respiration and respiratory stimulation of the FAO pathway) followed by 25 mM ADP, 10 µM cytochrome C, 5 mM pyruvate (respiratory stimulation by simultaneous action of the FAO pathway and the NADH electron transfer pathway), 10 mM succinate, 1 µM CCCP, 0.5 µM rotenone, and 2.5 µM antimycin (all Sigma-Aldrich).The respiration signals were analyzed using the O2k-6 software DatLab (269).

2.8.16 Quantification of mitochondria

The number of mitochondria was estimated by determining the ratio of mitochondrial to nuclear DNA as previously described (275). Briefly, genomic DNA from SM was incubated with DNA extraction buffer (100 mM NaCl, 25 mM EDTA, 10 mM Tris-Cl, 0.5% SDS, 1 mg/mL proteinase K, pH 8) overnight at 55 °C. Thereafter, DNA was extracted with phenol:chloroform:isoamyl alcohol (25:24:1, v:v:v). The concentration of extracted DNA was estimated by NanoDrop and diluted to 10 ng/µL for qPCR amplification. A comparison of *16S* (mitochondrial gene) expression relative to hexokinase 2 (*hk2*, nuclear gene) DNA expression was used to estimate the ratio between mtDNA to nDNA copy numbers (269).

2.8.17 MCP1 enzyme-linked immunosorbent assay (ELISA)

Levels of the inflammatory factor MCP1 (CCL2) were measured with an ELISA kit (DY479, R&D Systems, Minneapolis, MN) following the manufacturer's protocol. For plate preparation, the capture antibody was diluted in 0.5 mL PBS without carrier protein and then used to coat a 96-well microplate with 100 µL per well, followed by overnight incubation at RT. After aspiration and washing of each well with washing buffer, the plate was blocked with 300 µL reagent diluent per well for 1 h at RT. Subsequently, samples and standards were added in reagent diluent, and the plate was incubated for 2 h at RT. The detection antibody, diluted in reagent diluent, was then added to each well, followed by another 2 h of incubation. Streptavidin-HRP was applied to each well and incubated for 20 min at RT, after which the substrate solution was added and incubated for an additional 20 min. The final step involved the application of stop solution to each well, and subsequently, the optical density of the samples was measured at 450 nm using the CLARIOstar spectrophotometer. Quantification was performed by comparing the absorbance of the samples to the absorbance of the standards using a generated standard curve.

2.8.18 Analyses of the SM proteome

Sample preparation and processing for proteomics analysis

The segments enriched in oxidative or glycolytic fibers from GA were homogenized in lysis buffer composed of 100 mM Tris-HCl, 1% SDS, 10 mM Tris(2-carboxyethyl)phosphine, and 40 mM chloroacetamide (pH 8.5) by Bead Mill Max (VWR International GmbH, Darmstadt, Germany). The samples were then reduced and alkylated at 95°C for 10 min and centrifuged

at 7,000 *x g* and 4°C for 5 min. Fifty µg of each sample was precipitated with acetone, dissolved in 50 mM Tris-HCl (pH 8.5), and digested with trypsin/endoproteinase Lys-C mixture (Promega, Madison, WI) at 37°C overnight with constant shaking. Subsequent to the initial preparation, the peptide solution, containing 4 µg of proteins, was acidified by adding trifluoroacetic acid to reach a final concentration of 1%. Following the acidification, the peptides were further purified and desalted using homemade stage-tips. These stage-tips were packed with styrenedivinylbenzene reversed-phase sulfonate, which is effective for this purpose. The use of this method helps in removing salts and other contaminants, thereby preparing the peptides for subsequent mass spectrometry (269).

Proteome analysis by liquid chromatography-tandem mass spectrometry (LC-MS/MS)

Further analysis was performed on the UltiMate™ 3000 RSLCnano Dionex system (ThermoFisher Scientific, Waltham, MA) utilizing an IonOpticks Aurora Series UHPLC C18 column (250 mm x 75 µm, 1.6 µm) (IonOpticks, Fitzroy, Australia). This was achieved through an 86.5-min gradient at a flow rate of 400 nL/min, with the system maintained at 40°C. The gradient consisted of solvent A (0.1% formic acid in water) and solvent B (acetonitrile with 0.1% formic acid), with the following profile: 0-5.5 min: 2% B; 5.5-25.5 min: 2-10% B; 25.5-45.5 min: 10-25% B; 45.5-55.5 min: 25-37% B; 55.5-65.5 min: 37-80% B; 65.5-75.5 min: 80% B; 75.5-76.5 min: 80-2% B; 76.5-86.5 min: 2% B.

The timsTOF Pro mass spectrometer (Bruker Daltonics GmbH, Bremen, Germany) was operated in positive mode and utilized trapped ion mobility spectrometry (TIMS). The instrument operated at a 100% duty cycle with a ramp of 100 ms. The source capillary voltage was set to 1600 V, and a dry gas flow of 3 L/min at 180°C was maintained. Scan mode employed data-independent parallel accumulation–serial fragmentation (DIA-PASEF) as previously described (276), utilizing 21 x 25 Th isolation windows spanning m/z 475 – 1,000 with 0 Th overlap between windows. Following the MS1 scan, two and three isolation windows were fragmented per TIMS ramp, resulting in an overall DIA cycle time of 0.95 s (269).

LC-MS/MS proteomics data processing, bioinformatics, and statistical analysis

Data-Independent Acquisition by Neural Networks (DIA-NN) software (version 1.8.1) was used to process the raw data files and perform protein quantification (277, 278). For the library-free search, the SwissProt Mus musculus proteome database in fasta format was utilized. This database comprised a comprehensive collection of mouse protein sequences, including 17,219 sequences, and also incorporated sequences for common contaminants. The version used was downloaded on August 17, 2021. The search parameters included a false discovery

rate (FDR) threshold of 1% to ensure high confidence in the identification of proteins and minimize the inclusion of incorrect matches. For the analysis using DIA-NN software, deep learning algorithms were used to enhance the prediction of both the mass spectra and retention times for the peptides. These settings are part of the software's capabilities to accurately predict how peptides and their fragments behave in the mass spectrometer based on their sequences and modifications. The m/z range for the fragment ions was set between 200 and 1800, which defines the window within which the software will consider the data for analysis. This range is selected to ensure that the most informative and detectable ions are included while excluding less useful data. N-terminal methionine excision refers to the cleavage of the initial methionine residue from proteins during or after their synthesis in the cell. This biological process was considered in the analysis, likely improving the match between observed peptide sequences and those predicted by the software. The settings also included the tolerance for up to 2 missed cleavages by trypsin, a proteolytic enzyme commonly used in proteomics workflows to digest proteins into peptides. Missed cleavages occur when trypsin does not cleave at every expected site, usually at the carboxyl side of lysine or arginine amino acids. Lastly, the lengths of peptides considered for the analysis were constrained to a range of 7 to 30 amino acids. This restriction ensures that the search is focused on peptides of an appropriate size for detection and analysis by the mass spectrometer, enhancing the reliability of the protein identification and quantification process. Further, in the analysis with the DIA-NN software, cysteine carbamidomethylation was set as a fixed modification, meaning that all cysteine residues in the protein sequences were assumed to be carbamidomethylated. This is a common modification applied during sample preparation to prevent the formation of disulfide bonds between cysteine residues. Methionine oxidation was considered a variable modification, implying that some methionine residues may be oxidized while others are not. During the mass spectrometry analysis, DIA-NN considers both the unmodified and oxidized forms of methionine when identifying and quantifying peptides. The DIA-NN software also has the capability to optimize mass accuracy settings based on the data. In this case, the software used the data from the first run of the experiment to automatically adjust the mass accuracy parameters, which helps in improving the confidence of peptide identifications. For post-processing of the data, including functional analysis and visualization of protein group quantities, different software tools were used. Perseus software (version 1.6.15.0) was utilized for processing protein group quantities. Additionally, Jupyter Notebook with Python (version 3.9) was employed for custom data analysis and scripting purposes. Finally, Cytoscape, a software platform for visualizing molecular interaction networks and biological pathways, was also used in the analysis. To ensure the inclusion of proteins that might be present in low

abundance in either Wt or Lal-/- mice and not discarded due to their absence in some samples, a specific filtering approach was applied. The criteria required that proteins must have at least 4 valid measurements out of 5 or 6 samples in one of the groups to be retained for further analysis. This approach reduces the likelihood of excluding proteins that are truly present but not detected in certain conditions due to low expression levels. For any missing values that still existed after this filtering, an imputation strategy was employed. The missing values were replaced with random values drawn from a Gaussian (normal) distribution that was adjusted to be slightly wider and shifted downwards (width of 0.3, downshift of 1.8). Imputing data in this way is a common practice in proteomics to manage missing data that may occur because the protein abundance falls below the detection limit. PCA was performed on the normalized (z-scored) data to reveal the most significant sources of variation within the experiments and visually interpret relationships within the data. PCA was visualized using Jupyter Notebooks in combination with various Python packages, such as Pandas, Numpy, Matplotlib, Sklearn, Seaborn, and Bioinfokit. For statistical validation, two-sample t-tests were conducted to identify differences between groups, with an additional correction for multiple hypothesis testing using a permutation-based FDR approach to control for type I errors. The settings for the statistical test included S0 (a parameter that may set a small fold change cut-off value) at 0.1 and the FDR threshold at <0.01 to ensure statistical significance of the protein group differences (269). Lastly, functional enrichment analyses were carried out on the log2-fold changes of protein expressions. This was done using the PANTHER (279, 280). Proteomics was performed in collaboration with Prof. Ruth Birner-Gruenberger and her team, Technische Universität Wien, Austria.

2.8.19 Hanging wire test

The motoric test (hanging wire test) was performed as previously described (281) with minor adaptations. The system consisting of a thick metal wire fixed onto two vertical strands with bedding materials in the bottom of the supporting cage was kindly borrowed from Prof. F. Madeo's group, University of Graz. The experiment started when the mouse placed on the wire was able to hang and ended at the time point when the mouse fell off. The test was conducted in triplicate for each mouse. Mice hanging for longer than 5 min were excluded from final calculations.

2.8.20 Measurement of maximum O_2 consumption (VO_2max) and peak effort testing using treadmills

The effort tolerance of Wt and Lal-/- mice, peak effort, and maximal oxygen uptake (VO_2max) were studied under carefully controlled experimental conditions, using a motorized treadmill coupled to a calorimetric unit with a gas analyzer. Before the treadmill experiment, animals were kept in their cages for 1 h with *ad libitum* access to food and water. The mice were positioned individually in a switched-off closed treadmill chamber with the electrifying grid already active before the test was performed. The intensity of the electric stimulus was set to 2.5 mA and 0.5 s. Each chamber was connected to a gas analyzer for instant O_2 measurements throughout the experiment. The experimental animals were given approximately 2.5 min to freely explore the treadmill, at least until each mouse has explored its path and/or received at least one electric shock from the grid. The treadmill was then activated and the speed slowly increased to approximately 0.15 to 0.3 m/s. Once the mice began to run, the speed was slowly increased every 30 s for 0.01 m/s. The test was stopped when the mouse reached maximal exhaustion, which was defined as an animal's inability to maintain the running speed for approximately 5 s despite being in touch with the electrical grid. The moment at which oxygen intake reached a plateau during a workout/exercise was used to assess VO_2max and running distance. The ultimate running distance multiplied by body weight and divided by 1,000 was used to determine the maximum workload. Tissues were collected 2-3 h post exercises (269). This experiment was performed in collaboration with Prof. Simon Sedej, Medical University of Graz.

2.8.21 Cholesteryl ester and triglyceride hydrolase activity assays

C2C12 cells were lysed either in a citrate buffer (pH 4.2) containing 54% of 100 mM citric acid monohydrate and 46% of 100 mM trisodium citrate dehydrated, pH 4.2, or phosphate lysis buffer (pH 7) containing 0.25 M sucrose, 0.1 M KH_2PO_4, 1 mM EDTA, and 1 mM DTT. Then acid and neutral CE hydrolase (CEH) and TG hydrolase (TGH) activities were determined in C2C12 cell lysates as previously described (236). Briefly, cells were sonicated shortly on ice (2 x 10 s), and centrifuged at 1,000 *x g* at 4°C for 10 min. Protein concentrations were estimated in the supernatant using DC Protein Assay and microplate photometer HiPo MPP-96. Once the protein concentration is determined, an aliquot of the supernatant was taken such that it contains 50 µg of protein. This aliquot is then diluted with citrate buffer or 0.1 M potassium-phosphate buffer to reach a final volume of 100 µL. The substrate for measuring

CEH activity contained 0.2 mM cholesteryl oleate/sample, 0.04 µCi/sample cholesteryl [1-^{14}C]-oleate (Amersham Biosciences, Piscataway, NJ), and 455 µM mixed micelles in the ratio 3 to 1 of phosphatidylcholine (PC) and phosphatidylinositol (PI) (Amersham Biosciences). The substrate for the TGH activity assay contained 300 µM triolein/sample, 0.5 µCi/sample [9,10-^{3}H(N)]-triolein (Perkin Elmer, Waltham, MA), and 45 mM of PC/PI mixed micelles.
The samples mixed with substrates were incubated in the water bath for 1 h at 37°C under constant shaking. The reaction was terminated by the addition of 3.25 mL stop solution with a mixture of methanol, chloroform, and n-heptane (10:9:7, v:v:v) followed by the addition of 1 mL of 0.1 M potassium carbonate at pH 10.5. After vortexing and centrifugation at 800 *x g* for 15 min at 4 °C, the radioactivity was measured in 1 mL of the upper phase by liquid scintillation counting, and then the release of FA was calculated as described previously (282).

2.8.22 MTT assay

C2C12 cells in 12-well plates were washed twice with PBS. Thereafter, the cells were incubated with 250 µL of MTT (3-(4,5-dimethylthiazol-2-yl)-2,5-diphenyltetrazolium bromide) stock solution (5 ng/mL) dissolved in 1 mL cell culture medium for 90 min. Afterwards, the medium was sucked and 300 µL of ice-cold lysis solution (0.04 M HCl in isopropanol) was added to all wells. The plate was shaken for 10 min at RT and 200 rpm in the dark. The absorbance of each well was measured at 570 nm and 630 nm and absorption spectra were recorded using a microplate reader CLARIOstar.

2.8.23 Estimation of the proliferation rate of C2C12 cells and primary myoblasts

Fifty thousand cells/well for C2C12 and 20,000 of primary myoblasts were seeded into 12-well plates. After adhering overnight, the initial cell number was determined from reference wells following trypsinization. Then the experimental wells were washed with PBS at least twice and media containing Lalistat-2 (0.1 µM) or the respective amount of EtOH (final concentration: 0.1%) was applied to C2C12 cells. The cells were counted after 6 h (for C2C12 cells) and after 24 h for primary as a starting point. The final cell numbers were counted after 24 and 72 h for C2C12 cells. For primary myoblasts, the cells were counted after 72 h and 96 h. For this purpose, the cells were harvested using 150 µL of 0.5% Trypsin-EDTA, collected by centrifugation at 200 *x g* for 5 min at RT, and resuspended in 550 µL fresh media. The cell suspension was diluted 1:1 in trypan blue (ThermoFisher Scientific, Waltham, MA) and counted with a hemocytometer. The final number of cells was quantified as the average

number of cells in each of the 16 corner squares, multiplied by 10,000 to account for the dilution and grid area, and finally, multiplied by 2 to correct for the 1:1 dilution from the trypan blue addition.

2.8.24 FAO assay

FAO using [1-^{14}C] palmitic acid (PA) and isolated primary myoblasts from Lal-/- mice and the respective Wt littermates was performed as previously described with minor modifications (283). In brief, 45.000 primary myoblasts were seeded in gelatine-coated T-25 flasks in the upright position and grown in growth medium until confluency, after which the cells were differentiated to myoblasts using differentiation medium for 3 days. Thereafter, the cells were washed with warm PBS and incubated for 1 h at 37 °C with 1 mL of substrate containing 100 µM PA, 0.4 µCi [$^{1\text{-}14}$C]-PA, 0.5 mM carnitine, and 0.3% BSA in DMEM (glucose-, pyruvate- and glutamine-free) in flasks that were sealed with a rubber stopper and contained a hanging basket with a saturated filter (50 µL of 1 M NaOH). The reaction was stopped by adding 100 µL of 70% perchloric acid, and the released CO_2 was trapped at 37°C for 2 h, after which the radioactivity trapped in the filter was measured. The values determined in the presence of 100 µM etomoxir (CPT1 inhibitor) served as a negative control. The radioactivity captured by the filter paper was quantified using liquid scintillation counting and the results were normalized to the number of seeded cells.

2.8.25 Mitochondrial stress test by Seahorse analysis

C2C12 cells were plated at a density of 2,000 cells/well in Seahorse XFe 96-well culture microplates (Agilent, Santa Clara, CA) and cultured in differentiation media either with EtOH or Lalistat-2 (0.1 µM) for 6 days before being assayed as described previously (284). Briefly, prior to the assay, the cells were washed with basal assay medium (Agilent) in the presence of 10 mM glucose, 2 mM glutamine, 1 mM sodium pyruvate, 200 nM insulin, and 60 µM oleic acid-BSA (all Sigma-Aldrich, St. Louis, MO). A mitochondrial stress test was performed through the sequential injection of oligomycin (2 µM, port A), FCCP (2 µM, port B), and antimycin A/rotenone (1 µM) in combination with Hoechst dye (10 µM, Port C) (all Sigma-Aldrich). Cell counts/well were measured on the Biotek Cytation cellular imaging system, and data were normalized utilizing the Seahorse XF Imaging and Cell Counting software (both Agilent). The experiment was performed with the help of Prof. Elizabeth Rendina-Ruedy and her team and facilities from Vanderbilt University Medical Center during my stay abroad.

2.8.26 Statistical analyses

The statistical analyses for NMR and proteomics data are described in the respective paragraphs. For the remaining data, the statistical analyses and illustrations were done using GraphPad Prism 9.0 (GraphPad Software Inc, San Diego, CA). The significance of two group comparisons was established using the unpaired Student's t-test. When comparing multiple groups, one-way ANOVA was used first, followed by Bonferroni or Tukey post-hoc test. The data were presented as mean values with their related standard deviations (either ± SD or +SD). The degrees of statistical significance were marked with asterisks (or another symbol dependent on the control as described in the specific results section): * $p < 0.05$, ** $p \leq 0.01$, and *** $p \leq 0.001$ (269).

3. Results

3.1 *Lipa* mRNA expression in SM and C2C12 myoblast cells

In previous studies, it was suggested that the expression of *Lipa* in SM and cardiac muscle is relatively low compared to other organs such as the liver, spleen, lungs, brain, and small intestine (208). However, studies of *Lipa* mRNA levels in different types of SM have not been performed. Notably, *Lipa* expression was higher in SM with a predominance of slowly oxidative fibers such as *soleus* (SO) (Ct ≈27-28), compared with muscles enriched in glycolytic fibers like *quadriceps* (QU), *tibialis anterior* (TA), and *gastrocnemius* (GA) (Ct ≈28-29) (Fig. 7A). *Lipa* expression in the liver was determined as control (269).

In addition, I examined *Lipa* expression in C2C12, a mouse myoblast cell line, as a potential *in vitro* model to study the role of LAL in SM formation. We observed an increased expression of the *Lipa* gene during myotube differentiation (Fig. 7B). Interestingly, the Ct values for *Lipa* in C2C12 cells (Ct ≈24-25) were higher compared to those in SM from adult mice.

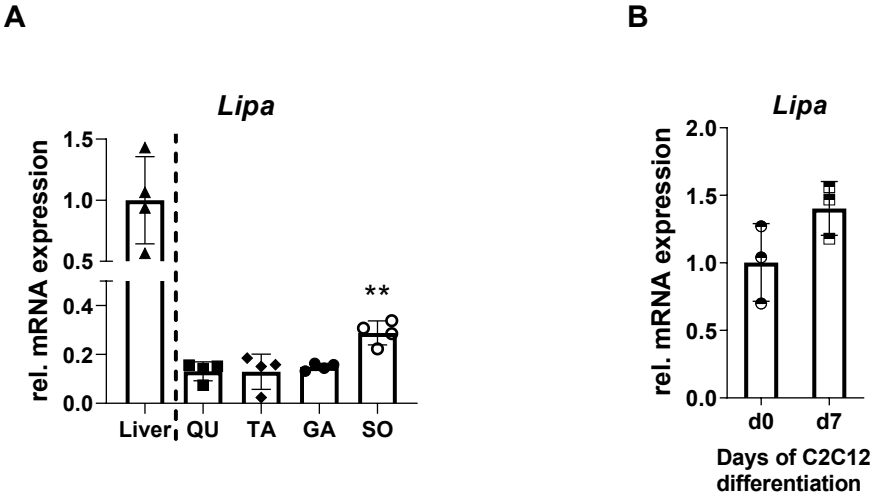

Figure 7: *Lipa* gene expression in different skeletal muscles and C2C12 cells.
Relative expression of *Lipa* (encoding LAL) in **(A)** liver, quadriceps (QU), tibialis anterior (TA), gastrocnemius (GA), and soleus (SO) of fed Wt mice (n=4) (269) and **(B)** C2C12 cells at the beginning (d0) and the end (d7) of differentiation (n=3). Data represent mean ± SD. **p ≤ 0.01. **(A)** One-way ANOVA between skeletal muscles; expression in liver was plotted as reference. **(B)** Unpaired Student's t test. The use of the figure **A** obtained from (269) is allowed under the terms described in the Appendix.

3.2 Phenotypical changes in SM of Lal-/- mice

To investigate phenotypical changes in SM of Lal-/- mice, we examined different hind limb SM, including QU, TA, GA, and SO. Interestingly, we only observed a tendency for SM weight loss in QU from Lal-/- mice at 2 weeks of age (Fig. 8A). However, in older Lal-/- mice (15-16 weeks old), the weight of QU was reduced by 60.6%, TA by 62.1%, and GA by approximately 62.7% (Fig. 8B). Additionally, QU, TA, and GA exhibited reduced weight as a percentage of body weight by 34.8%, 11.2%, and 28.2%, respectively (Fig. 8C). Notably, the weight of SO was reduced only in absolute counts by 48.5%, remaining unchanged when measured as %BW (Fig. 8B, C). H&E staining did not reveal any abnormalities in Lal-/- SM, such as small and angular atrophic fibers, abundant fibrosis, or the presence of central nuclei (Fig. 8D). The multiple nuclei of the fibers were observed at the periphery of the muscle fibers in both genotypes (Fig. 8D). Normal longitudinal sections of SM from Lal-/- were also confirmed by electron microscopy (Fig. 8E).

Furthermore, we quantified the laminin-stained region using ImageJ to determine the CSA and minimum Feret diameter of myofibers, which are essential parameters for assessing the muscular phenotype. QU, TA, and GA mean fiber CSA (Fig. 8F, G) in line with Feret diameter (Fig. 8G, H) were significantly lower in Lal-/- mice compared to their WT littermates. Although the SM of Lal-/- mice were smaller, they also had a paler color compared with their Wt counterparts (Fig. 8I) (269).

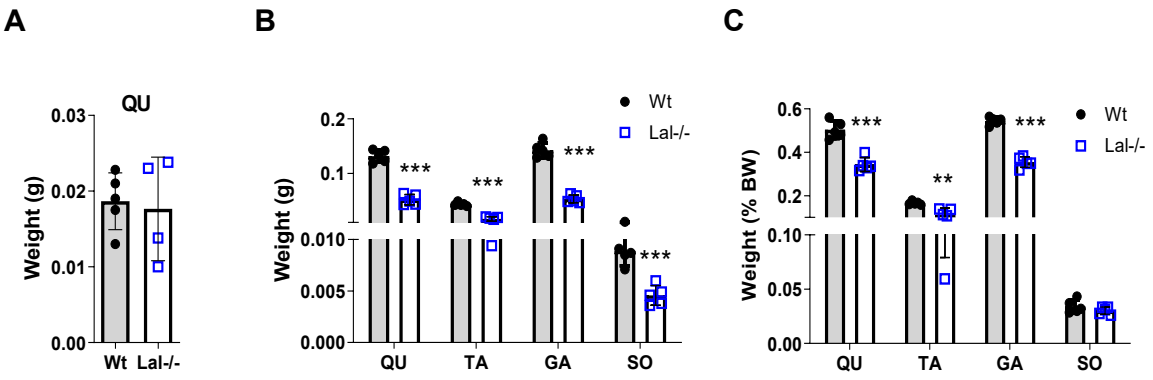

D

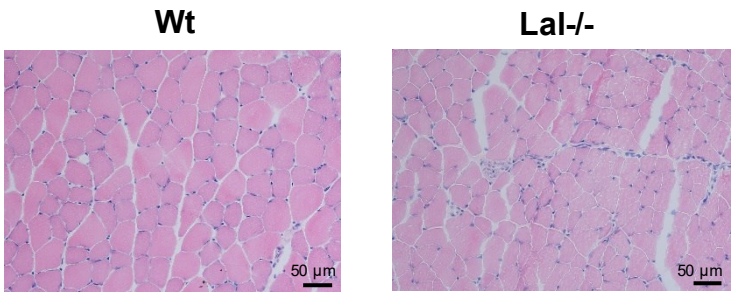
Wt
Lal-/-
50 µm
50 µm

E

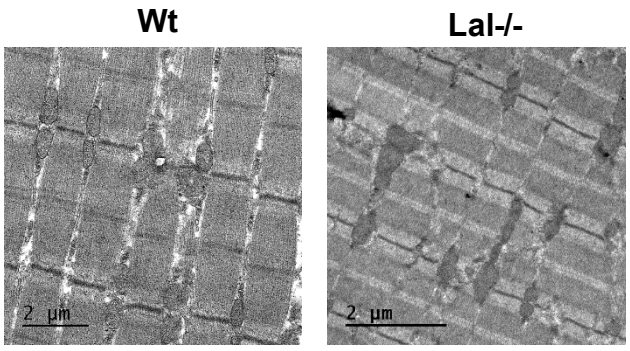
Wt
Lal-/-
2 µm
2 µm

F

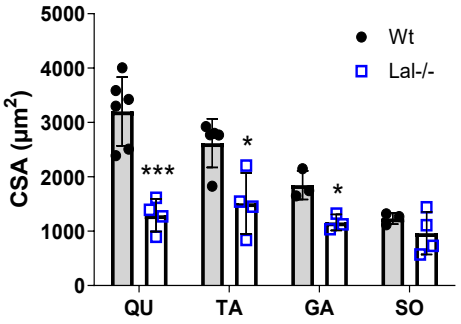
CSA (µm²)
5000
4000
3000
2000
1000
0
Wt
Lal-/-
***
*
*
QU
TA
GA
SO

G

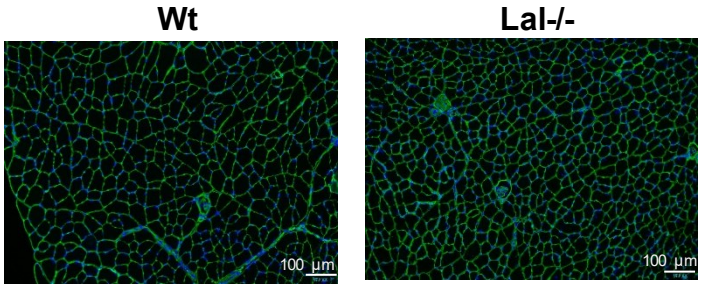
Wt
Lal-/-
100 µm
100 µm

H

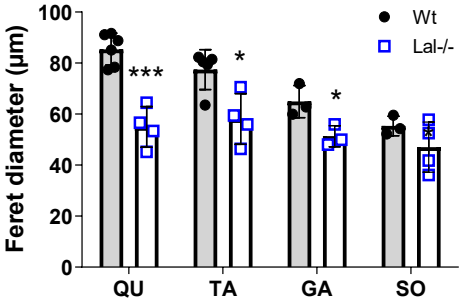
Feret diameter (µm)
100
80
60
40
20
0
Wt
Lal-/-
***
*
*
QU
TA
GA
SO

I

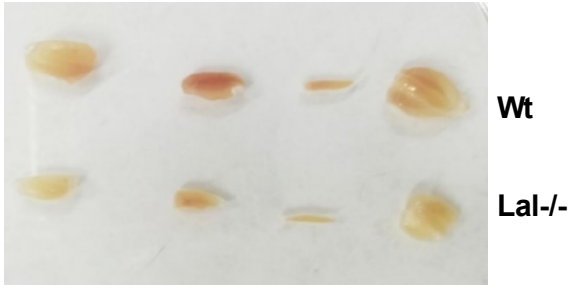
QU
TA
SO
GA
Wt
Lal-/-

Figure 8: Reduced skeletal muscle mass and size in Lal-/- mice.
(A) Absolute weight in g of quadriceps (QU) from 2-week-old Lal-/- and Wt mice (n=4-5). **(B)** Absolute weight and **(C)** weight of the SM in % of body weight (BW) of QU, tibialis anterior (TA), gastrocnemius (GA), and soleus (SO) isolated from male Wt and Lal-/- mice aged 15-16 weeks (fed state). **(D)** Representative images of GA stained with hematoxylin and eosin (scale bar, 50 µm). **(E)** Representative electron micrographs of GA extracted from 50-51 weeks old Lal-/- and Wt mice (scale bar, 2 µm). **(F)** Quantification of laminin-stained cross-sectional area (CSA) (1 to 4 technical replicates from n=3-5 young fed male mice). **(G)** Representative images of laminin-stained TA (scale bar, 100 µm). **(H)** Quantification of minimum Feret diameter of SM fibers (1 to 4 technical replicates from n=3-5 mice). **(I)** Representative images of isolated QU, TA, GA, and SO from Wt and Lal-/- mice. Data represent mean ± SD. *p < 0.05, **p ≤ 0.01, ***p ≤ 0.001. Unpaired Student's t test. The use of the figure **F-I** obtained from (269) is allowed under the terms described in the Appendix.

3.3 Insights into protein turnover mechanisms in Lal-/- mice: implications for muscle mass regulation

Like any other tissue within the body, the regulation of SM mass involves a dynamic process of protein and cellular turnover (285). The ubiquitin-proteasome system is one of the key mechanisms regulating a delicate equilibrium between degradation and synthesis of proteins in SM (286). In the QU (Fig. 9A), TA (Fig. 9B), and GA (Fig. 9C) isolated from Lal-/- mice, we found a noticeable reduction in proteasomal chymotrypsin-like peptidase activity. Interestingly, trypsin-like and caspase-like activities remained comparable between Lal-/- mice and Wt counterparts (Fig. 9A-B), suggesting that the ubiquitin-proteasome system is not activated in Lal-/- SM (269).

In QU, TA, GA, and SO (Fig. 9D-G) from Lal-/- mice and Wt counterparts maintained on RT under starvation conditions, we failed to reveal any differences in the mRNA expression levels of *Murf1* and *Atrogin1*, two key markers associated with muscle atrophy (174, 175). However, in the fed state, the expression of these markers was even reduced in QU, TA, and GA (Fig. 9H-J), but not in the SO muscle (Fig. 9K) from Lal-/- mice. This finding implies that alternative mechanisms may be involved to regulate protein turnover and energy metabolism in Lal-/- muscle tissue (269).

We conducted additional analysis on the expression of FoxO1, a transcription factor implicated in muscle atrophy (146). However, our study indicated a minor increase in FoxO1 gene expression only in GA (Fig. 9L), but no changes in QU, TA, and SO (Fig. 9L) isolated from Lal-/- mice.

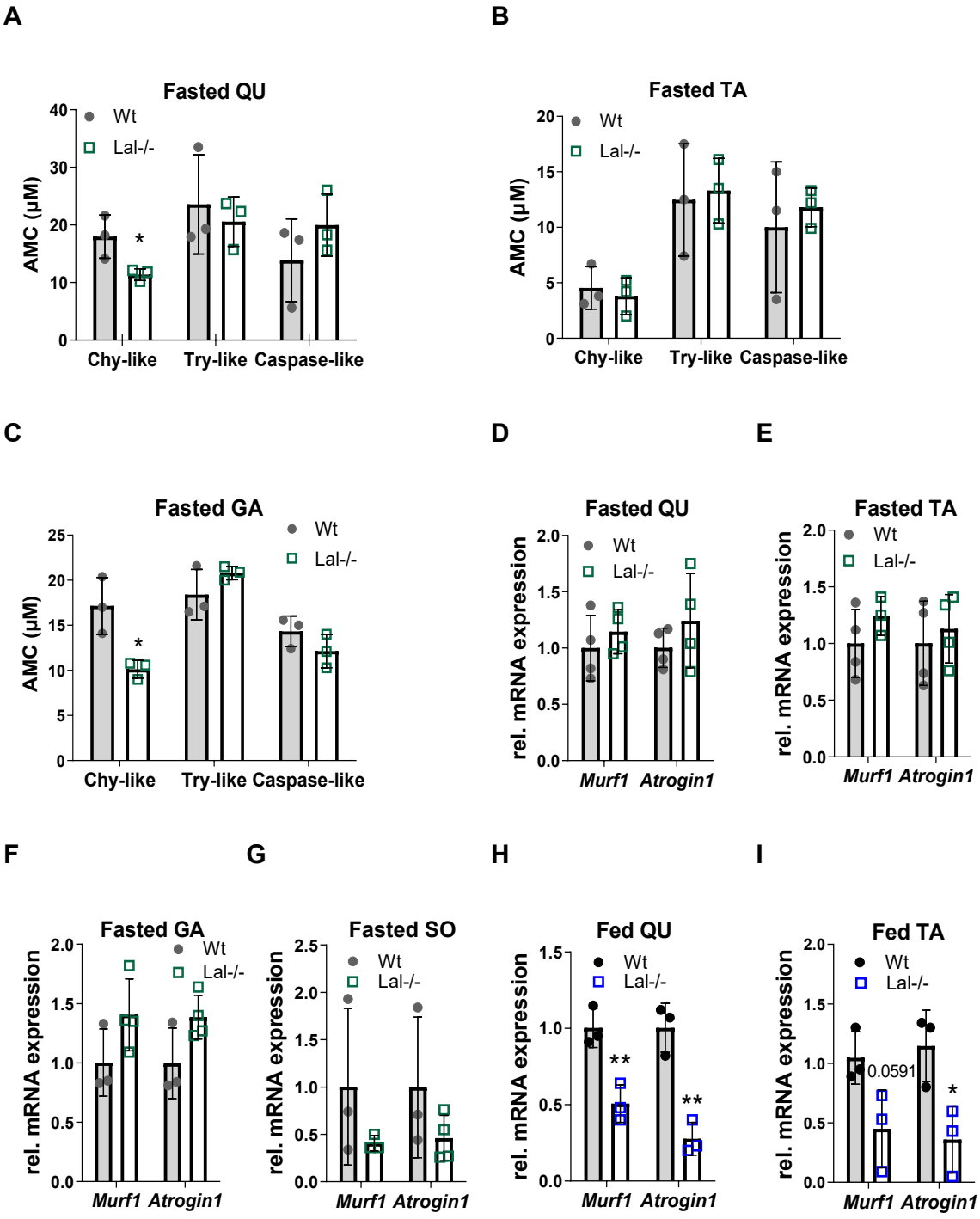
A
Fasted QU
Wt
Lal-/-
AMC (µM)
40
30
20
10
0
*
Chy-like
Try-like
Caspase-like
B
Fasted TA
Wt
Lal-/-
AMC (µM)
20
15
10
5
0
Chy-like
Try-like
Caspase-like
C
Fasted GA
Wt
Lal-/-
AMC (µM)
25
20
15
10
5
0
*
Chy-like
Try-like
Caspase-like
D
Fasted QU
Wt
Lal-/-
rel. mRNA expression
2.0
1.5
1.0
0.5
0.0
Murf1
Atrogin1
E
Fasted TA
Wt
Lal-/-
rel. mRNA expression
2.0
1.5
1.0
0.5
0.0
Murf1
Atrogin1
F
Fasted GA
Wt
Lal-/-
rel. mRNA expression
2.0
1.5
1.0
0.5
0.0
Murf1
Atrogin1
G
Fasted SO
Wt
Lal-/-
rel. mRNA expression
2.5
2.0
1.5
1.0
0.5
0.0
Murf1
Atrogin1
H
Fed QU
Wt
Lal-/-
rel. mRNA expression
1.5
1.0
0.5
0.0
**
**
Murf1
Atrogin1
I
Fed TA
Wt
Lal-/-
rel. mRNA expression
2.0
1.5
1.0
0.5
0.0
0.0591
*
Murf1
Atrogin1

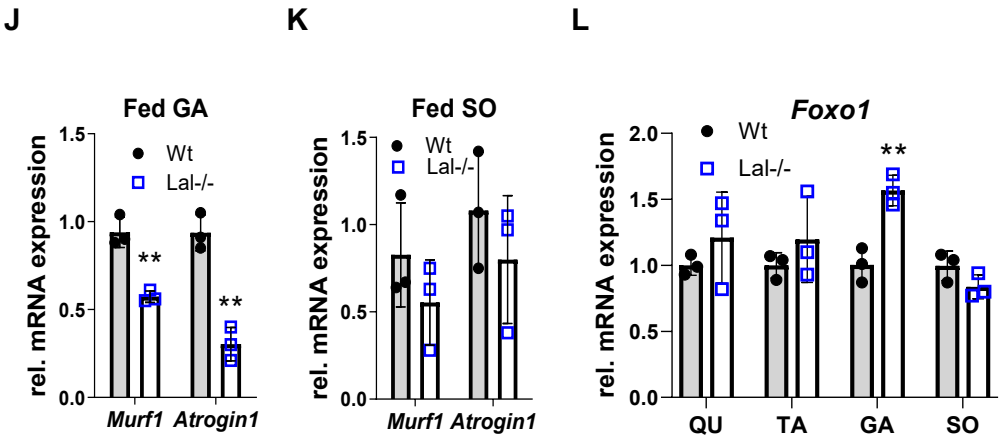

Figure 9: The reduction in muscle size observed in Lal-/- mice does not appear to be related to skeletal muscle (SM) proteolysis.
Proteasomal peptidase activities (chymotrypsin-like (Chy-like), trypsin-like (Try-like), and caspase-like) estimated in **(A)** QU, **(B)** TA, and **(C)** GA dissected from young female 12-h fasted Lal-/- and control mice (n=3). Activities were calculated based on the fluorescence of 7-amino-4-methylcoumarin (AMC) as standard. Relative mRNA expression of genes encoding the SM proteolysis markers *Murf1* and *Atrogin1* in SM of **(D-G)** 19-21-week-old female mice fasted for 12 h (n=4) and **(H-K)** 15-16-week-old male mice (fed state) (n=3). **(L)** Relative mRNA expression of *Foxo1* in SM of 15-16-week-old male mice (fed state) (n=3). Data represent mean ± SD. *p < 0.05, **p ≤ 0.01. Unpaired Student's t test. The use of the figures **A - K** obtained from (269) is allowed under the terms described in the Appendix.

The IGF-1/Akt/mTOR pathway plays a critical role as an intracellular regulator of muscle mass (287-289). We failed to reveal any differences in the gene expression of *Igf1* in SM between the genotypes as depicted in Figure 10A. Although we observed a small increase in *Igf1r* mRNA levels (Fig.10B) in QU and SO isolated from fed Lal-/- mice. Further, we estimated protein expression of Akt, the mTOR target 4E-BP1 and their phosphorylated forms. We were not able to detect any significant changes in the ratio of pAkt/Akt (Fig. 10C, D) and p4E-BP1/4E-BP1 (Fig. 10E, F) protein expression in Lal-/- QU (Fig. 10C, E) and GA (Fig. 10D, F). Thus, IGF-1/Akt/mTOR pathway was not affected in Lal-/- SM, and the observed alterations in SM mass and size were not due to changes in this pathway (269).

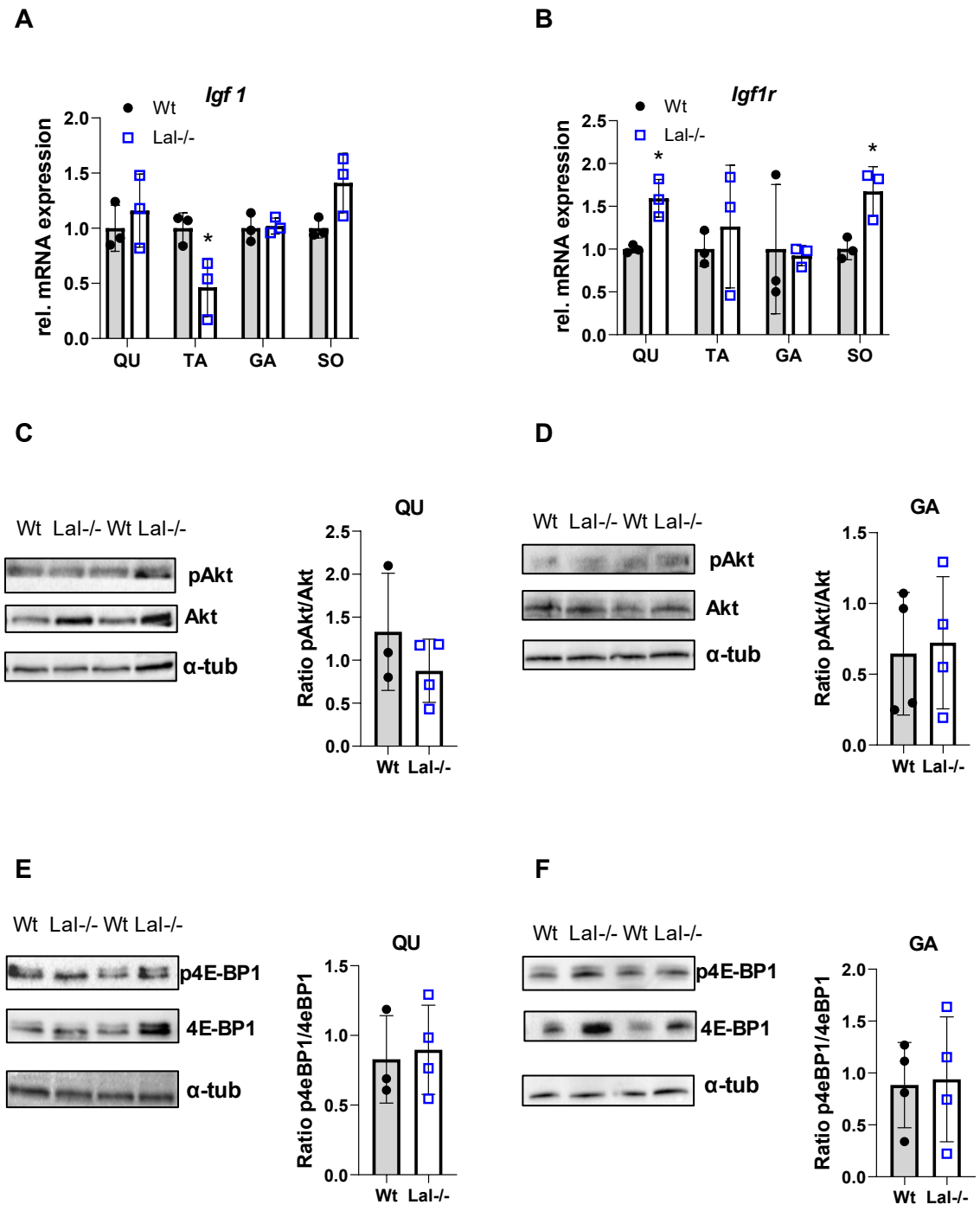

Figure 10: IGF-1/Akt/mTOR pathway was not significantly altered in Lal-/- skeletal muscles.

(A) Relative *Igf1* mRNA expression in quadriceps (QU), tibialis anterior (TA), gastrocnemius (GA), and soleus (SO) of young fed male Lal-/- mice and Wt counterparts (n=3) relative to *cyclophilin A* expression as reference gene. Protein expression and quantification of **(C, D)** pAkt/Akt and **(E, F)** p4E-BP1/4E-BP1 ratios (n=4) in **(C, E)** QU and **(D, F)** GA lysates of Lal-/- and Wt mice with α-tubuline (α-tub) as loading control. Data represent mean ± SD. *p < 0.05. Unpaired Student's t test. The use of the figure **A, C - F** obtained from (269) is allowed under the terms described in the Appendix.

In SM, AMPK activation leads to various metabolic changes aimed at increasing energy production and conserving energy expenditure. AMPK phosphorylation has been associated with the inhibition of the mTOR pathway, which is a key regulator of muscle protein synthesis (290). To determine whether protein synthesis is reduced in SM of Lal-/- mice due to possible changes in AMPK expression, we assessed its phosphorylated form in both the fed and fasted states. Densitometric evaluation revealed no significant changes in the pAMPKβ1/AMPKβ1 ratio (Figure 11A). However, we detected decreased AMPKβ1 expression in Lal-/- mice, as estimated as the ratio of AMPKβ1 intensity to the loading control (calnexin) (Fig. 11A).

Dividing the GA into a "red" (enriched in oxidative slow fibers) and "white" (enriched in glycolytic fast fibers) part allows a more detailed study of metabolic and functional differences between fiber types within one particular SM. Western blot analysis revealed stronger AMPKβ expression in the GA segment enriched with oxidative fibers (Fig. 11B). The AMPKβ2 subunit was almost undetectable and expression of the AMPKβ1 subunit was reduced in Lal-/- mice (Fig. 11B). In addition, the expression signal of both subunits of pAMPKβ was very weak (Fig. 11B). However, despite the decreased expression of AMKP protein, we cannot draw a conclusion about role of AMPK signaling in the SM of Lal-/- mice.

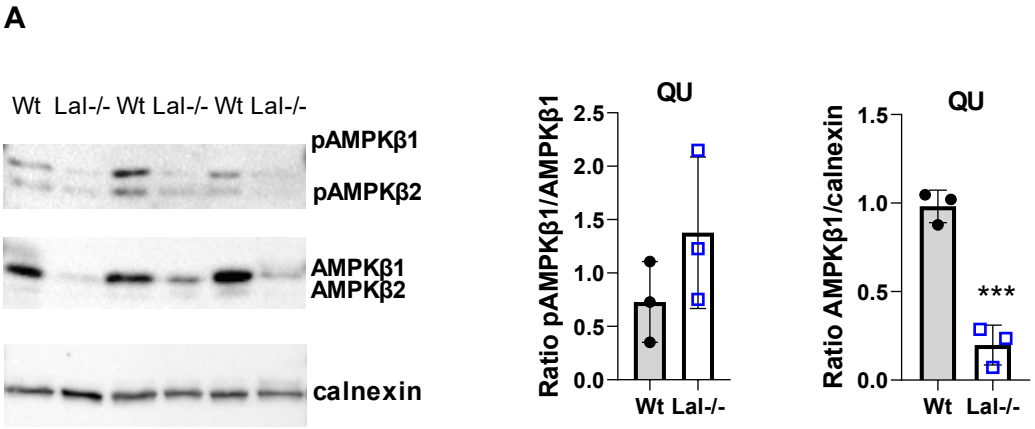

B

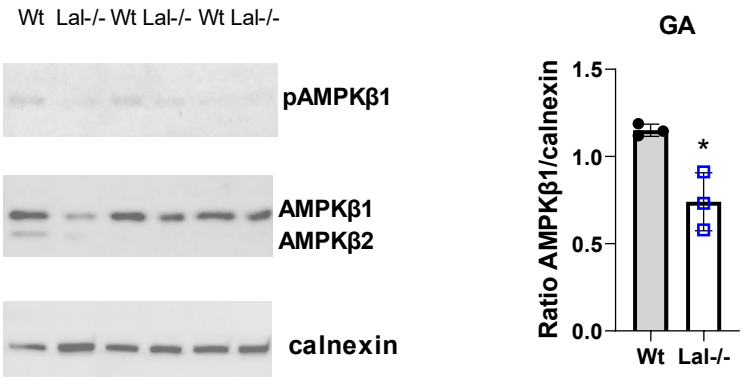

Figure 11: The reduced expression of the AMPK subunit in Lal-/- skeletal muscle with its unchanged phosphorylation.
The protein expression levels of pAMPKβ1/2 and AMPKβ1/2 were determined by Western blot analysis in **(A)** quadriceps (QU) lysates from young 6-h fasted and **(B)** gastrocnemius (GA) from fed Wt and Lal-/- mice (n=3). Calnexin was used as a loading control. Data represent mean ± SD. *p < 0.05, ***p ≤ 0.001. Unpaired Student's t test.

We additionally performed LC3 Western blot to evaluate the levels of autophagic flux in SM, providing insight into the potential role of LAL loss in modulating autophagy. Unexpectedly, ratio LC3B-II to LC3B-I was upregulated in GA from Lal-/- mice (Fig. 12) suggesting enhanced autophagosome formation and thus increased autophagic activity.

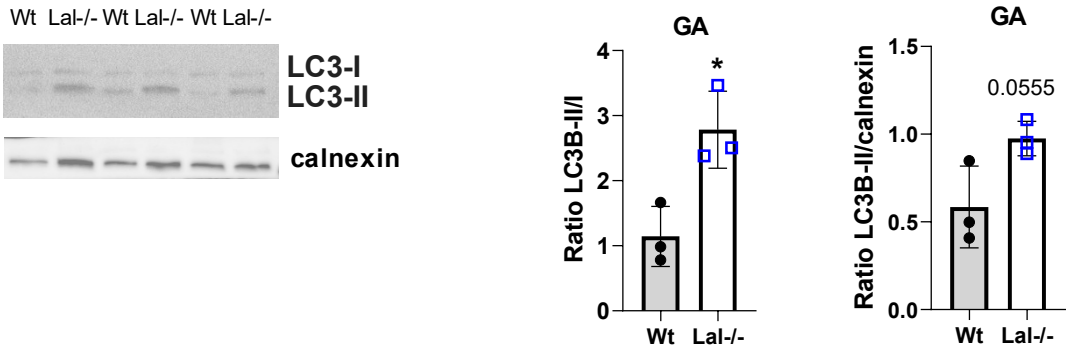

Figure 12: Increased expression of LC3B-II in gastrocnemius (GA) from old fed Lal-/- mice.
The protein expression levels of LC3B-I and II were determined by Western blot analysis. Calnexin was used as a loading control. Data represent mean ± SD. *p < 0.05. Unpaired Student's t test.

3.4 Loss of LAL leads to alterations in the concentrations of AA in SM and plasma

Reduced AA availability in the SM can have significant implications for muscle protein synthesis and anabolism (291). By analyzing NMR spectra, metabolites that were quantified as normalized peak revealed altered AA in both oxidative and glycolytic segments of GA from Lal-/- mice (Fig. 13A-C). Glucogenic AA such as alanine (Ala), glycine (Gly), and glutamine (Gln) (Fig.13A), as well as the glucogenic/ketogenic AA tyrosine (Tyr) (Fig.13B) were reduced in both GA segments studied.

Further analysis of plasma AA by HPLC revealed decreased abundance of Gln in *ab libitum* fed Lal-/- mice (Fig. 13D). Concentrations of BCAA such as valine (Val) (Fig. 13D), isoleucine (Ile) (Fig. 13E), and leucine (Leu) (Fig. 13F) were increased in plasma but unchanged in GA (Fig. 13A-C) (269). These minor changes in AA concentration are likely not related to SM fiber degradation.

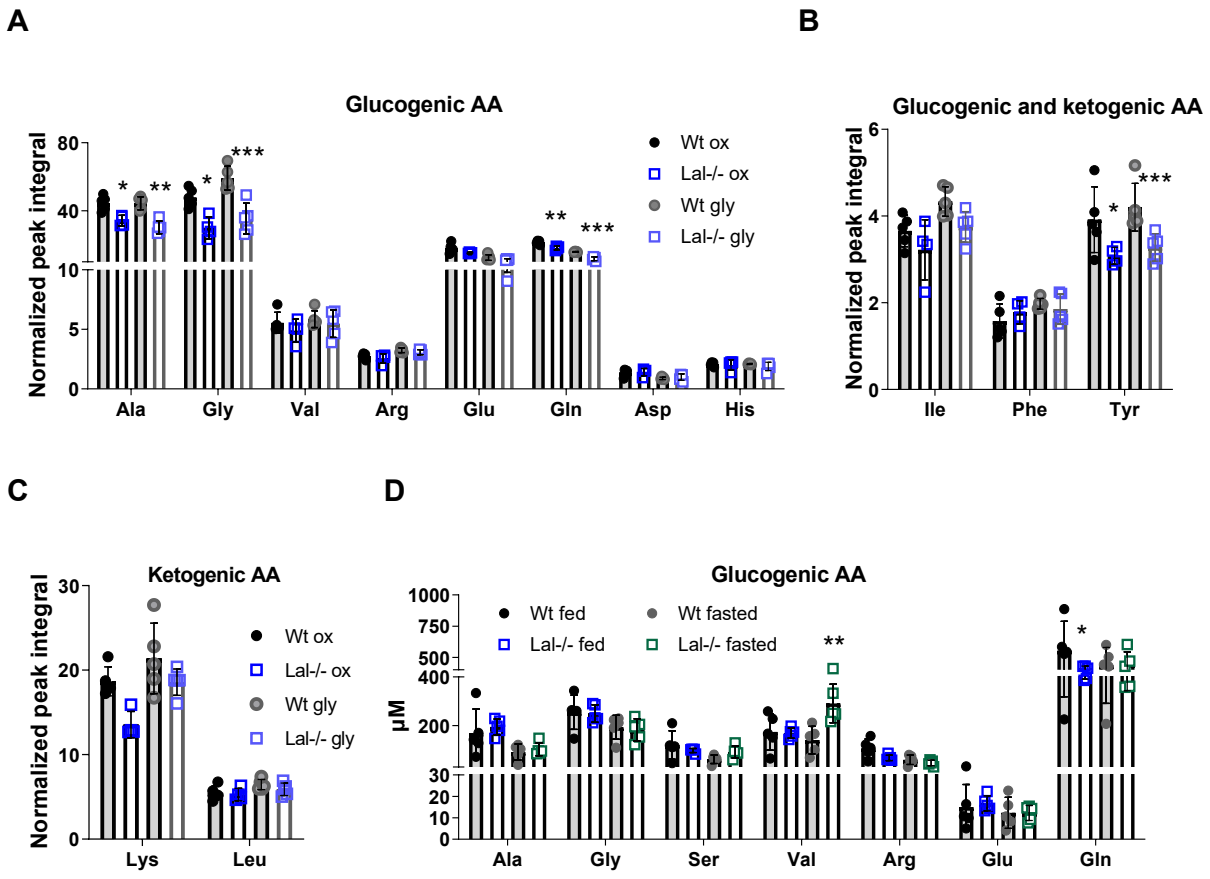

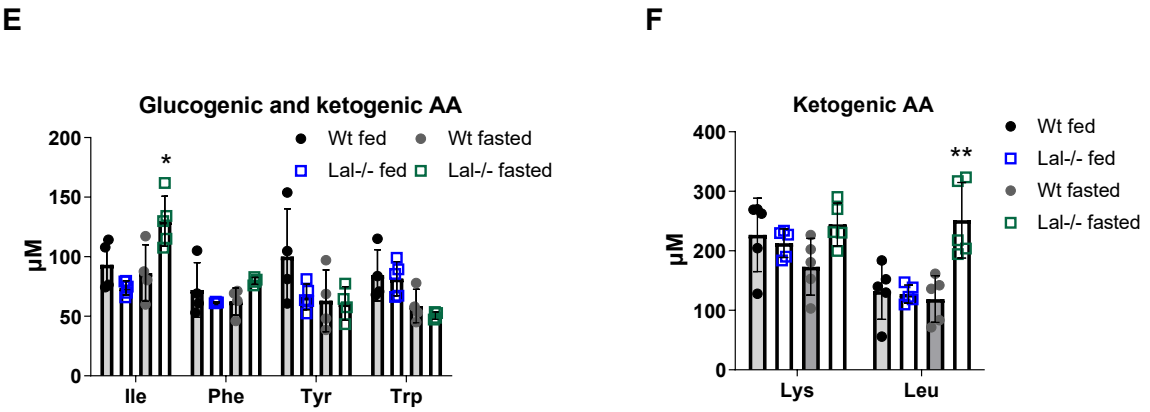

Figure 13: Altered amino acid (AA) concentrations in gastrocnemius (GA) and plasma of Lal-/- mice.
Individual **(A)** glucogenic, **(B)** glucogenic/ketogenic, and **(C)** ketogenic AA of 14-17-week-old male WT and Lal-/- mice (fed state) quantified by NMR. The data are presented as normalized peak integral enriched in oxidative (ox) or glycolytic (gly) segments of GA from Lal-/- mice (n=4-5). Plasma AA concentrations quantified using AA separation of female 40-50-week-old Lal-/- and Wt mice in the fed and 12-h fasted states (n=4-5). Data represent mean ± SD. *p < 0.05, **p ≤ 0.01, ***p ≤ 0.001. Unpaired Student's t test for the comparison of Wt and Lal-/- samples within either ox or gly GA segments or between fed and fasted conditions. The use of the figure **D - F** obtained from (269) is allowed under the terms described in the Appendix.

3.5 Impaired content of energetic substrates in Lal-/- SM

Intramuscular ATP stores are known to be relatively low and they are further reduced in Lal-/- mice QU (Fig. 14A). This may result from various factors, including lack of energy substrates, insufficient oxygen supply, or impaired metabolic pathways (292). Following previous findings of decreased blood glucose and heightened glucose absorption in GA (263) we confirmed an increased [^{3}H]2-deoxy-D-glucose uptake across all types of SM examined (Fig. 14B) (269).
To further identify metabolic differences between control and Lal-/- SM, we performed NMR metabolic profiling for more oxidative or more glycolytic segments of GA from Lal-/- mice. Loss of LAL dramatically affected overall metabolism of SM of mice: 25 out of 38 metabolites investigated were significantly altered. Intramuscular glucose levels were increased in both oxidative and glycolytic parts of GA from Lal-/- mice (Fig. 14C), however, previous results indicated unchanged expression of glycolysis-related genes (263) and lactate concentrations in SM of chow-fed Lal-/- mice (Fig. 14D (269) and (263)). Interestingly, the glycogen concentration was slightly increased in both studied parts of GA (Fig. 14E), whereas creatine was only increased in more oxidative fibers (Fig. 14F) (269). Next, we estimated the content of some metabolites from the TCA cycle. Succinate was slightly reduced in oxidative fibers (Fig. 14G); but fumarate concentrations were similar between the genotypes examined in both

red and white GA segments (Fig.14H). Among the most reduced metabolites in oxidative and glycolytic GA parts, we noted choline (Fig. 14I) and carnosine (Fig. 14J), which both play a critical role in SM functions. These findings suggest metabolic differences between Lal-/- and control mice SM, including increased glucose uptake and levels of intramuscular energy metabolites.

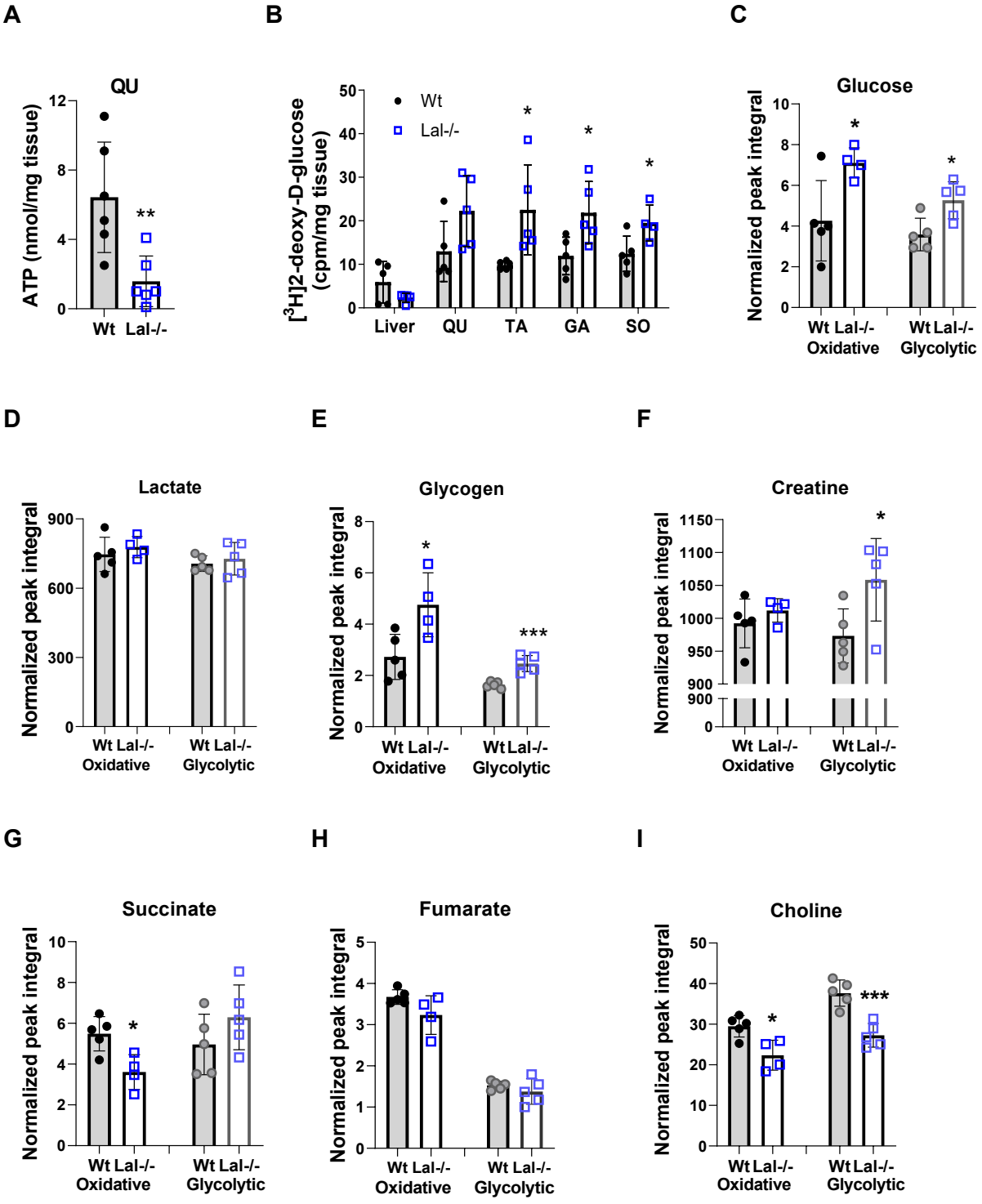

J

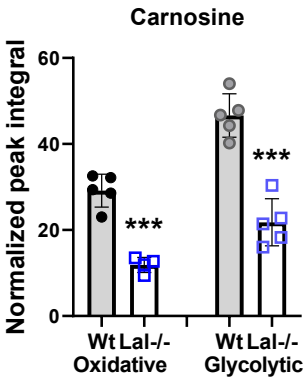

Figure 14: Metabolic alterations in skeletal muscle of Lal-/- mice: intramuscular ATP, glucose uptake, and metabolite profiling.
(A) Measurement of ATP levels in the quadriceps (QU) of fed young male mice (n= 6-7) by mass spectrometry. **(B)** Assessment of radioactivity (cpm) in liver, QU, tibialis anterior (TA), gastrocnemius (GA), and soleus (SO) in female Wt and Lal-/- mice following intraperitoneal injection of [^{3}H]2-deoxy-D-glucose (n=5). **(C-J)** Quantification of metabolites expressed as standardized peak intensities in GA separated for glycolytic and oxidative parts from male 15-16-week-old *ab libitum* fed mice by NMR (n=4-5). Data represent mean ± SD. *p < 0.05, **p ≤ 0.01, ***p ≤ 0.001. Unpaired Student's t test. The use of the figure **A, B, E, F** obtained from (269) is allowed under the terms described in the Appendix.

3.6 Loss of LAL results in minor changes in SM lipid metabolism in Lal-/- mice in the fed state

Most cells and organs, such as the liver, spleen, and small intestine from Lal-/- mice, are characterized by lipid-laden lysosomes (256, 258, 259). However, our investigation revealed intriguing variations in lipid composition across different SM of these mice. Specifically, when Lal-/- mice were fed *ad libitum*, we noted a significant increase in concentrations of CE exclusively in the GA (Fig. 15C). Conversely, in SO, while there was a trend towards increased CE levels, we observed elevated concentrations of FC (Fig. 15D). Interestingly, when examining lipids including cholesterol and TG across other SM such as QU and TA, we found comparable levels among all tested SM (Fig. 15A-D) (269). Additionally, staining experiments with ORO, a dye commonly used to visualize lipid accumulation, failed to reveal any visible lipid accumulation in the SM of Lal-/- mice (Fig. 15E). This observation suggested that despite alterations in lipid metabolism and accumulation in other tissues, the SM of Lal-/- mice may exhibit a unique lipid-handling phenotype or have mechanisms to prevent lipid deposition within muscle fibers.

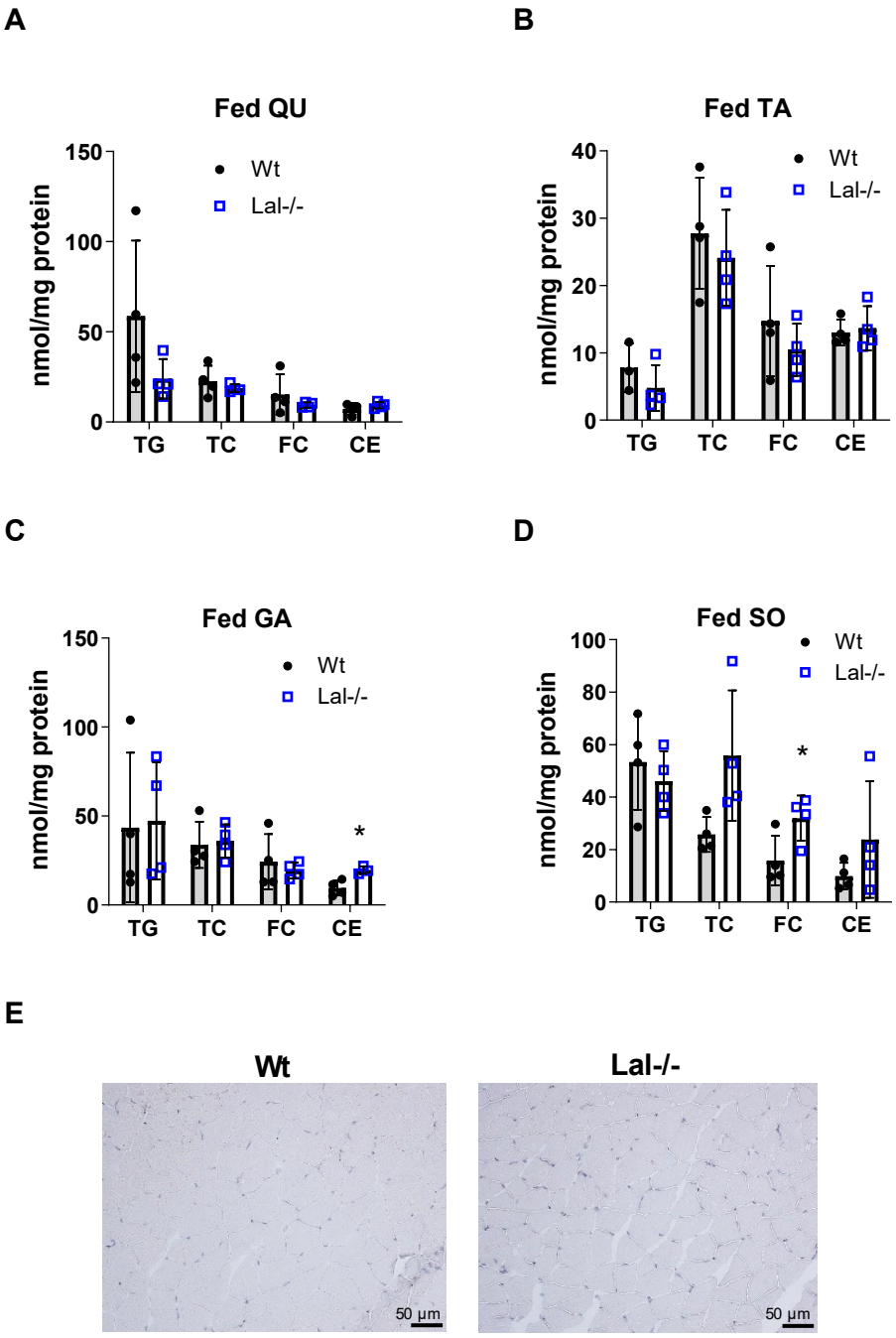

Figure 15: Minor alterations in lipid metabolism in skeletal muscles of male Lal-/- mice in *ad libitum* fed state.

(A-D) Biochemical quantification of triacylglycerol (TG), total cholesterol (TC), free cholesterol (FC), and cholesteryl ester (CE) concentrations from in **(A)** quadriceps (QU), **(B)** tibialis anterior (TA), **(C)** gastrocnemius (GA), and **(D)** soleus (SO) (n=3-4). **(E)** Representative images of oil red O- stained GA (scale bar, 50 µm). Data represent mean ± SD. *p < 0.05. Unpaired Student's t test. The use of the figure **A - D** obtained from (269) is allowed under the terms described in the Appendix.

3.7 Loss of LAL severely affects lipid metabolism in fasted Lal-/- mice

During fasting, lipid oxidation may play an important role in meeting the energy needs of SM (89). Moreover, it is well-described that the phenotype of Lal-/- mice deteriorates with age (222, 259). In the fasted state, Lal-/- mice aged 40-55 weeks exhibited a significant reduction in TG concentrations in QU, as depicted in Figure 16A. Additionally, there were trends toward decreased TG concentrations observed in TA, GA, and SO (Fig. 16B-D). Furthermore, we observed elevated concentrations of CE in QU, TA, and GA of mature Lal-/- mice compared to their corresponding littermates This increase in CE levels appeared to correlate with the elevated TC concentrations (Fig. 16A-C). In the SO muscle from Lal-/- mice, we observed increased levels of TC and FC, but no change in CE content (Fig. 15D).

Since Lal-/- mice suffer from loss of WAT (256) and have reduced circulating TG levels in the fasted state (263), we next analyzed whether FAO might be affected in Lal-/- SM. mRNA levels of genes involved in FA flux in SM were comparable (Fig. 16E-H), except for slightly increased expression of *Fabp3* and *Acsl1* in QU (Fig. 16E) and *Cpt1b* in GA (Fig. 16G). Although changes were detected, they were too small to be considered biologically significant in the context of the study. Hence, these changes are not regarded as relevant for the biological processes or outcomes being investigated. We failed to detect differences in individual acyl-carnitines (CAR) in GA (Fig. 16K). However, CAR species in QU (Fig.16I), TA (Fig.16J), and SO (Fig.16L), as well as total CAR concentrations (Fig. 16M) were markedly reduced in Lal deficient mice. These observations, as well as the decrease in FAO in GA (Figure 16N), confirm the decreased ability to utilize lipids as substrates in the SM of starved Lal-/- mice (269).

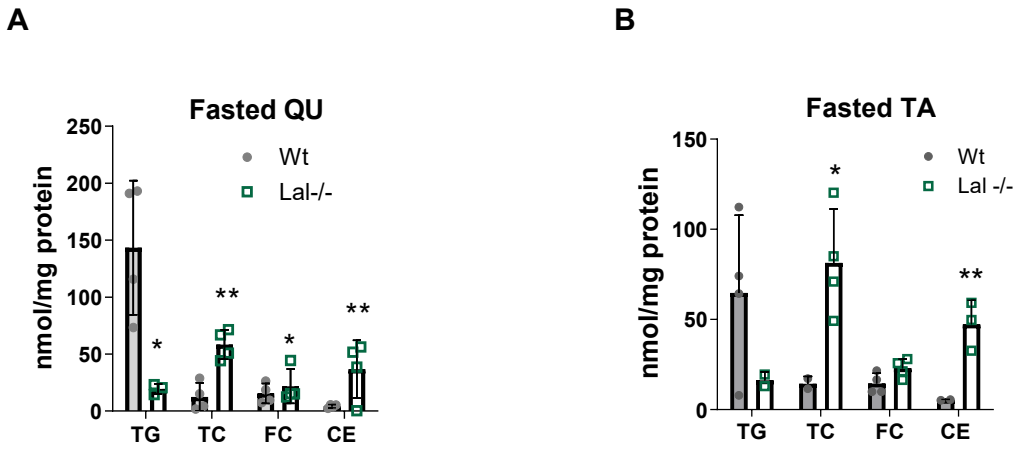

C

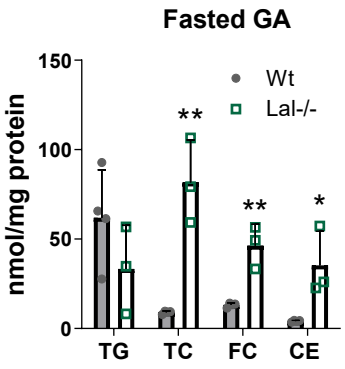
Fasted GA
nmol/mg protein
150
100
50
0
Wt
Lal-/-
**
**
*
TG
TC
FC
CE

D

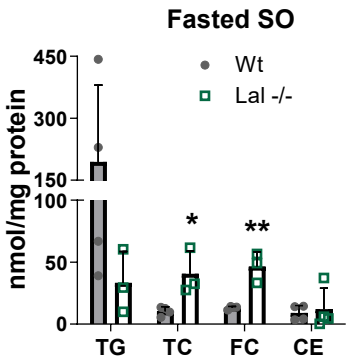
Fasted SO
nmol/mg protein
450
300
150
100
50
0
Wt
Lal -/-
*
**
TG
TC
FC
CE

E

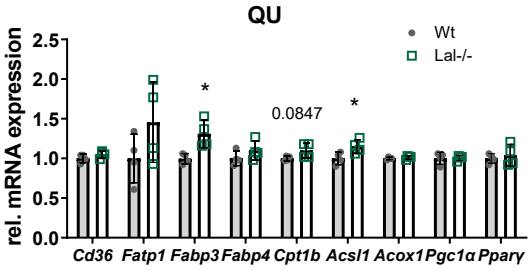
QU
rel. mRNA expression
2.5
2.0
1.5
1.0
0.5
0.0
Wt
Lal-/-
*
0.0847
*
Cd36 Fatp1 Fabp3 Fabp4 Cpt1b Acsl1 Acox1 Pgc1α Pparγ

F

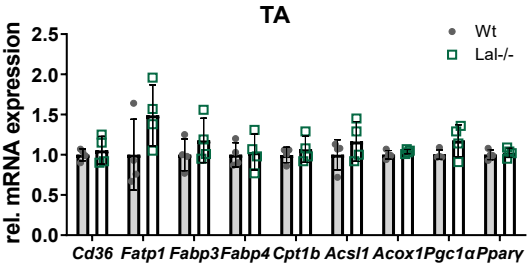
TA
rel. mRNA expression
2.5
2.0
1.5
1.0
0.5
0.0
Wt
Lal-/-
Cd36 Fatp1 Fabp3 Fabp4 Cpt1b Acsl1 Acox1 Pgc1α Pparγ

G

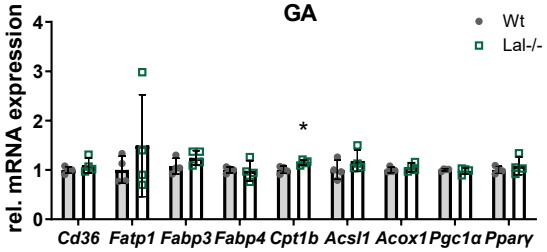
GA
rel. mRNA expression
4
3
2
1
0
Wt
Lal-/-
*
Cd36 Fatp1 Fabp3 Fabp4 Cpt1b Acsl1 Acox1 Pgc1α Pparγ

H

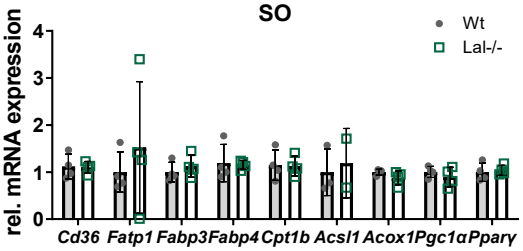
SO
rel. mRNA expression
4
3
2
1
0
Wt
Lal-/-
Cd36 Fatp1 Fabp3 Fabp4 Cpt1b Acsl1 Acox1 Pgc1α Pparγ

I

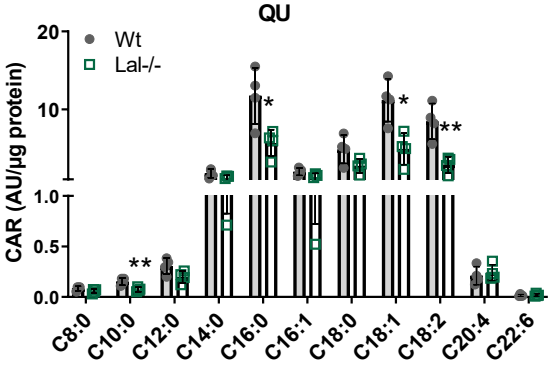
QU
CAR (AU/µg protein)
20
10
1.0
0.5
0.0
Wt
Lal-/-
**
*
*
**
C8:0
C10:0
C12:0
C14:0
C16:0
C16:1
C18:0
C18:1
C18:2
C20:4
C22:6

J

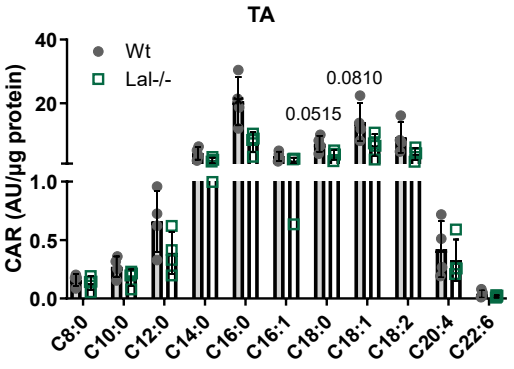
TA
CAR (AU/µg protein)
40
20
1.0
0.5
0.0
Wt
Lal-/-
0.0515
0.0810
C8:0
C10:0
C12:0
C14:0
C16:0
C16:1
C18:0
C18:1
C18:2
C20:4
C22:6

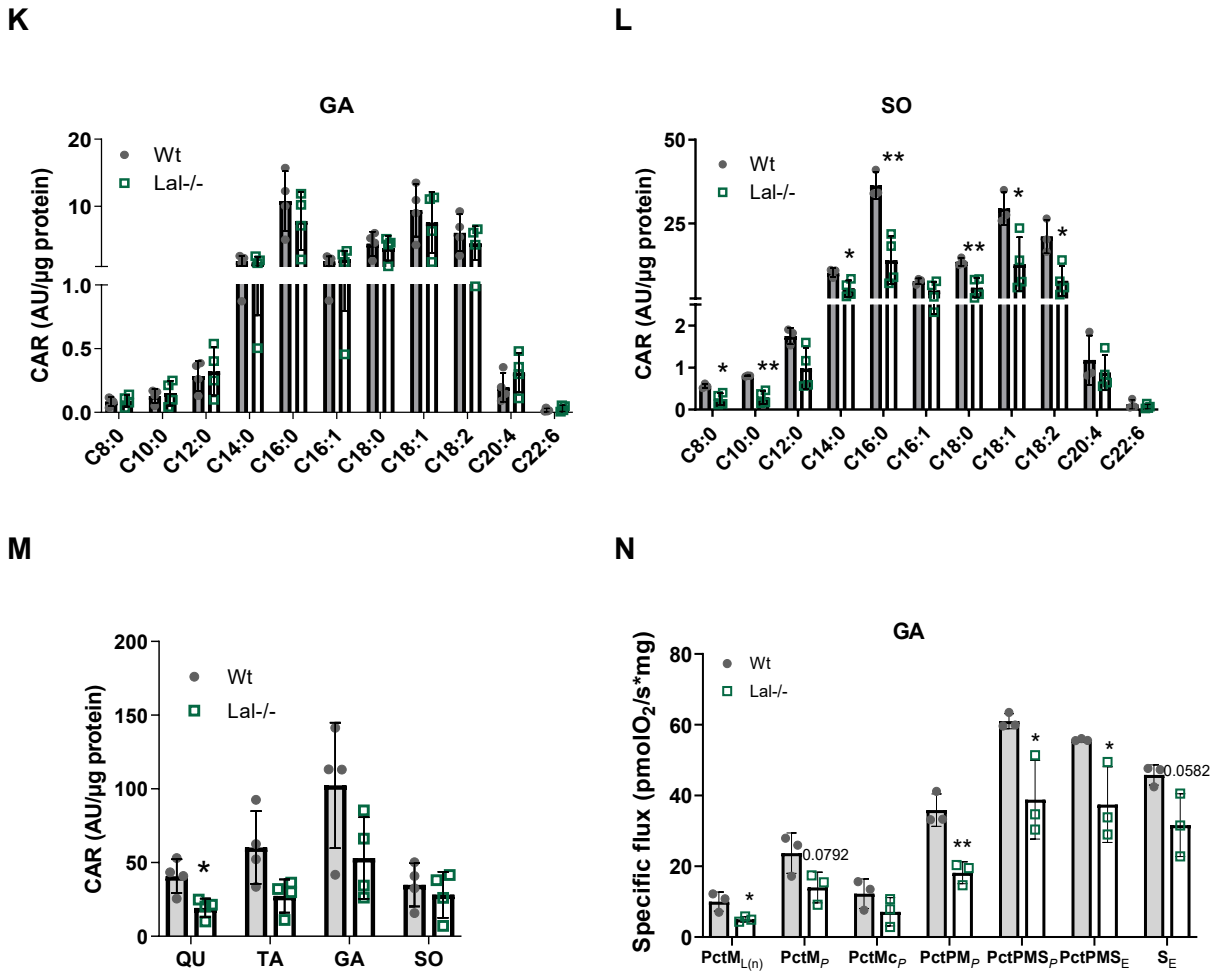

Figure 16: Altered lipid composition and fatty acid oxidation (FAO) in SM of fasted mature Lal-/- mice.

Biochemical analyses of the lipid content in **(A)** QU, **(B)** TA, **(C)** GA, and **(D)** SO from male 40-55-week-old mice in a 12-h fasted state (n=3-4). Relative mRNA expression of genes involved in FAO in **(E)** QU, **(F)** TA, **(G)** GA, and **(H)** SO of 12-h fasted young female Wt and Lal-/- mice (n=3-4). Individual acyl-carnitine (CAR) concentrations in **(I)** QU, **(J)** TA, **(K)** GA, and **(L)** SO of Wt and Lal-/- mice (n=4). **(M)** Total CAR levels in various SM of Lal-/- and Wt mice (n=4). **(N)** FAO was estimated as specific flux at distinct mitochondrial stages in permeabilized fibers from GA of juvenile male Lal-/- and Wt mice. Initial FAO-pathway activity (F) was induced with palmitoyl carnitine (Pct) in combination with malate (M): indicated by $PctM_{L(n)}$, with Pct and L(n) depicting the LEAK state which measures mitochondrial respiration without ATP production. The capacity for oxidative phosphorylation was denoted by $PctM_P$ following the introduction of saturating levels of ADP (*P*). Evaluations of the external mitochondrial membrane integrity were performed with the addition of cytochrome C (c), labeled as $PctMc_P$. The respiratory response to combined activation of the FAO and NADH pathways was measured in the presence of pyruvate (P), captured as $PctPM_P$, reflecting convergent electron influx. The synchronized respiratory boost from FAO, NADH pathways, and complex II activities was recorded as $PctPMS_P$ upon introducing succinate (S). The peak electron transfer capacity was explored via uncoupler titration, labeled as $PctPMS_E$ (E stands for electron transfer capacity). Finally, the residual electron transfer activity, independent of phosphorylation, was stated as SE (sample size n=3 for each group). **(A, E-N)** Data represent mean ± SD. **(B-D)** Data represent mean +SD. *p ≤0.05, **p ≤ 0.01. Unpaired Student's t test.

The use of this figure obtained from (265) is allowed under the terms described in the Appendix.

3.8 HFHC diet did not lead to any significant changes in the lipid composition of Lal-/- SM

Lal-/- mice, compared to their Wt littermates, exhibited lower body weight and progressive loss of WAT when fed chow (256, 263). Although they consumed more food than their WT littermates, they showed no weight gain when fed a western type diet (WTD) for a maximum of 6 weeks (260). Moreover, previous observations confirmed that WTD feeding resulted in weight gain in the liver and proximal intestine, a phenomenon consistent with observations in chow diet-fed Lal-/- mice (260). To see whether a lipid-enriched diet may also affect SM mass, we challenged mice with a high-fat, high-cholesterol (HFHC) diet for 6 weeks. Like WTD-fed mice, Lal-/- mice fed the HFHC diet gained weight and their mass increase remained comparable to Wt littermates (Fig. 17A). The weight of QU, TA, GA, and SO in grams was still drastically reduced in Lal-/- compared to WT mice by 54.2%, 50.4%, 50.1%, and 32.4% respectively (Fig. 17B). These observations are consistent with the difference in SM mass in mice fed chow diet.

The quantification of lipids did not reveal a consistent pattern in the SM studied. In particular, the CE concentrations were higher in QU and TA from Lal-/- mice fed HFHC diet (Fig. 17C, D). TC was elevated in TA, GA, and SO (Fig. 17D-F), but not in QU (Fig. 17C), while FC concentrations were increased in GA and SO (Fig. 17E, F). Notably, a significant difference in TG concentration was observed only in GA (Fig. 17E), where Lal-/- mice had lower TG content compared with the corresponding controls (Fig. 17C, D, F).

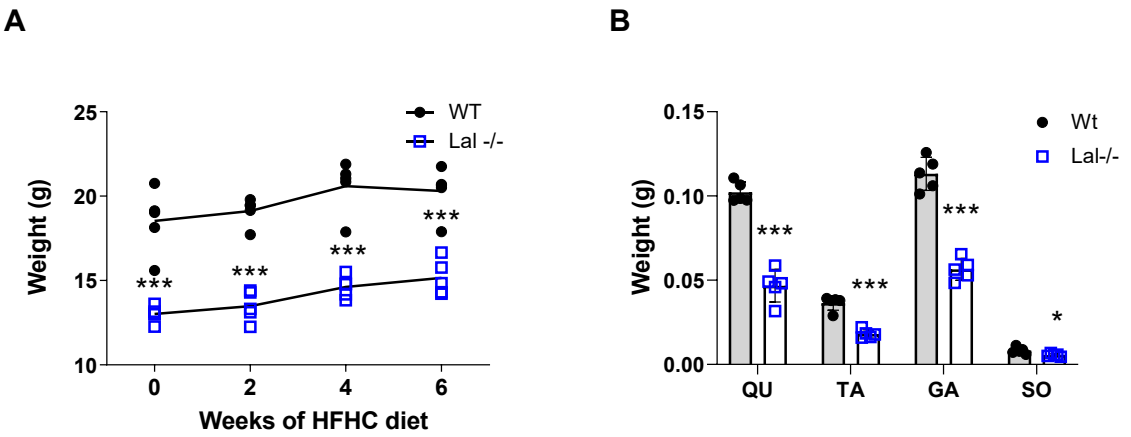

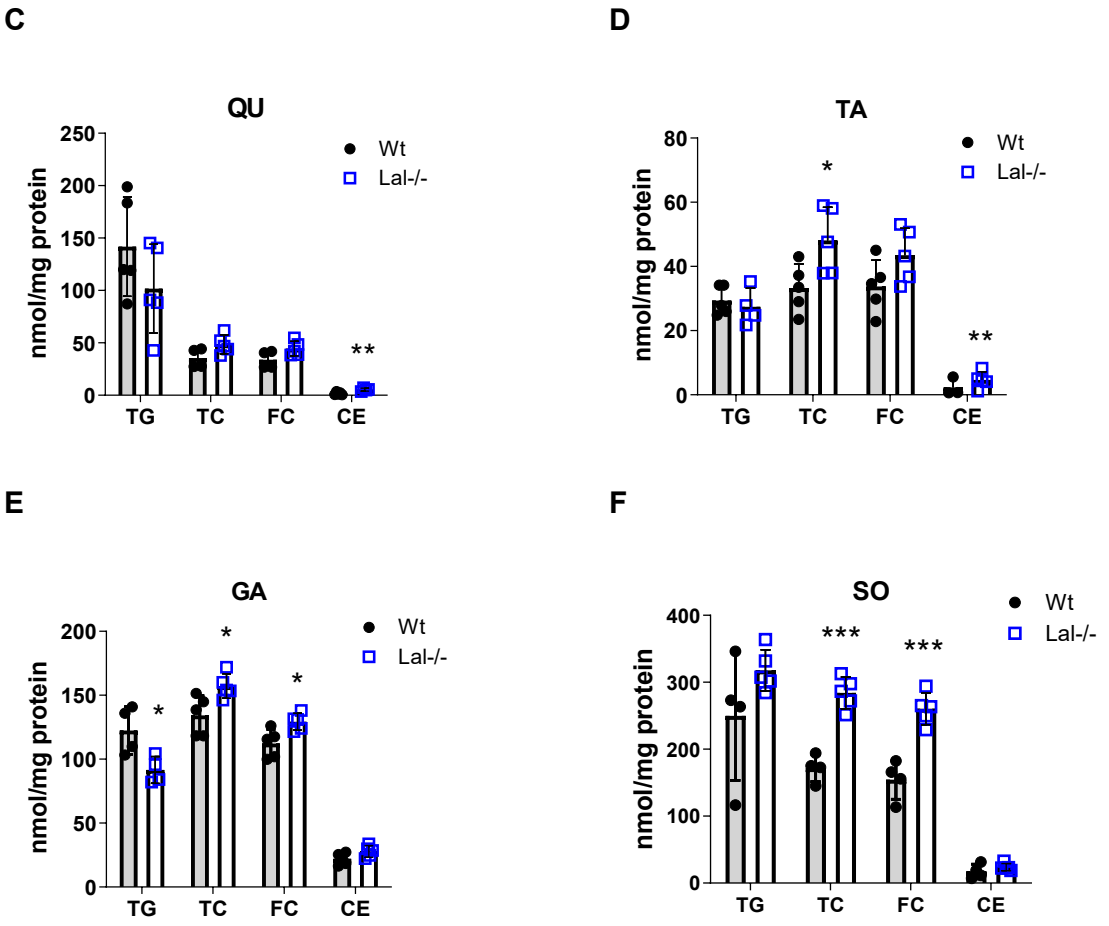

Figure 17: Unchanged skeletal muscle mass and lipid content in high-fat, high-cholesterol (HFHC) diet-fed Lal-/- mice.
(A) Body weight curve during 6 weeks of HFHC diet feeding. **(B)** SM (quadriceps (QU), tibialis anterior (TA), gastrocnemius (GA), soleus (SO)) mass in female 16-18-week-old mice fasted for 6 h (n=4) after HFHC diet feeding. Biochemical analyses of the lipid content in **(C)** QU, **(D)** TA, **(E)** GA, and **(F)** SO (n=4). Data represent mean ± SD. *p ≤ 0.05, **p ≤ 0.01, ***p ≤ 0.001. Unpaired Student's t test.

3.9 Whole-body loss of LAL affects functions but not morphology of mitochondria

Despite inadequate FA uptake and reduced concentrations of acyl-CoA in the liver, mitochondrial function and energy production in hepatocytes of Lal-/- mice remained unaffected as previously described (263). To extend our insights into mitochondrial function in SM, we conducted a comprehensive assessment using high-resolution respirometry to measure the oxygen consumption rate in with saponin permeabilized SM fibers isolated from Lal-/- and Wt mice. Our results revealed that the absence of LAL caused a reduction at maximal respiration, driven by both complexes I and II upon the addition of succinate (GM_SP) and in the presence of the uncoupler CCCP (GMS_C) in permeabilized fibers from Lal-/- mice.

This observation suggests a broad impact on mitochondrial coupling in SM, as depicted in Figure 18A. In GA dissected from Lal-/- mice, further analyses of gene expression revealed a downregulation of mitochondrial transcription factor A (*Tfam*) that contributes to the transcription, organization, and maintenance of mtDNA (Fig. 18B).

However, we failed to detect any changes in mitochondrial morphology (Fig. 18C) or mitochondria number as confirmed by unaltered expression of the mitochondrial large subunit ribosomal RNA encoded by *16S* (Fig. 18D). Taken together, these results suggest impaired mitochondrial function at least in Lal-/- GA, regardless of the unaltered number or structure of mitochondria between the genotypes.

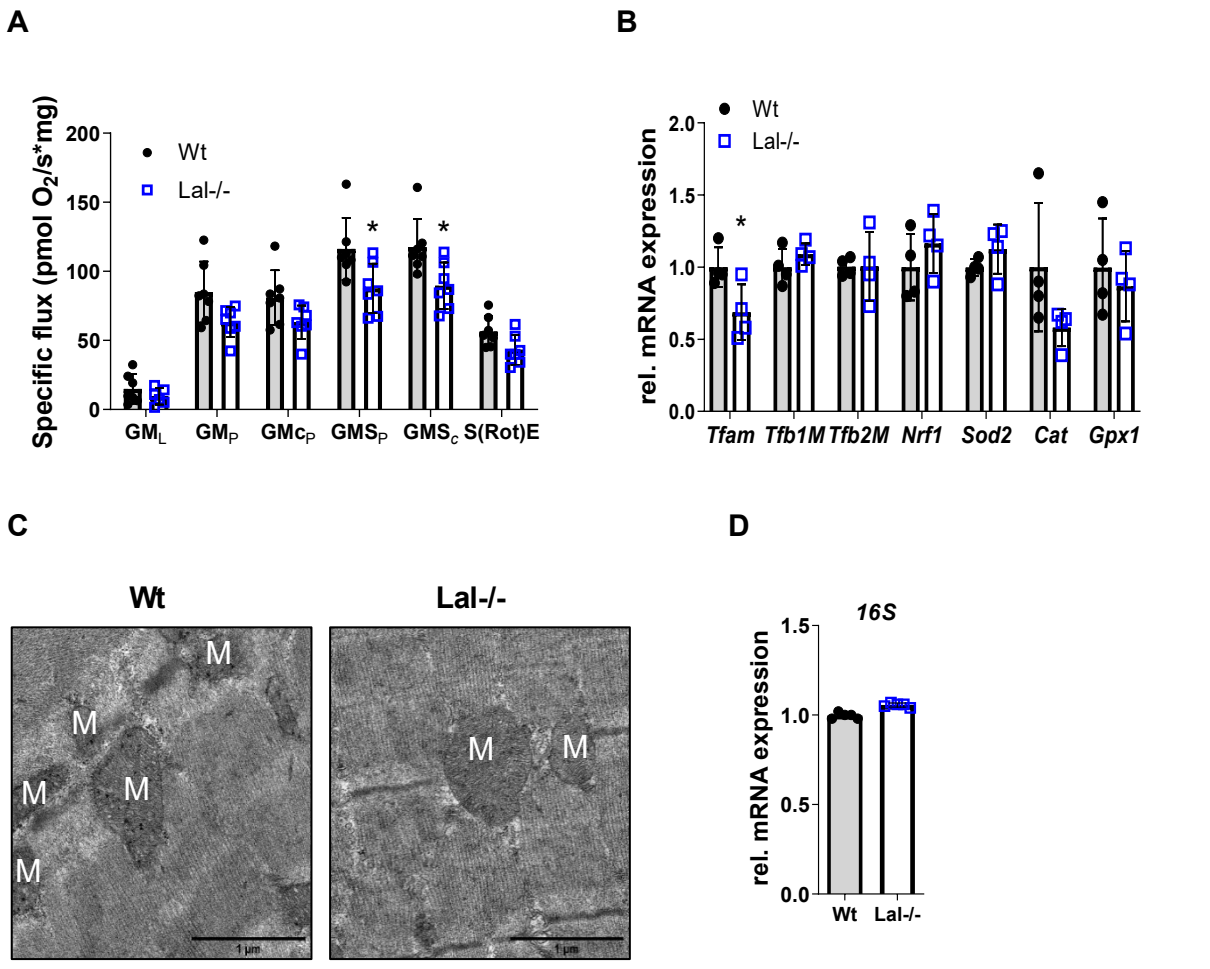

Figure 18: Reduced mitochondrial functions but unaltered mitochondrial morphology in gastrocnemius (GA) of Lal-/- mice.

(A) Oxygen consumption rate by mitochondria was assessed in permeabilized GA fibers from juvenile Lal /- and control mice using the Oxygraph-2k for detailed respirometry. Beginning with base respiratory rates in the non-phosphorylating condition facilitated by glutamate and malate: GM_L (G, glutamate; M, malate; L, LEAK), the capability for oxidative phosphorylation was gauged under full ADP saturation, designated GM_P, where pyruvate (P) served as an additional substrate. The integrity of the external mitochondrial membrane was probed using the GMc_P state, involving cytochrome C (c) as marker. Maximum capacity for oxidative

phosphorylation with simultaneous electron flow through complex I and II was characterized as GMS_P, through the incorporation of succinate (S). The highest capacity for electron transference independent of phosphorylation was discerned by GMS_C, where is *c* as CCCP - an uncoupling agent. Oxygen consumption attributed to non-mitochondrial sources, expressed as SE (E, electron transfer capacity), was quantified after the administration of rotenone (Rot) to elucidate the capacity for electron transfer (n=6). **(B)** Relative mRNA expression of mitochondrial genes in GA of young male Wt and Lal-/- mice (fed state) (n=3). **(C)** Representative electron micrographs of GA mitochondria from Wt and Lal-/- mice. M indicates mitochondria (scale bar,1 µm). **(D)** Mitochondrial DNA copy number in GA (n=5). Data represent mean ± SD. *p < 0.05. Unpaired Student's t test. The use of the figures **A, C, D** obtained from (269) is allowed under the terms described in the Appendix.

3.10 Whole-body inflammation in Lal-/- mice did not result in SM inflammation

LAL-D is associated with systemic inflammation and alterations in immune cell populations (293). Additionally, in mice it has been associated with increased levels of chemokines such as MCP-1 (encoded by *Ccl2*) (Fig. 19A) and hepatic and small intestinal macrophage infiltration (259, 294, 295), indicating a prominent role of inflammation in disease pathogenesis. We noted a decrease in the expression of *Il6* in the QU and GA muscles (Fig. 19B, D), and a similar reduction in *Tnfα* expression in TA (Fig.19C) from Lal-/- mice. A slight increase in *Ccl2* expression was also detected in TA (Fig. 19C) in the LAL knockout mouse model. We failed to detect any differences in expression of proinflammatory cytokines and the chemokine in SO of Lal-/- mice (Fig. 19E). However, the overall indication of inflammatory response in SM of Lal-/- mice remains inconclusive because the expression levels of the investigated genes were relatively low with Ct values around 29-30, which implies a scarce presence of the target RNA.

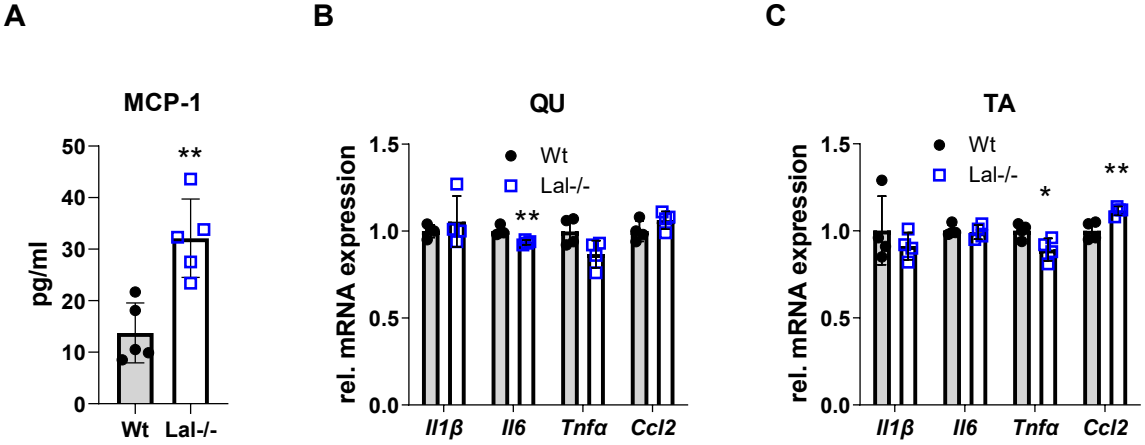

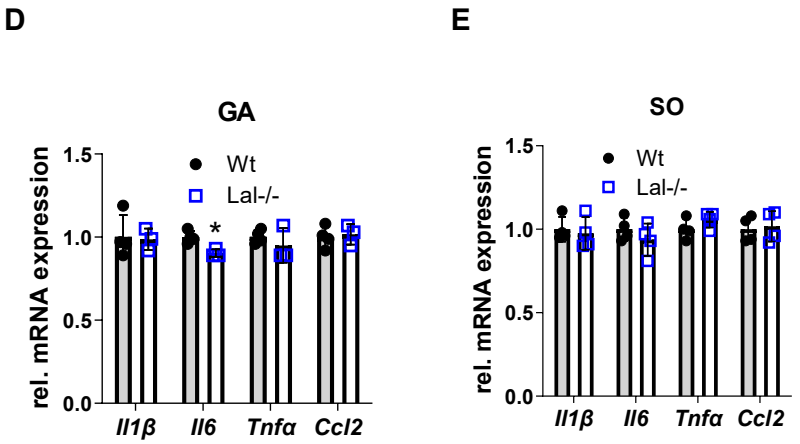

Figure 19: Systemic inflammation in Lal-/- mice is not associated with skeletal muscle inflammation.
(A) The circulating levels of monocyte chemoattractant protein-1 (MCP-1) in 50-58 weeks old 5h fasted female Lal-/- and Wt mice (n=5). RNA expression of proinflammatory cytokines and chemokines that regulate migration and infiltration of macrophages in young 12-h fasted female Lal-/- and Wt mice in **(B)** QU, **(C)** TA, **(D)** GA, and **(E)** SO (n=4). Gene expression was normalized to *cyclophilin A* as housekeeping gene. Data represent mean ± SD. *p < 0.05; **p ≤ 0.01.

3.11 Altered protein expression patterns in the SM of Lal-/- mice

The noted alterations not just between genotypes but also among muscles characterized by a predominance of oxidative (such as SO) or glycolytic (QU, TA, and GA) fibers prompted us to look deeper into the metabolism of Lal-/- SM with a specific focus on the fiber distributions.
The dissected GA muscle was divided in enriched in glycolytic or oxidative fibers parts. Then both GA segments underwent processing via LC-MS/MS, followed by the analysis of raw data files using DIA-NN software for protein quantification. Upon filtering for a minimum of four valid values in at least one group and imputing missing values, we quantified more than 3000 proteins in both dissected GA parts. Subsequent statistical analysis of the muscle proteome (FDR < 0.01, fold change > 0.1) unveiled 567 (300 downregulated and 267 upregulated) significantly altered proteins in oxidative muscle fibers and 430 (215 downregulated and 215 upregulated) in glycolytic ones. The MS proteomics data generated from the study have been made publicly available and were. submitted to the ProteomeXchange Consortium through the PRIDE partner repository (296). The specific dataset has been assigned the identifier PXD045665.
PCA identified distinct segregation patterns between oxidative (Fig. 20A) and glycolytic (Fig. 20B) segments of GA among both Lal-/- mice and their respective controls. Notably, in the more oxidative part, 32.66% of the variance was accounted for by the first principal component

and 12.16% by the second component, while in the more glycolytic part, these values were 53.72% and 11.02%, respectively.

Volcano plots, commonly used to visualize and identify proteins that exhibit substantial changes in the abundance between experimental conditions, depicted differences in both oxidative- and glycolytic-enriched fibers of the Lal-/- GA. The most upregulated protein in the oxidative and glycolytic parts of Lal-/- GA was alpha-1-acid glycoprotein 2 (A1AG2) and cathepsin S (CATS), respectively (Fig. 20C). Among the prominently upregulated proteins identified in both “red” and “white” muscle fibers were haptoglobin (HPT), ceruloplasmin (CERU), myosin heavy chain-7 (MYH7 or MyHCI), glutamine synthetase (GLNA), alpha-1-acid glycoprotein 1 (A1AGA), palmitoyl-protein thioesterase 1 (PPT1), and various types of troponins specific for slow SM, including troponin I (TNNI1) (Fig. 20C, D). The most downregulated protein identified in both the oxidative and glycolytic segments of the GA was major urinary protein (MUP). Unfortunately, it was challenging to visualize this protein on the volcano plot because the analysis had difficulty distinguishing between several isoforms of the respective protein. However, among the most downregulated proteins observed in both segments of the GA, we additionally identified insulin-like growth factor-binding protein 5 (IBP5), NADH dehydrogenase [ubiquinone] 1 alpha subcomplex assembly factor 2 (NDUF2), creatine kinase S-type, and mitochondrial (KCRS), collagen alpha-1(III) chain (CO3A) (Fig. 20C, D). In addition, cytochrome c oxidase assembly factor 7 (COA7), cytochrome c oxidase subunit 5A, mitochondrial (COX5A), ATP synthase subunit delta, mitochondrial (ATPD), and acyl-CoA-binding domain-containing protein 6 (ACBD6) were significantly downregulated in the more glycolytic part of GA (Fig. 20D). Notably, the majority of the upregulated proteins were associated with muscle structure and function, while the downregulated proteins were primarily linked to mitochondrial function and metabolism (269).

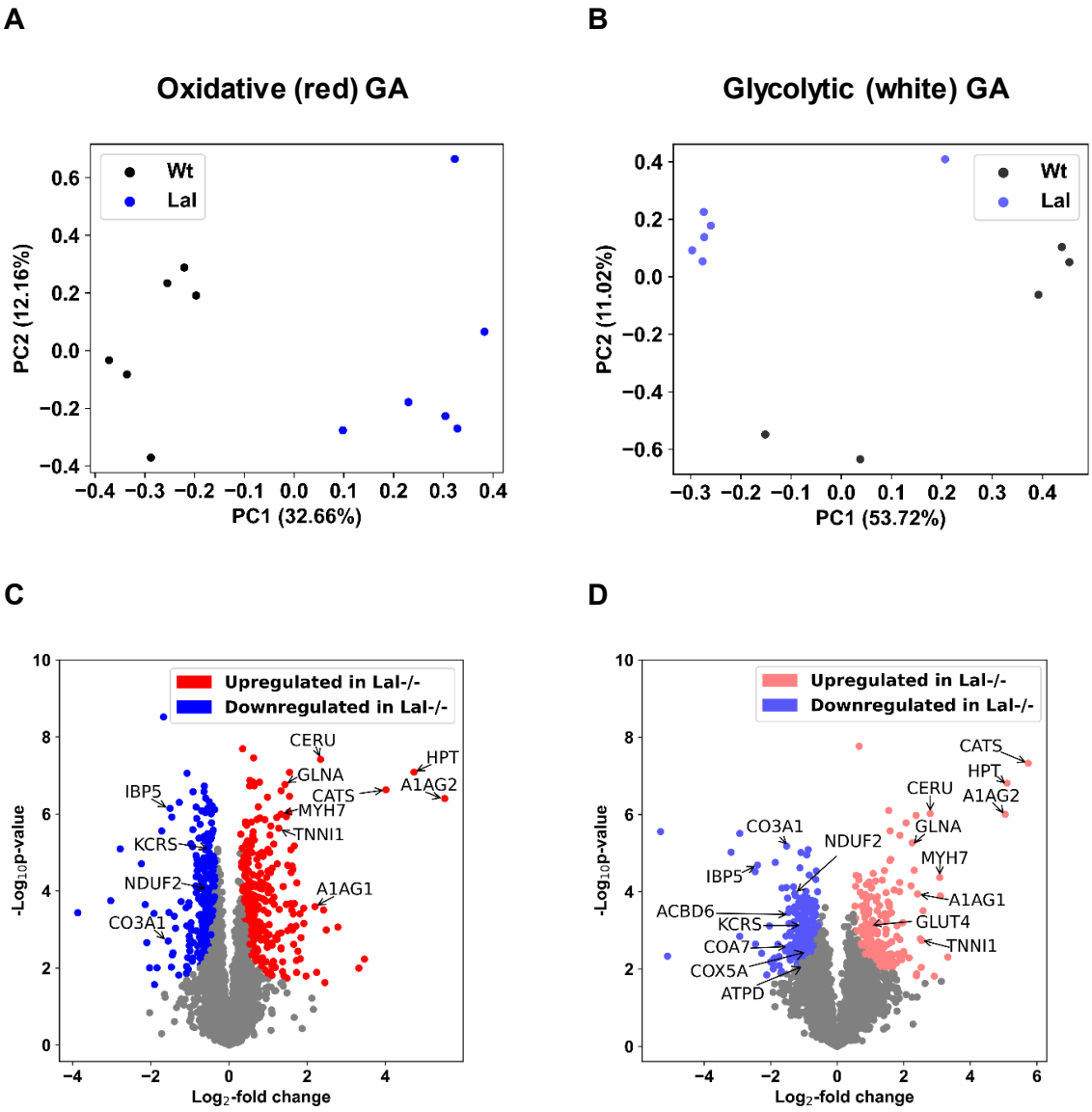

Figure 20: Proteomic analysis reveals differential protein abundance in oxidative and glycolytic muscle fibers of Lal-/- mice.
Principal component analysis (PCA) was performed on the proteome data obtained from SM of young *ab libitum* fed Wt and Lal-/- mice, allowing for the clear differentiation of both the **(A)** oxidative and **(B)** glycolytic components within gastrocnemius (GA). The volcano plots depict the differences in protein abundance in the **(C)** oxidative and **(D)** glycolytic parts of GA from juvenile male Wt or Lal-/- mice. Blue dots indicate proteins downregulated in Lal-/- mice, red dots represent proteins upregulated in Lal-/- mice, and grey dots denote unchanged protein expression between genotypes. The data are based on n = 5-6 mice per group, with significance thresholds set at S0 = 0.1 and FDR < 0.01. The use of this figure obtained from (269) is allowed under the terms described in the Appendix.

We proceeded with PANTHER, a widely utilized bioinformatics tool in proteomics (280), to uncover overrepresented Gene Ontology Biological Processes (GOBP), Gene Ontology Cellular Component (GOCC), and Reactome pathways. This analysis uncovered substantial changes, particularly in mitochondrial functions (downregulated oxidative phosphorylation,

electron transport chain, and ATP synthesis-coupled electron transport), along with RNA (upregulated mRNA processing and regulation of mRNA metabolic processing) within the oxidative segment of GA. This was evident from the significant enrichment of these terms among the top-ranking GOBP terms (Fig. 21A). Conversely, in the glycolytic part, the enriched upregulated terms predominantly involved a spectrum of metabolic and catabolic processes such as organic and carboxylic acids, lipid, and acyl-CoA metabolic processes (Fig. 21B). Notably, protein folding emerged as the most downregulated biological process within the glycolytic GA part (Fig. 21B). This unexpected finding suggests potential disruptions in protein folding mechanisms within the glycolytic muscle fibers (Fig. 21B), indicating intricate regulatory dynamics in response to specific physiological conditions or genetic alterations.

Following these observations, the most prominently enriched downregulated terms in GOCC included respirasome, inner mitochondrial membrane protein complex, oxidoreductase, and mitochondrial respiratory chain I complexes (Fig. 21C) within the oxidative GA part. Unexpectedly, no downregulated GOCC terms were found to be enriched in the glycolytic segment of GA from Lal-/- mice (Fig. 21D). Notably, the most upregulated terms in the glycolytic GA were nucleosome, heterotrimeric G-protein complex, extrinsic components of cytoplasmic side of membrane as well as GTPase complex and myosin filament (Fig. 21D), mirroring observations in the oxidative part of GA, including the spliceosome, nuclear protein-containing, and myosin complexes (Fig. 21C). These findings underscore the dynamic alterations in the GOCC composition and organization occurring in response to distinct metabolic demands and functional adaptations within different segments of the GA.

Analysis of the Reactome pathways provides a further comprehensive collection of curated pathways, including metabolic pathways, signaling cascades, and molecular interactions (297). Among the most upregulated Reactome pathways in the oxidative part of GA were mRNA splicing – major pathway, gene expression, and muscle contraction (Fig. 21E). Interestingly, in the glycolytic part of GA, upregulated Reactome pathways were transport of small molecules, metabolism of lipids, and integration of energy metabolism (Fig.21F). The downregulated terms included translation, specifically mitochondrial translation and TCA cycle in the oxidative SM part (Fig. 21E) as well as respiratory electron transport, endosomal sorting compels, and mitochondrial iron-sulfur cluster biogenesis in the glycolytic one (Fig. 21F) (269).

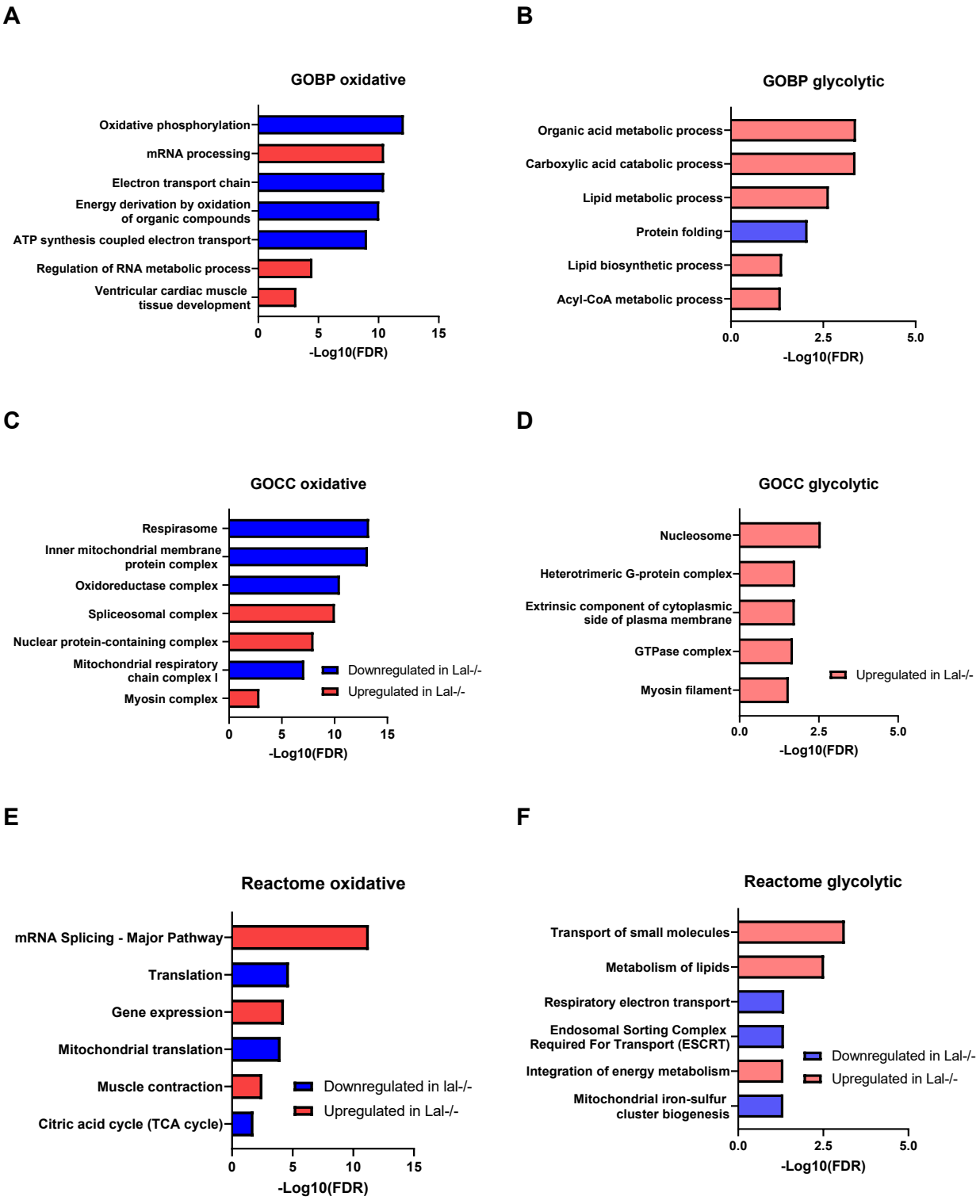

Figure 21: Top selected Gene Ontology (GO) terms associated with proteins enriched in skeletal muscle (SM) of Lal-/- mice.
Analyses of downregulated (blue) and upregulated (red) GO term in the **(A, C, E)** oxidative and **(B, D, F)** glycolytic parts of GA in juvenile Wt and Lal /- mice (fed state) performed by PANTHER. **(A, B)** A comparative analysis of GO terms associated with enriched proteins in Lal-/- SM, categorized by biological processes (GOBP). **(C, D)** The top selected Gene Ontology

Cellular Component (GOCC) terms, revealing cellular localization changes in response to LAL deficiency. **(E)** and **(F)** depict significantly enriched Reactome pathways identified within the oxidative and glycolytic muscle fibers, respectively, providing insights into molecular pathways affected by the absence of LAL. The use of this figure obtained from (269) is allowed under the terms described in the Appendix.

The oxidative- or glycolytic-enriched fiber parts of GA showed similar patterns in the clusters of differentially expressed proteins that were identified by network analysis using protein-protein interactions displayed in Cytoscape. Notably, both parts revealed clusters of many downregulated proteins linked to mitochondrial and oxidative phosphorylation (Oxphos) (Fig. 22A, B), which may indicate mitochondrial malfunction in Lal-/- SM. Moreover, a different set of downregulated proteins grouped around ER functions linked to protein folding and processing (Fig. 22A, B), suggesting disturbances in ER homeostasis in GA from Lal-/- mice. Several downregulated proteins were also clustered in glucose metabolism (Fig. 22B) or glucose homeostasis and TCA cycle (Fig. 22A), whereas glycolysis or lipid metabolism clusters contained proteins that did not correspond to a certain expression pattern (Figure 22A).
On the other hand, there was an abundance of upregulated proteins clustered around functions associated with muscle contraction in both parts of the GA (Fig. 22A, B), as well as muscle development, particularly in the more oxidative part (Fig. 22A) (269).

A

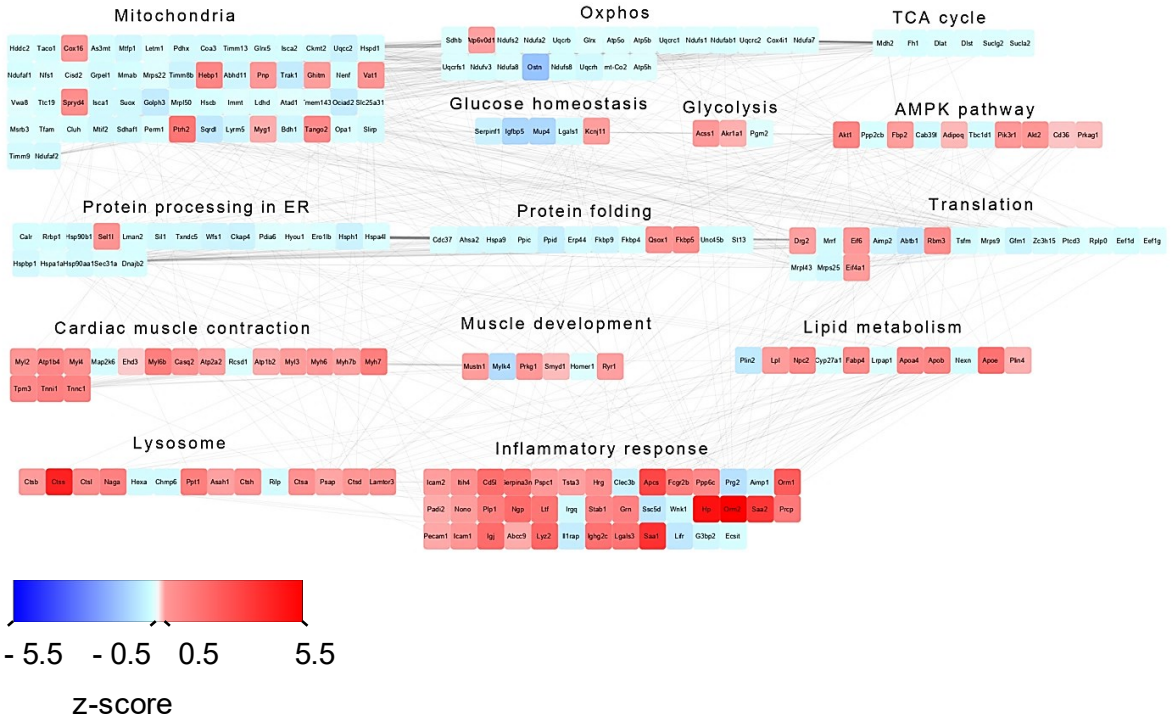

B

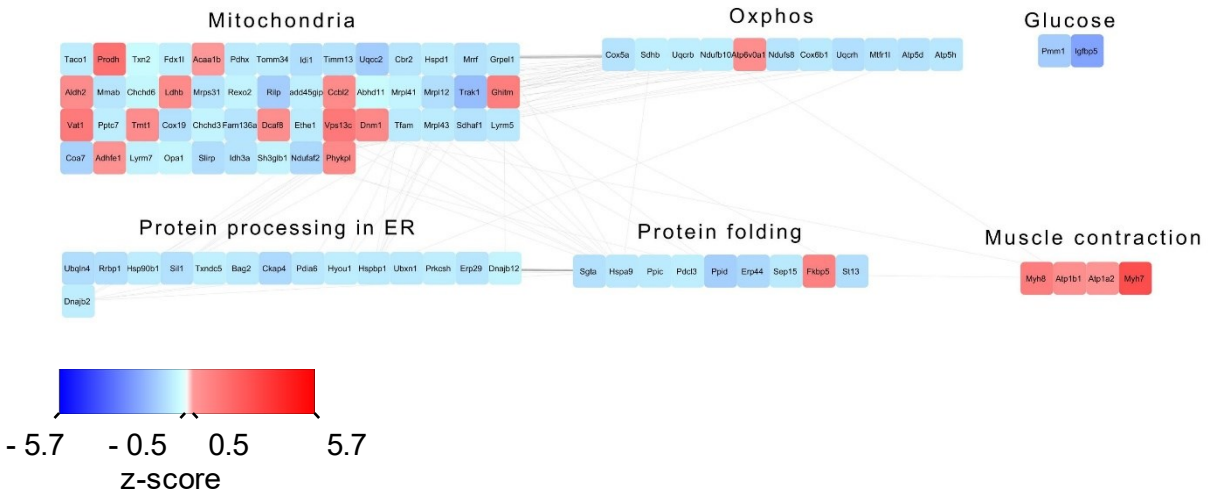

Figure 22: The protein-protein interaction network revealed alterations in biological processes, including mitochondria structure and functions. The protein-protein interaction network is based on clusters of up- and downregulated proteins in the gastrocnemius (GA) of young Lal-/- mice in the fed state. The interaction network was generated by Cytoscape using highlighted up- and down-regulated proteins enriched in **(A)** oxidative and **(B** glycolytic segments from GA. Blue color represent proteins with z-score < -0.5; red represents a z-score > 0.5. The use of this figure obtained from (269) is allowed under the terms described in the Appendix.

3.12 Increased expression of proteins specific for oxidative myofibers in Lal-/- mice

Proteomics analysis revealed strong upregulation of the slow skeletal fiber markers MyHCI (MYH7) and troponin C1 (TNNC1) in both the oxidative and glycolytic parts of GA. Quantitative PCR analysis revealed an upregulation of *Myh7* gene expression in GA (Fig. 23C) and SO (Fig. 23D) muscles of Lal-/- mice. In contrast, only a suggestive trend towards increased *Myh7* expression was observed in QU (Fig. 23A) and TA (Fig. 23B), without reaching definitive statistical significance. We confirmed the increased MyHCI protein expression in QU and GA of Lal-/- mice by Western blotting (Fig. 23E) and in TA and GA sections by immunofluorescent staining with MyHCI antibody coupled with laminin (Fig.23F). These findings hint to an overexpression of slow oxidative fibers in Lal-/- SM (269).

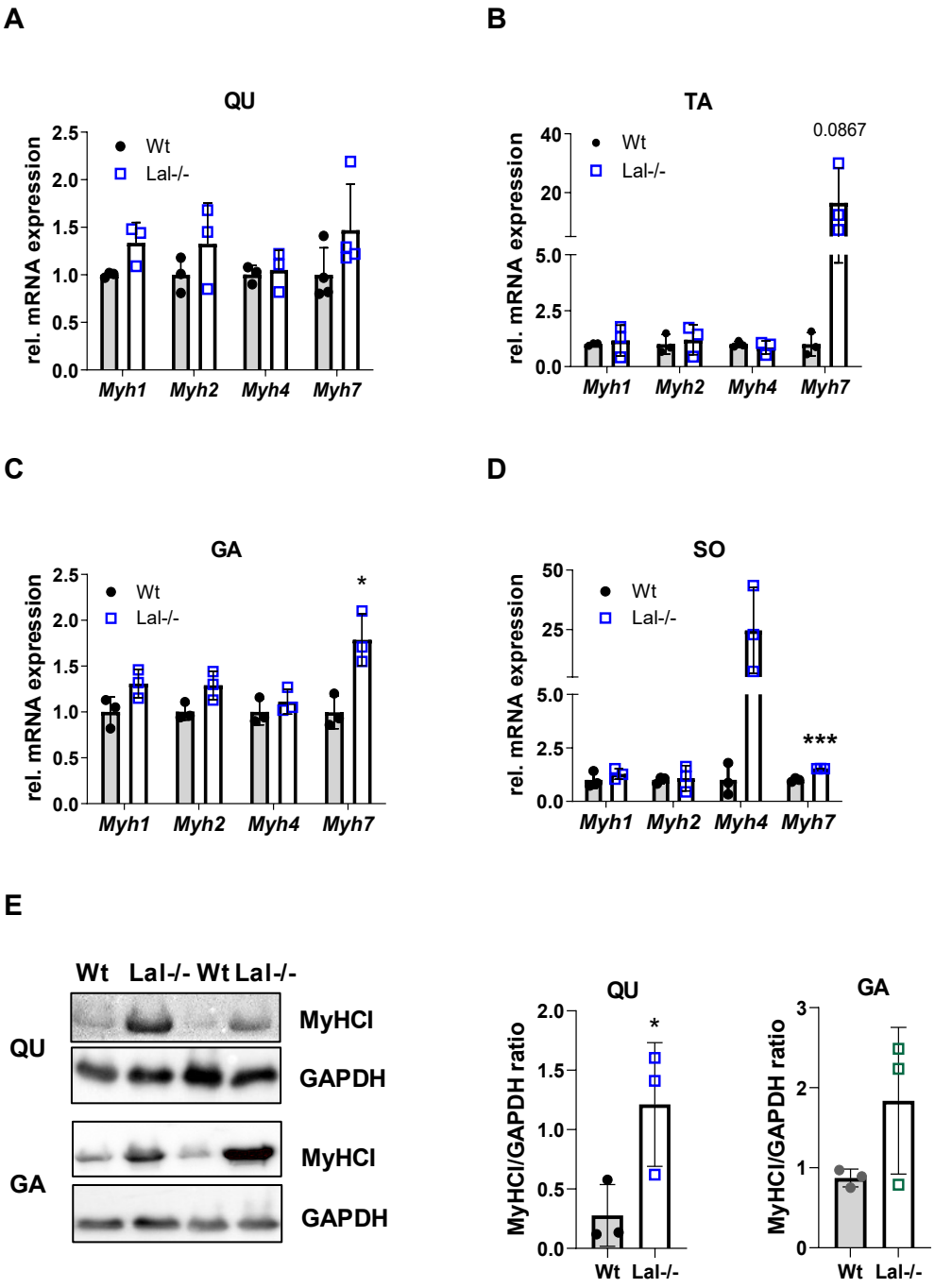
A
QU
rel. mRNA expression
Wt
Lal-/-
Myh1
Myh2
Myh4
Myh7
B
TA
0.0867
C
GA
*
D
SO
***
E
Wt
Lal-/-
MyHCI
GAPDH
MyHCI/GAPDH ratio

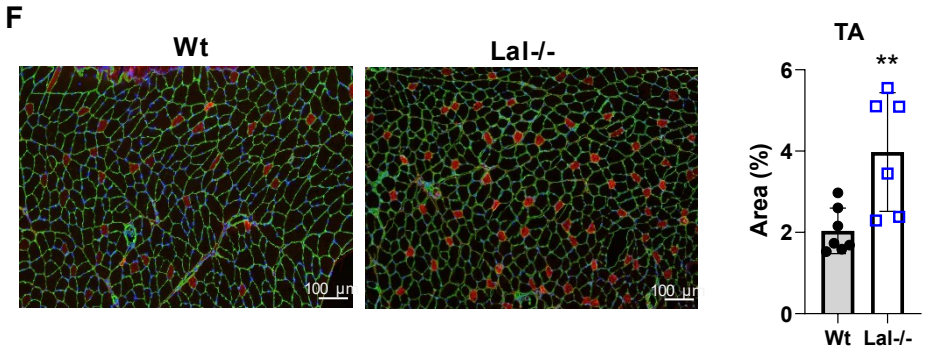

Figure 23: Upregulated gene and protein expression of oxidative fiber-specific myosin heavy chain.
Relative mRNA expression of genes encoding different isoforms of myosin heavy chain (*Myh*) in **(A)** quadriceps (QU), **(B)** tibialis anterior (TA), **(C)** gastrocnemius, and **(D)** soleus (SO) of male mice in the fed state (n=3-4) relative to *cyclophilin A* expression as reference gene. **(E)** Representative Western blotting experiment of MyHCI, protein expression, and densitometric quantifications relative to GAPDH (n=3) in QU and GA from 6-h fasted young male Lal-/- mice and their respective controls. **(F)** Co-staining of MyHCI (red) and laminin (a protein of the extracellular matrix, green) in TA sections from Lal-/- and Wt mice. Cell nuclei within these tissues have been highlighted using DAPI staining (blue). Scale bar, 100 µm. The graph displays the quantification of the MyHCI-positive areas within the tissue sections, measured through Image J software, with data represented as mean values derived from 2 to 3 technical replicates across samples from 3 different mice. Data represent mean ± SD. *p ≤ 0.05, **p ≤ 0.01, ***p ≤ 0.001. Unpaired Student's t test. The use of this figure obtained from (269) is allowed under the terms described in the Appendix.

3.13 Reduced performance in peak effort testing associate with affected metabolites in SM of Lal-/- mice

To examine SM functions and whether the observed changes in fiber types translate into reduced physical activity, we performed the hanging wire test, in which the mice are forced to hang from a wire and their latency to fall is measured (281). Interestingly, we observed a tendency to improved performance of Lal-/- mice in this motoric test (Fig. 24A). However, these results may be influenced by the animal's weight, balance, and behavior (298). Due to the reduced body weight of Lal-/- mice compared to their control littermates, we compared impulses and weight (in grams) times time (in s), which reflects the least amount of sustained tension (impulse) required to counteract gravity (281). These results revealed similar motoric conditions between the genotypes (Fig. 24B).

To detect fatigue-like behavior in our model, we performed the treadmill peak effort test coupled with indirect calorimetry. Lal-/- mice displayed a shorter running distance (Fig. 24C) and a substantially decreased total workload (Fig. 24D). This concomitantly led to reduced

peak aerobic capacity (Fig. 24E) and showed significantly reduced time until exhaustion due to effort resistance in Lal-/- mice (269).

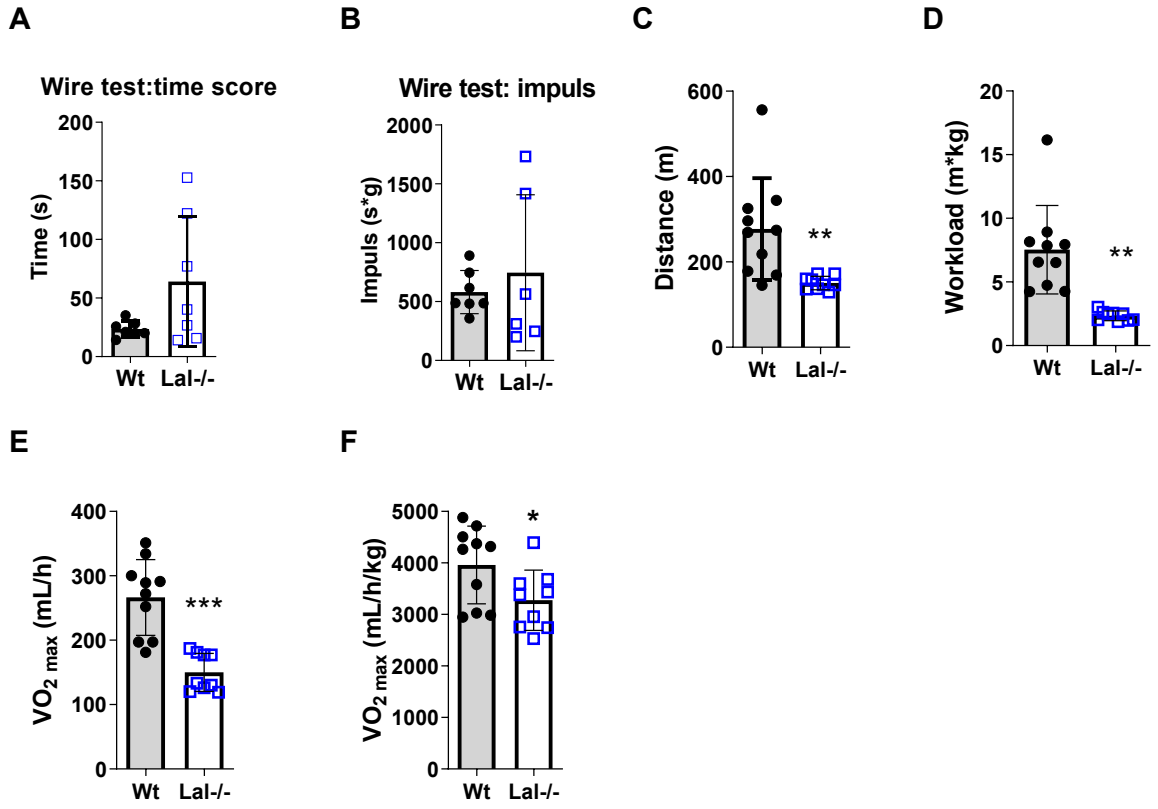

Figure 24: Unchanged hanging time but decreased treadmill exercise performance in Lal-/- mice.
(A, B) Hanging wire test performance time or impulse of 10-13 weeks old Lal-/- and Wt mice (n=7). **(C)** Maximal running distance, **(D)** workload, and **(E, F)** maximal oxygen consumption (VO_{2max}) in 16-18 weeks old Lal-/- mice and their Wt littermates during peak effort testing on a treadmill (n = 9-10 mice per group). Data show mean ± SD. *p ≤ 0.05, **p ≤ 0.01, ***p ≤0.001. Unpaired Student's t test. The use of the figures **C-F** obtained from (269) is allowed under the terms described in the Appendix.

The peak treadmill exercise test may provide valuable insights not just into the SM functions but also the metabolite profile and thus metabolic adaptations in Lal-/- mice. The observed significant changes in metabolites in both oxidative and glycolytic segments of the GA, as quantified by NMR, are presented in the heatmap (Fig. 25A). The increase in creatine levels in both oxidative and glycolytic parts of GA from Lal-/- mice (Fig. 25B) suggests a stronger demand for ATP in the SM of exercised Lal-/- mice. Unexpectedly, the concentrations of lactate (Fig. 25C) and glycogen (Fig. 25D) remained unchanged. Furthermore, the observed decrease in succinate levels in oxidative Lal-/- GA fibers, while remaining unchanged in glycolytic segments, suggests differential regulation of TCA cycle metabolites in response to exercise

(Fig. 25E). The notable increase in taurine levels in both studied fiber types of GA from Lal-/- mice (Fig. 25F) highlights the potential role of taurine in the adaptive responses of Lal-/- SM to endurance training.

The alterations in glucogenic AA such as Ala, Gly, and His in glycolytic fibers (Fig. 25G) and the increased Arg levels in the oxidative part of the GA from treadmill-trained Lal-/- mice suggest their additional role in maintaining energy needs in SM of Lal-/-. However, the slight increase in Phe levels in oxidative GA fibers (Fig. 25H), but no alterations in ketogenic AA (Fig. 25I) may suggest only a minor role of AA in mice trained until exhaustion. Overall, these findings suggest that while the hanging wire test indicated no sign of strength loss in Lal-/- mice, the treadmill peak effort test revealed reduced physical performance and increased fatigue, possibly due to complex metabolic adaptations in GA by the loss of LAL.

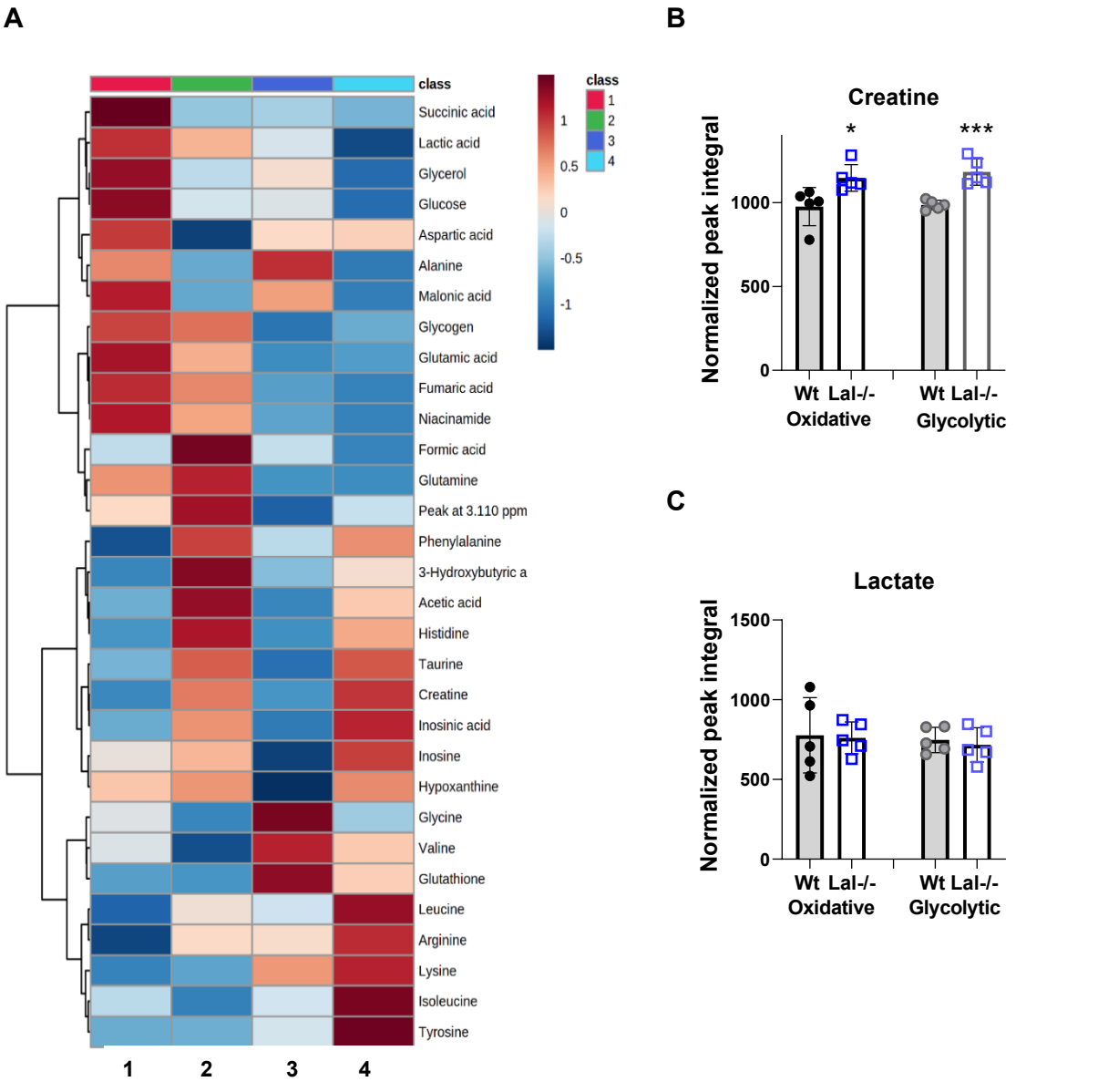

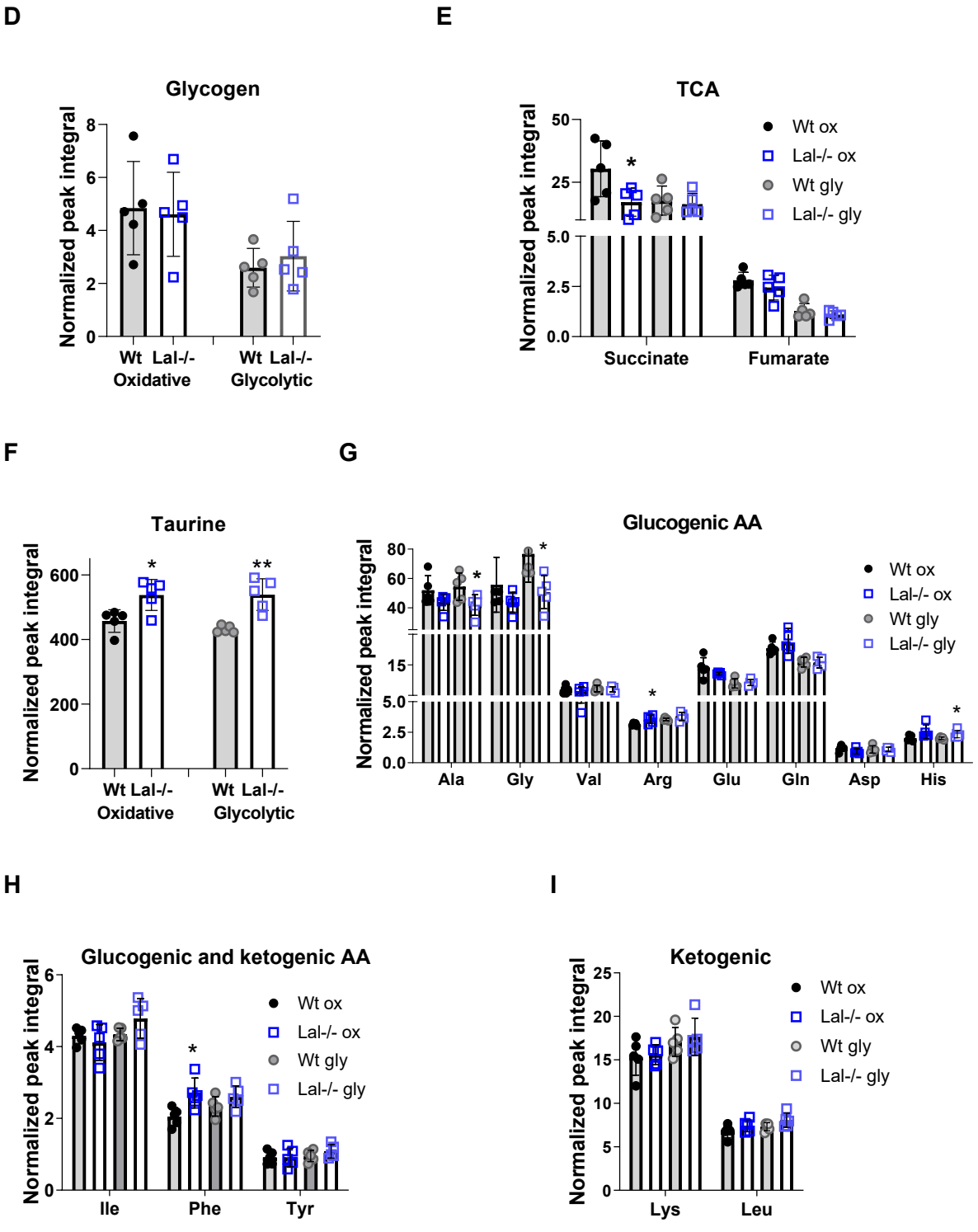

Figure 25: Altered metabolite concentration in treadmill trained Lal-/- mice.
(A) Heatmap of NMR analysis showing the relative metabolite levels in oxidative (ox) and glycolytic (gly) parts of GA from young male Lal-/- and Wt mice where class 1 is Wt oxidative GA segment, class 2 is Lal-/- oxidative GA segment, class 3 is Wt glycolytic GA segment, and class 4 is Lal-/- glycolytic GA segment. **(B-F)** Concentrations of metabolites quantified by NMR

and expressed as standardized peak intensities in GA separated for glycolytic and oxidative parts from young male mice. Individual **(G)** glucogenic, **(H)** glucogenic/ketogenic, and **(I)** ketogenic AA quantified by NMR and presented as normalized peak integral enriched in ox or gly segments of GA from Lal-/- or Wt mice after peak effort testing. Data represent mean ± SD. *p < 0.05, **p ≤ 0.01, ***p ≤ 0.001. Unpaired Student's t test.

3.14 Inhibition of LAL in C2C12 cells and primary myoblasts

The observed changes in SM of Lal-/- mice raised the question of whether these variations are a direct consequence of LAL loss in SM or reflect systemic effects of LAL-D throughout the body. Furthermore, despite a slight trend toward decreased QU mass in juvenile mice, our study revealed decreased levels of regulated proteins, including IGFBP-5 (299), recognized in previous studies as a marker indicative of impaired SM differentiation. Hence, I further investigated SM development in Lal-/- mice.

To address these questions, I utilized primary myoblasts isolated from SM devoid of *Lipa* gene expression (Fig. 26A). Additionally, I used mouse myoblast-derived C2C12 cells as another model widely employed to study muscle regeneration and differentiation (300). To investigate whether the loss of LAL affects metabolism and growth of newly formed fibers, I incubated C2C12 cells with the LAL inhibitor Lalistat-2. Since this inhibitor has also been shown to inhibit other lipases, including ATGL, HSL, and MGL (236), it was crucial to use a concentration of the inhibitor that only inhibits LAL and no other enzymes. I therefore treated C2C12 cells with different concentrations of Lalistat-2 (0.1, 1, and 10 µM) and performed CE and TG hydrolase activity assays. These results showed that 0.1 µM Lalistat-2 specifically reduced the activities of acid CE and TG hydrolase (Fig. 26B, C), whereas concentrations > 0.1 µM also reduced neutral CE and TG hydrolase activities (Fig. 26D, E), suggesting off-target effects of Lalistat-2 also in muscle cells. Based on these findings, I performed further experiments with C2C12 cells using a concentration of 0.1 µM of Lalistat-2.

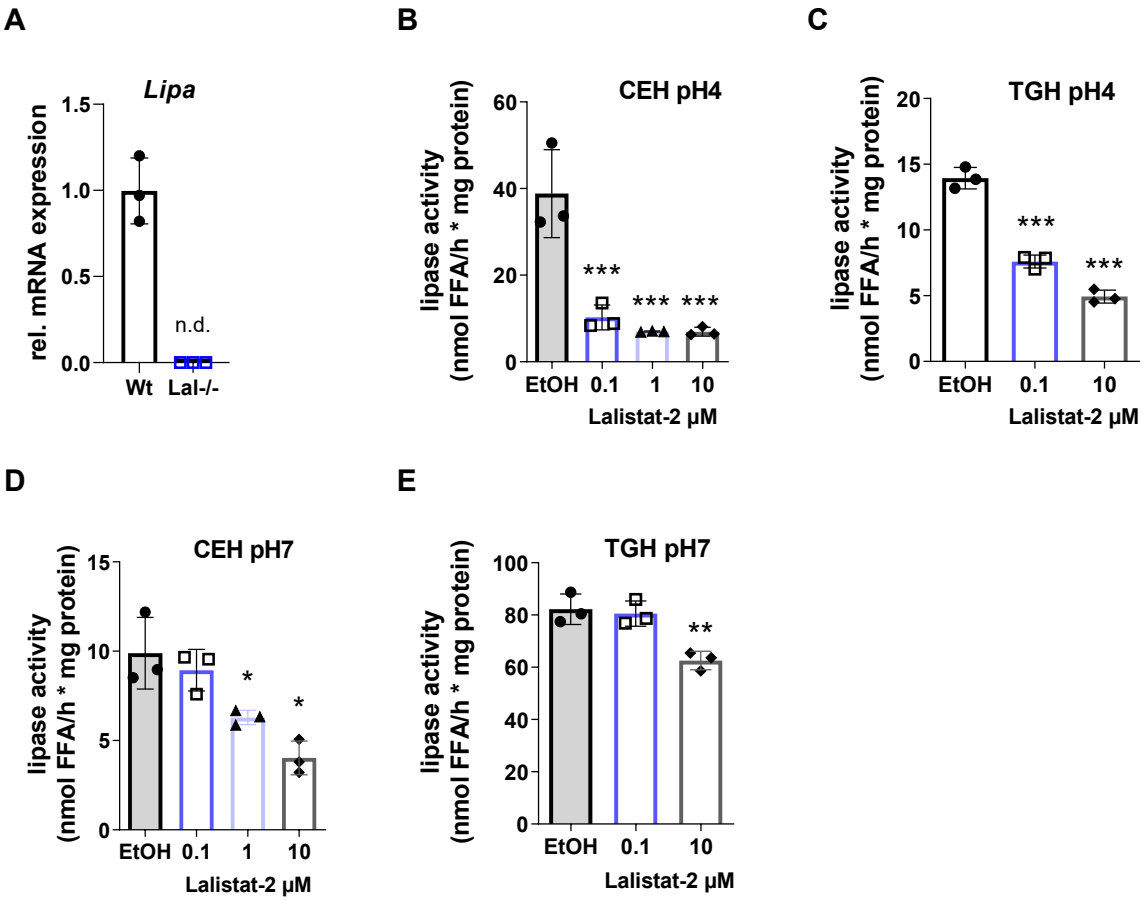

Figure 26: Successful inhibition of LAL activity in C2C12 cells.
(A) Relative gene expression of *Lipa* in primary myoblasts isolated from Lal-/- and Wt mice during differentiation (n=3). Cholesteryl ester hydrolase (CEH) activity at **(B)** acidic pH and **(D)** neutral pH as well as triglyceride hydrolase (TGH) activity at **(C)** acidic pH and **(E)** neutral pH in C2C12 cells treated with different concentrations of Lalistat-2**.** Data represent mean ± SD. *p < 0.05, **p ≤ 0.01, ***p ≤ 0.001. (A) Unpaired Student's t test. (B-E) One-way ANOVA.

Treatment of C2C12 cells with 0.1 µM of Lalistat-2 did not affect their viability (Fig. 27A) or proliferation rate (Fig. 27B), indicating that this concentration of Lalistat-2 is not toxic to this cell line. Primary myoblasts isolated from Lal-/- mice were both viable and proliferated at rates similar to Wt cells (Fig. 27C). This suggests that the absence or inhibition of LAL does not adversely affect cell growth in primary myoblasts and C2C12 cells compared with controls.

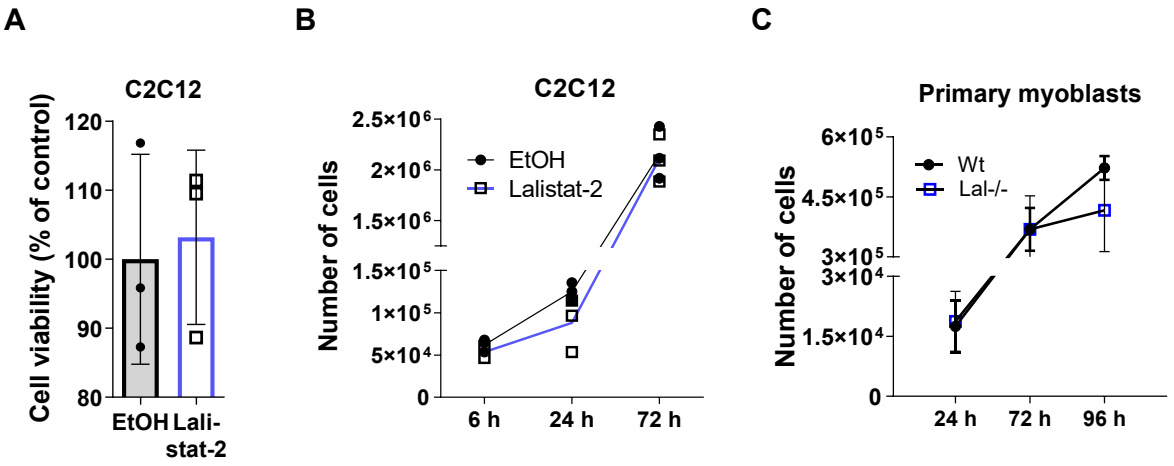

Figure 27: Inhibition of LAL in C2C12 cells and LAL-D in primary myoblasts does not affect cell proliferation and viability.
(A) Cell viability of differentiating C2C12 cells treated with 0.1 µM of Lalistat-2 in % of control (0.1% EtOH) (n=3). **(B)** Proliferation rate of C2C12 cells treated with 0.1 µM of Lalistat-2 (n=3). **(C)** Proliferation rate of primary myoblasts isolated from Lal-/- mice and their respective controls (n=4). Data represent mean ± SD. **(A)** Unpaired Student's t test. **(B, C)** One-way ANOVA.

3.15 Inhibition of LAL in C2C12 cells and LAL-D in primary myoblasts leads to lipid accumulation

Treatment with 0.1 µM of Lalistat-2 resulted in lipid accumulation in proliferating C2C12 cells, as demonstrated by ORO staining (Fig. 28A). Quantitative analysis of lipids revealed increased concentrations of TG, TC, and CE, along with a decrease in FC levels (Fig. 28B). Of note, Lal-/- mice exhibit markedly reduced very low-density lipoprotein concentration (263). To mimic these conditions in vitro, we cultivated Lalistat-2-treated C2C12 cells in DMEM containing lipoprotein-deficient serum (LPDS). Under these conditions, staining with ORO showed no visible lipid accumulation in cells treated with Lalistat-2 (Fig. 28C), which was confirmed by unchanged lipid parameters (Fig. 28D).
In line with observations from C2C12 cells treated with Lalistat-2, primary myoblast cultures derived from Lal-/- mice similarly exhibited lipid deposition as evidenced by ORO staining, identifying areas of lipid accumulation (Fig. 28E). Subsequent assessments demonstrated an elevation in both TC and CE concentrations within differentiated primary myoblasts from Lal-/- mice compared to those from Wt controls. However, TG levels remained consistent across both genotypes (Fig. 28F). Overall, although there was no specific pattern of lipid accumulation in the SM of adult Lal-/- mice, we observed an increase or a trend toward an increase in

cholesterol concentrations, indicating that the loss of LAL affects the lipid profile also in the SM.

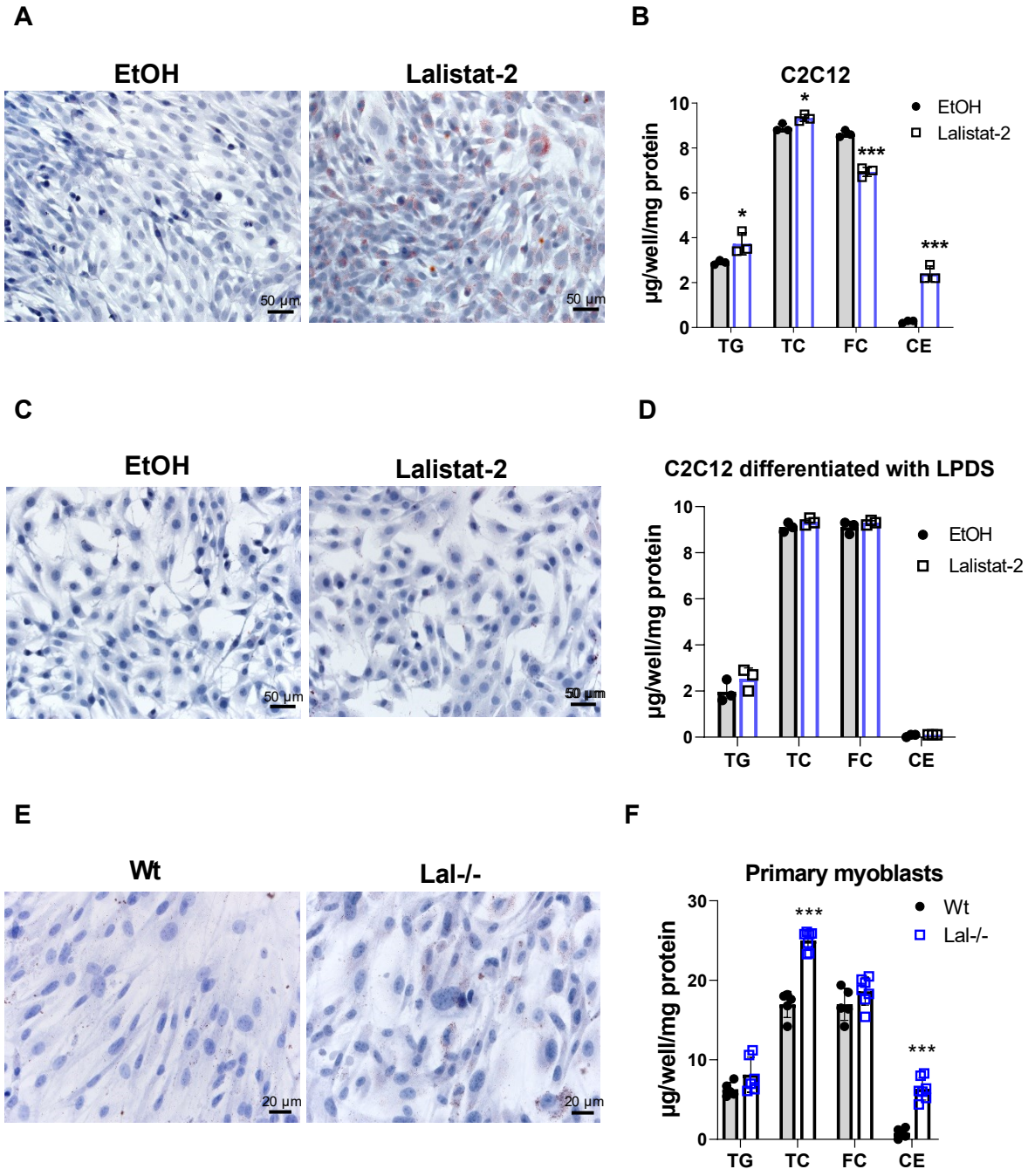

Figure 28: Inhibition of LAL in C2C12 cells and LAL-D in primary myoblasts results in lipid accumulation.
Representative images of ORO staining of proliferating C2C12 cells in medium containing either **(A)** 10% fetal bovine serum (FBS) or **(C)** 10% lipoprotein-deficient serum (LPDS) treated with 0.1 µM of Lalistat-2 (scale bar, 50 µm) and **(E)** primary myoblasts isolated from Lal-/- and Wt mice (scale bar, 20 µm). Biochemical analyses of lipid content in differentiated C2C12 cells **(B)** growing in medium containing 2% horse serum (HS) or **(D)** 10% LPDS treated with Lalistat-

2 (n=3) and **(F)** primary myoblasts isolated from Lal-/- and Wt mice (Wt, n=4; Lal-/-, n=7). Data represent mean ± SD. *p ≤ 0.05, ***p ≤ 0.001. Unpaired Student's t test.

3.16 Inhibition of LAL in C2C12 and LAL-D in primary myoblasts does not affect myofiber formation

The renewal of muscle cells through cellular processes such as proliferation and differentiation plays a crucial role in maintaining muscle mass (286). To investigate the effect of LAL inhibition on myocyte differentiation, confluent C2C12 cells were treated with 0.1 µM of Lalistat-2 for 6 days. mRNA expression of the main myofiber differentiation markers myogenin (*Myog*), myoblast determination protein 1 (*Myod*), and myogenic factor 6 or herculin (*Myf6*)) remained unaltered, whereas mRNA levels of myogenic factor 5 (*Myf5*) were slightly reduced (Fig. 29A). Unexpectedly, the evaluation of gene expression of the main differentiated markers in primary myoblasts revealed minor upregulation in *Myog*, *Myf5*, and *Myf6* in cells isolated from Lal-/- SM (Fig. 29B). The results from both studied cell models suggest that LAL-D is not associated with impaired myofiber formation.

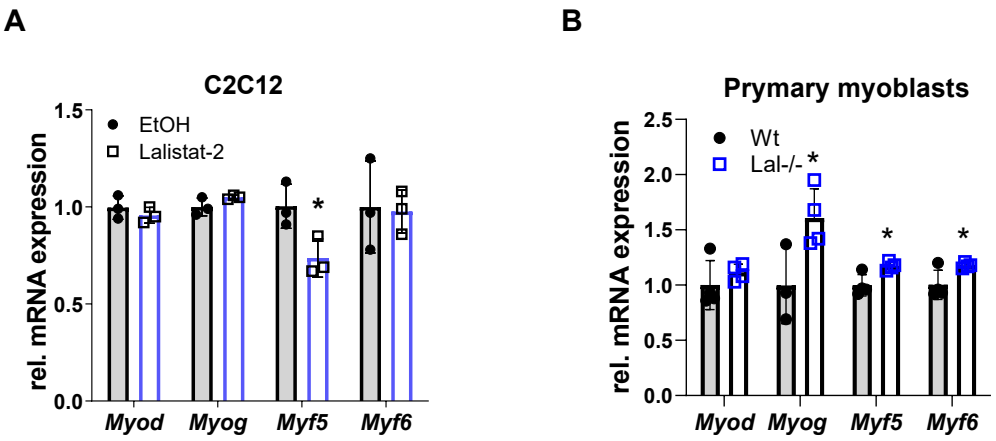

Figure 29: Unchanged fiber formation in C2C12 cells treated with Lalistat-2 and in LAL-D primary myoblasts.
Relative mRNA expression of genes encoding differentiation markers genes of SM fibers relative to *cyclophilin A* expression as reference gene in **(A)** C2C12 cells treated with 0.1 µM of Lalistat-2 or 0.1% EtOH for 6 days during differentiation (n=3) and in **(B)** differentiated primary myoblasts from Wt and Lal-/- mice (n=4). Data represent mean ± SD. *p ≤ 0.05. Unpaired Student's t test.

3.17 Loss of LAL in myoblasts and inhibition of LAL activity *in vitro* do not affect the expression of myosin isoform specific to oxidative fibers

I have described earlier an increased expression of markers specific for oxidative, slow-twitch fibers in Lal-/- mice. In our *in vitro* model, *Myh7* expression was similar in C2C12 cells treated with either EtOH or Lalistat-2 (Fig. 30A) and in primary myoblasts isolated either from Lal-/- SM or their respective controls (Fig. 30B).

In addition, mRNA expression of *Myh3* (specific for developing fibers), *Myh1* as the fast glycolytic fiber marker, and protein expression of MyHCIIx, the predominant isoform of MyHC in C2C12 cells, were comparable between cells treated with Lalisat-2 or EtOH (Fig. 30C, D). These findings were confirmed by comparable immunofluorescent staining patterns in EtOH- and Lalistat-2-treated cells (Fig. 30E). Surprisingly, despite unchanged *Myh1* and *Myh3* gene expression (Fig. 30F), levels of MyHCIIx protein (Fig. 30G) were significantly reduced in differentiated myoblasts from Lal-/- mice. Thus, these inconsistent patterns in MyHC expression in all studied models suggests that alterations observed in SM of Lal-/- mice may stem from systemic alterations rather than being directly caused by the loss of LAL in SM.

A

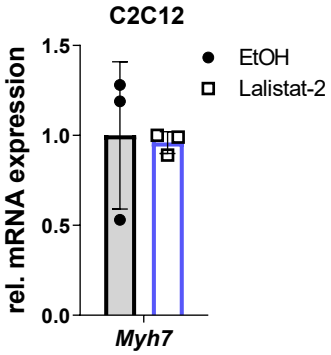

B

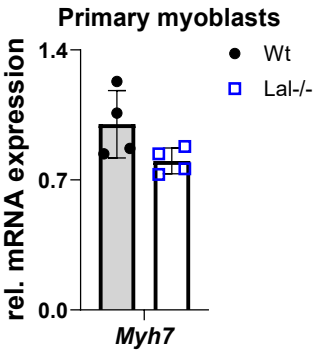

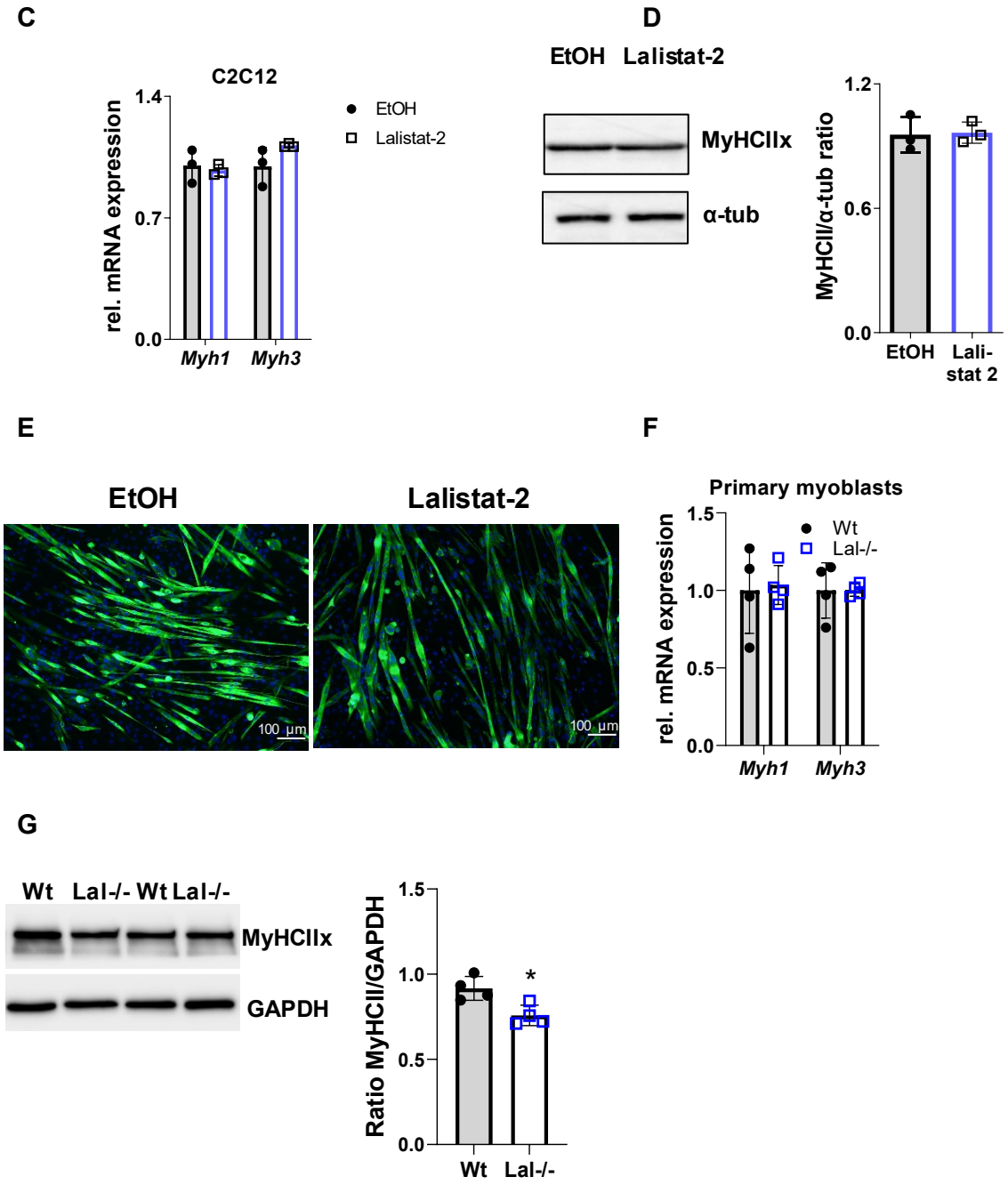

Figure 30: Inhibition of LAL in C2C12 cells and LAL-D in primary myoblasts do not affect expression of myosin heavy chain (MyHC) specific for slow oxidative fibers.
Relative mRNA expression of genes encoding **(A, B)** MyHCI (*Myh7*) or **(C, F)** MyHCIIx (*Myh1*) and MyHC-emb (*Myh3*) **(A, C)** relative to *cyclophilin A* expression as reference gene in C2C12 cells (n=3) and **(B,F)** relative to *Gapdh gene* expression as reference gene in primary myoblasts isolated from Wt and Lal-/- mice (n=4). **(D)** Representative Western blotting experiment and quantification (n=3) of myosin heavy chain IIx (MyHCIIx) protein expression in C2C12 cells upon treatment with 0.1 µM of Lalistat-2 at the end of differentiation. α-Tubuline (α-tub) was used as loading control. **(E)** Representative images of immunofluorescence staining for MyHCIIx (green) in C2C12 cells differentiated for 6 days. Nuclei are stained with DAPI (blue). Scale bar, 100 µm. **(G)** Representative Western blotting experiment and

quantification (n=4) of MyHCIIx protein expression in primary myoblasts at the end of differentiation. GAPDH was used as loading control. Data represent mean ± SD. *p ≤ 0.05 Unpaired Student's t test.

3.18 Unchanged mitochondrial function in Lalistat-2-treated C2C12 cells

I have already described above that decreased oxidative capacity and ATP concentration in SM of Lal-/- mice correlated with reduced mitochondrial function. In our *in vitro* model of C2C12 cells treated with Lalistat-2, however, I failed to confirm defective mitochondrial functions as evidenced by unchanged oxygen consumption rate (OCR) (Fig. 31A) and extracellular acidification rate (ECAR) (Fig. 31B).

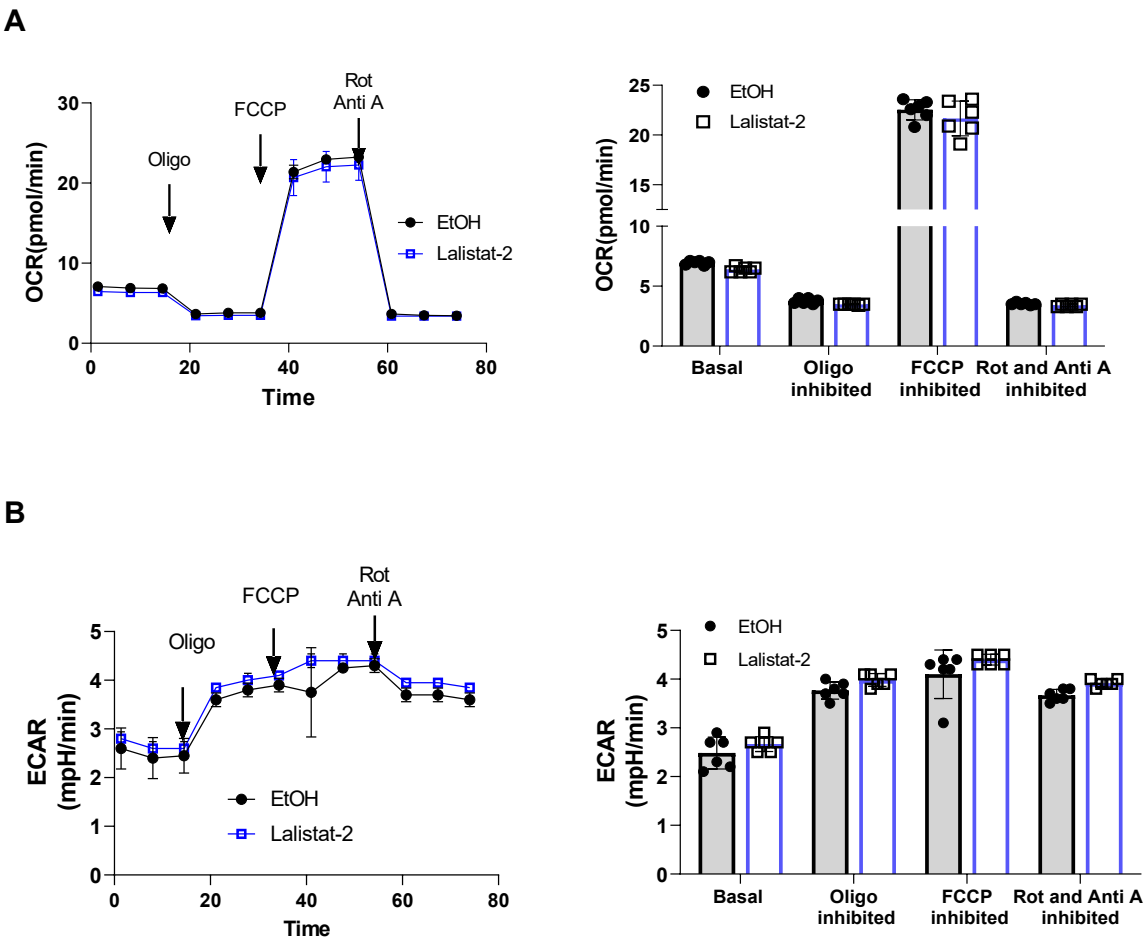

Figure 31: Treatment of C2C12 cells with Lalistat-2 did not affect the functionality of mitochondria.
(A) Oxygen consumption rate (OCR) and **(B)** extracellular acidification rates (ECAR) over time of C2C12 cells treated either with EtOH or Lalistat-2 normalized to the cell number. Arrows indicate the addition of mitochondrial inhibitors (oligomycin (Oligo); FCCP; rotenone (Rot)/antimycin (AntiA)). Data represent mean ± SD. Unpaired Student's t test.

3.19 LAL-D in primary myoblasts does not affect FAO

The experiments using permeabilized muscle fibers from Lal-/- SM revealed reduced mitochondrial FAO and substrate utilization. Unfortunately, I failed to identify any difference in radioactivity captured by the filter paper after the FAO assay in primary myoblasts isolated from Lal-/- or Wt SM (Fig. 32). Thus, both of our *in vitro* models showed no changes in mitochondrial function upon inhibition or loss of LAL activity.

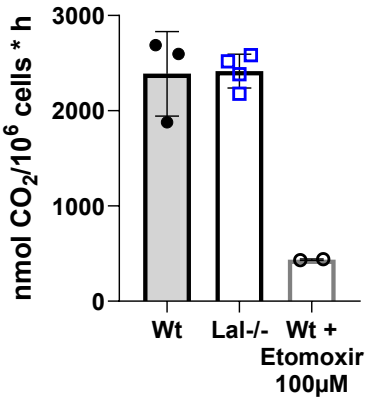

Figure 32: Unaffected fatty acid oxidation in primary myoblasts from Lal-/- mice.
Oxidation of [^{14}C, C-1]palmitate in primary myoblasts isolated from skeletal muscle of Lal-/- and Wt mice (n=3-4). Etomoxir was used as negative control. Data represent mean ± SD. Unpaired Student's t test between Wt and Lal-/- cells.

4. Discussion

The impact of LAL-D on SM pathophysiology is a topic of interest due to the reported characteristic features of decreased muscle size and weakness in LAL-D patients (227, 264-266, 268). The compromised lipid homeostasis in LAL-D, resulting from impaired hepatic and intestinal lipid metabolism, has been associated with improved glucose tolerance, lowered fat mass, decreased blood glucose, and a steady increase in LDL- accompanied by reduced HDL-cholesterol (232, 263, 301, 302). This potentially influences the metabolic state and muscle function. Since SM require a considerable amount of energy to work efficiently, changes in lipid and/or glucose metabolism may influence the metabolic state of the muscle and, consequently, their proper functionality. We, therefore, aimed to characterize SM structure and functions in an animal model of LAL-D. We observed a pronounced increase in the expression of slow-twitch oxidative fibers in SM and, most likely, affected SM functions, resulting from reduced ATP production due to dysfunctional mitochondria and impaired energy metabolism. In addition, the inhibition of LAL activity in C2C12 cells and primary myoblasts resulted in increased lipid accumulation, particularly CE, indicating a role of LAL in lipid metabolism in SM. However, this inhibition had no significant effects on myofiber differentiation or mitochondrial functions, suggesting a minor influence of LAL activity on SM formation. This implies that the changes in SM observed in Lal-/- mice are more likely linked to broader physiological disturbances rather than being a direct result of the lack of LAL in SM.

Myofibers of vertebrate SM differ in contractile properties, mitochondrial density, and metabolic characteristics. Slow-twitch fibers are distinguished by the presence of type I MyHC expression and a high mitochondrial density, which results predominantly in an oxidative metabolism. Fast-twitch fibers express type II MyHCs, which are divided into three subtypes: IIA, IIx or d, and IIB (19). Different SM have a combination of different fibers. For instance, QU, TA, and GA mainly consist of MyHCIIB (fast glycolytic fibers) but in different proportions, whereas SO has a combination of MyHCI and MyHCIIA (26). Due to this fact as well as their role in locomotion, we have chosen these SM types for our studies.

Lal-/- mice display a notable reduction in QU, TA, and GA size, as indicated by decreased muscle weight and diminished CSA and Feret diameter. These findings suggest that the lack of LAL may have an impact on muscle growth in these mice. Nonetheless, it is important to highlight that there is no substantial disparity in SM mass during the early phases of development when compared to Wt mice. However, we have previously shown that impaired lysosomal lipolysis disrupts the balance of cholesterol in the placenta and fetus. This manifests as an early sign of disease pathology within the womb, evidenced by the accumulation of

lysosomal lipids in the liver of Lal-/- fetuses with increases in hepatic lysosomal lipids immediately following birth (222). Interestingly, we found IGFBP5 among the significantly downregulated proteins in both oxidative and glycolytic segments of GA in our proteomics dataset. The expression of *Igfbp5* has already been shown to be reduced during states that induce muscle atrophy in different pathological conditions (303). Moreover, recent studies have suggested a role for IGFBP5 in regulating muscle cell differentiation, which is still controversial (299, 304, 305).

To elucidate whether SM formation is affected in the absence or by inhibiting LAL, conducted experiments with primary cells from Lal-/- mice and with C12C12 cells treated with Lalistat 2. Validation of the specific inhibition of LAL activity at a concentration of 0.1 µM by Lalistat-2 highlighted the importance of optimizing the inhibitor concentration to prevent unintended effects such as inhibition of other lipases (236). We observed that 0.1 µM Lalistat-2 did not affect cell viability or proliferation but significantly reduced acid but not neutral CE and TG hydrolase activities in C2C12 cells, emphasizing its efficacy in targeting LAL. Higher concentrations of Lalistat-2 resulted in drastic inhibition of neutral CE and TG hydrolase activities, confirming our previous results that Lalistat-2 leads to a decrease in neutral lipid hydrolase activities (236). Both *in vitro* models did not reveal any altered expression of key myofiber differentiation markers or the predominant isoform of MyHC, suggesting that loss of LAL does not affect muscle formation. However, the outcome may additionally indicate that the experimental conditions may not have been appropriate for replicating the conditions of the whole-body Lal-/- mouse to disrupt the normal processes of muscle fiber differentiation and maturation.

The loss of SM mass is indeed a primary feature of muscle atrophy, regardless of the cause. MuRF1 (muscle RING-finger protein-1) and Atrogin1, encoded the by *Murf1* and *Atrogin1* genes, respectively, are two muscle-specific ubiquitin ligases that are often upregulated during conditions that promote muscle atrophy, such as denervation, immobilization, fasting, sepsis, and cancer cachexia (180). Chow diet-fed Lal-/- mice use their muscle AA as an extra source of energy being subjected to cold, as seen by increased mRNA expression of these markers (262). However, we assumed that Lal-/- mice already begin to use SM proteins as an alternative energy source at RT. Unexpectedly, we observed even lower expression of *Murf1* and *Atrogin1* in QU, TA, and GA in the fed state and comparable mRNA expression of these markers in 12-h fasted Lal-/- and Wt mice. However, their expression levels can be influenced by various factors, and they may not always be universally upregulated in all forms of muscle atrophy. It is noteworthy that the specific roles and regulation of MuRF1 and Atrogin1 can be complex and their expression is not an absolute indicator of muscle atrophy in every scenario.

Thus, we additionally estimated the proteasomal activity (the system that degrades proteins) and surprisingly found that it was reduced in some cases, raising doubt on the hypothesis that muscle wasting is responsible for smaller muscle size and mass in Lal-/- mice.

Plasma AA could be used as building blocks or substrates for the synthesis or remodeling of muscle proteins. The concentrations of glucogenic AA, which were expected to be increased in the circulation during starvation by muscle proteolysis (306), were unchanged in Lal-/- compared to respective Wt mice, or even reduced (Gln). However, the concentration of Gln, an important AA produced by SM, was also reduced in GA from Lal-/- mice. It plays a crucial role in nitrogen transport, acid-base balance in the blood, and it participates in TCA cycle supplementation (307), which potentially takes place in SM and liver due to the altered metabolic conditions of Lal-/- mice (263). Moreover, Gln serves as an essential energy source for enterocytes, which utilize it at a high rate for various functions, such as fueling the Krebs cycle, supporting cell proliferation, and maintaining the intestinal barrier function (308). Lal-/- also exhibit a pronounced intestinal phenotype, however, only in systemic but not enterocyte-specific knockout mice (259) .

Ala release from SM is associated with the glucose-alanine cycle (309, 310), which involves the transamination of pyruvate to Ala by the enzyme alanine aminotransferase (ALT), using an amino group from another AA, often Glu. This newly synthesized Ala can then be transported to the liver, where it is converted back to pyruvate and used in gluconeogenesis to form glucose. Interestingly, increased levels of ALT and aspartate aminotransferase (AST) are important clinical markers for CESD patients (218) and can be used to distinguish LAL-D from FH. Reduced Ala concentration found in Lal-/- GA can be caused by the affected synthesis of Ala, which reflects broader metabolic processes and is not due to the breakdown of specific storage proteins with high Ala content.

The decline in Gly levels within SM could arise from various factors. Observations from mouse models of diabetes and muscular dystrophy, as well as from studies conducted on the elderly, suggest a propensity for reduced SM Gly levels associated with these conditions (311-313). Nevertheless, Gly serves not only as a fundamental building block for protein synthesis but also participates in other crucial physiological processes. Gly contributes to the synthesis of creatine, which plays a pivotal role in the storage and provisioning of energy within muscle cells during high-intensity activities (314), thus potentially exerting an important role in supporting the energy equilibrium in Lal-/- SM.

Additionally, we found elevated concentrations of the BCAA Leu, Ile, and Val in plasma from fasted Lal-/- mice. BCAA play significant roles in muscle cell metabolism by facilitating the translocation of the glucose transporters GLUT1 and GLUT4 to the cell surface, thereby

enhancing glucose uptake into the muscle cells (315). In addition to aiding glucose metabolism, these AA contribute CoA intermediates such as acetyl-CoA and succinyl-CoA to the TCA cycle, supporting the cellular process of energy production (316). However, studies have indicated that BCAA, are significant biomarkers for metabolic diseases. Elevated levels of BCAAs have been observed in individuals with obesity, insulin resistance, type 2 diabetes (317) and, most importantly, with liver pathologies such as non-alcoholic fatty liver disease (318). Therefore, it remains elusive whether the elevated circulating levels of BCAAs in Lal-/- mice are attributable to their pronounced liver damage or their involvement in SM metabolic demands.

One of the most important signaling pathways controlling protein production in SM is the PI3K/Akt/mTOR pathway. Akt phosphorylates and activates mTOR kinase, which in turn phosphorylates downstream targets such as 4e-BP1, thereby promoting translation and protein synthesis (287-289). The data of protein expression in Lal-/- SM indicate that there were no significant changes in the phosphorylation states of Akt and 4E-BP1 relative to their total protein levels. This suggests that the IGF-1/Akt/mTOR pathway, which is vital for muscle protein synthesis and cell growth, was not altered in Lal-/- mice. AMPK also plays a multifaceted role in SM metabolism. It acts as an energy sensor responding to changes in ATP levels inside of a cell (319). However, despite decreased ATP content in QU, the overall expression of AMPK subunits was reduced in Lal-/- QU and GA. AMPK also affects protein synthesis in SM. By inhibiting the mTORC1 signaling pathway, activated AMPK can decrease the rate of protein synthesis. This effect is typically seen during energy stress as an attempt to conserve energy, which contrasts with the growth-promoting activity of the IGF-1/Akt/mTOR pathway (290). Conversely, our mouse model showed decreased AMPK levels and unchanged expression of Akt and mTOR, indicating the presence of another mechanism that may affect protein synthesis in SM in Lal-/- mice. Despite unchanged expression of these markers, the observation that translation as one of the most downregulated Reactome terms in red muscle fibers suggests the presence of underlying regulatory issues affecting protein synthesis that are not directly revealed by these markers. The nuclear factor kappa B (NF-κB) pathway might play a role in these regulatory processes (289). NF-κB is a transcription factor that is typically associated with the immune response and inflammation. It is activated by a variety of proinflammatory cytokines, such as TNF-α, IL-1, and IL-6 (320). The link between the NF-κB pathway and alterations in protein synthesis in muscle fibers may not be direct. However, systemic inflammation, as evidenced by elevated levels of MCP1 and macrophage infiltration in Lal-/- mice, may be correlated with NF-κB activation (321).

Furthermore, the downregulated GOBP terms and protein interaction network generated by Cytoscape confirmed impaired protein folding in both oxidative and glycolytic segments of GA from Lal-/- mice. Molecular chaperones, such as heat shock proteins (HSP) and protein disulfide isomerases (PDI), play essential roles in assisting protein folding and maintaining protein homeostasis (proteostasis) (322). A deficiency in these chaperones, as indicated by significant downregulation, could lead to protein misfolding and aggregation and contribute to cellular stress and potential muscle dysfunction (323). While a direct link between reduced expression of chaperones and low muscle mass has not yet been established, it is reasonable to suspect that impaired protein folding could negatively affect SM integrity and thus the mass. Alterations in muscle size might correspond to a transition in muscle fiber type, particularly as slow-twitch (oxidative) fibers generally have a smaller CSA than fast-twitch (glycolytic) fibers. This relationship contributes to what is referred to as the "muscle fiber type – fiber size paradox" (324). In Lal-/- mice, an increase in the expression of genes and proteins associated with slow-twitch oxidative fibers, such as MyHCI (MYH7), TNNC1, and TNNI1, confirmed by proteomics data, qPCR, western blotting, and immunofluorescence staining, indicates a shift toward type I myofibers. However, the precise mechanisms leading to this upregulation of type I fiber-specific proteins in SM of Lal-/- mice remain to be elucidated. Furthermore, muscles with fast-twitch glycolytic fibers are known to be more sensitive than slow-twitch oxidative fibers under a range of atrophic conditions (180). Thus, this might be a possible adaptation mechanism to changes in whole-body energy metabolism, as slow fibers work sufficiently but with lower power utilization and consume less ATP than fast fibers (325).

SM is a highly active tissue that demands substantial energy, making it sensitive to disturbances in metabolism. Previous research on Lal-/- mice revealed that these mice when subjected to cold temperatures exhibited disruption in FA metabolism in SM (262). However, more importantly, Lal-/- mice kept at RT showed changes in metabolite concentrations (263). LAL-D results in the pathological accumulation of lipids, such as CE and TGs, within hepatic lysosomes, leading to liver dysfunction and a progressive loss of WAT (256, 263, 295). This loss of WAT in Lal-/- mice necessitates metabolic adaptations. Moreover, in the liver of Lal-/- mice, the inability to adequately hydrolyze CE and TG leads to a decreased flux of FA and a subsequent reduction in hepatic acyl-CoA, which is crucial for the synthesis of very low-density lipoproteins (263) and thus manifests in lower plasma TG levels. As a compensatory response to this energy crisis, these mice exhibit metabolic adaptations that increase systemic glucose utilization. These adaptations have been observed through intraperitoneal glucose tolerance tests and insulin tolerance tests, revealing that Lal-/- mice display improved glucose tolerance and heightened insulin sensitivity (263). Plasma glucose levels are reduced in these mice as

well as decreased hepatic glucose content and glycogen stores, along with diminished liver concentrations of Glu (263). As shown before (263), Lal-/- SM increases glucose clearance to compensate for a potential energy deficit. The increased glucose and glycogen contents in GA of Lal-/- mice support the notion that these mice compensate for the deficiency in lipid metabolism by triggering glucose storage and its utilization. Although the concentration of succinate was decreased in Lal-/- mice, unchanged concentrations of fumarate do not clearly point to an impairment of the TCA cycle as a whole.

The observed reduction in choline levels in Lal-/- SM can have significant implications for muscle function and metabolism, including SM atrophy and altered lipid metabolism (326, 327). Moreover, carnosine, a histidine-containing dipeptide, is abundant in SM and is involved in muscle buffering, protection against oxidative stress, and muscle contraction (328, 329). Thus, the reduced levels of choline and carnosine in Lal-/- SM can considerably impact muscle health and activity.

The formation and accumulation of fat-laden lysosomes and cholesterol (or CE) crystals in non-adipose tissues were described in various organs of Lal-/- mice (222, 256, 258, 259). Whole-body LAL-D in mice results in the abnormal storage of lipids across different SM as well, including a marked increase in CE specifically in GA when the mice are fed chow diet. Fasting led to a notable reduction in TG levels in Lal-/- muscles such as QU, indicating altered lipid metabolism. These findings highlight the variability of lipid accumulation in SM and the dynamic changes in lipid content in response to the metabolic state in Lal-/- mice, reflecting the impact of enzyme deficiency on lipid handling in muscle tissue. Interestingly, Lal-/- rats showed accumulation of “lipid droplets” in the subsarcolemmal space of muscles fibers (330). However, despite altered lipid content, we were unable to detect lipid accumulation in SM of Lal-/- mice. Estimation of lipids in Lalistat-2 treated cells as well as in primary myoblasts from Lal-/- mice revealed CE accumulation in both cell types. Thus, the obtained data hint to an important role of LAL in SM cholesterol metabolism. Surprisingly, Lal-/- mice on a HFHC diet show significant changes in SM mass and lipid profile that are comparable to that of older Lal-/- mice fed a standard chow diet.

Reduced acyl-carnitine concentrations in QU, TA, and GA from 12-h fasted mice could be a consequence of the failure of Lal-/- mice to enhance circulating TG concentrations during fasting together with elevated TC (independently of the feeding status), which we have shown earlier (263). However, reduced acyl-carnitines may be a sign of mitochondrial dysfunction in Lal-/- SM. Cholesterol accumulation in Lal-/- SM could potentially affect the mitochondria, characterized by impaired respiration and lower ATP production (331, 332). This connection between excess cholesterol and mitochondrial health suggests that the disrupted lipid

metabolism associated with LAL-D could have downstream effects on cellular energy generation. Despite an increased number of oxidative fibers in Lal-/- mice, which would usually indicate a higher mitochondrial count and improved cellular respiration, these mice actually showed reduced ability of SM to produce energy through the process of oxidative phosphorylation. The quantity and structure of mitochondria appeared unaffected, but proteomic analysis revealed that functions related to energy-generating processes in the mitochondria were compromised. Proteins essential for the electron transport chain and ATP synthesis, specifically complex I, II, III, and V proteins such as NDUF, SDH, UQCR, and ATP5 family members, were found to be diminished. These proteins are known to be decreased in muscles affected by sarcopenia (age-related SM loss) (333). Among the proteins that were significantly reduced in SM of Lal-/- mice, MUP isoforms were found in both oxidative and glycolytic fibers in dissected GA. SM is known to be one of the key tissues metabolically affected by low expression of MUP1, which was observed in models of obesity or diabetes. In comparison, elevated *Mup* gene expression was related to improved mitochondrial biogenesis and oxidative phosphorylation primarily in SM (334). Hence, potentially different isoforms of *Mup* could play a role in SM metabolism and somehow affect mitochondrial functionality in Lal-/- mice but this remains to be elucidated in further studies.

In contrast to the findings in Lal-/- mice in which we observed reduced FAO and oxidative phosphorylation, we failed to recapitulate the findings on mitochondria function in both of our *in vitro* cell models. The differences we observed between *in vivo* and *in vitro/ex vivo* models might be a consequence of the inaccessibility of lipids in Lal-/- mice, the absence of white adipose tissue, and the rapid glucose consumption in a variety of tissues in mice (256, 262, 263), whereas cells normally grow in a complete glucose-rich environment. Moreover, systemic inflammation profoundly influences the SM phenotype as evidenced in various pathological conditions such as cachexia (335-337), diabetes (338, 339) or chronic obstructive pulmonary disease (340, 341). The consistent elevation of pro-inflammatory cytokines and the substantial presence of macrophages in multiple organs indicate systemic inflammation in Lal-/- mice, a phenomenon that is challenging to be replicated in cell culture experiments. It is noteworthy that local inflammation was not detected in SM of Lal-/- mice.

The increased GLNA expression but decreased glutamine (Gln) concentration in SM may have significant implications for metabolic homeostasis and muscle function. GLNA (Gln synthetase) plays a crucial role in the synthesis of the essential amino acid Gln, which is involved in various metabolic processes (72). The observed increase in GLNA suggests the upregulation of Gln synthesis pathways. However, the decreased levels of Gln may indicate enhanced utilization or altered metabolic flux of Gln in SM and maybe even in the liver as discussed above.

The comparable performance during the hanging wire test suggested that the strength, coordination, and stamina are not affected in SM of Lal-/- mice, indicating no sign of neuromuscular and motor impairment in our knockout mouse model. Interestingly, muscle contraction was highlighted as one of the clusters in the Cytoscape protein interaction network with the majority of upregulated proteins. However, compared to controls, increased exhaustion in the treadmill peak effort testing was confirmed for Lal-/- mice. These functional deficits may be explained in part by the affected mitochondrial functions described above. Another important finding points at the impaired whole-body energy metabolism in Lal-/- mice (263), which may also influence exercise performance. Decreased expression of IGFBP5 has been reported in cases where muscles are denervated or subjected to unloading, a condition that fits the reduced locomotor activity and physical performance in Lal-/- mice. This aligns with the well-established opinion that the changes in muscle use, such as those induced by reduced movement or external loading, can impact the expression of proteins related to muscle growth and maintenance (342). It should be noted that no cardiac abnormalities have been reported in Lal-/- mice and it still remains unclear if the pathophysiological characteristics observed in the lungs of Lal-/- mice (261) influence their physical capabilities. The observed disparities in metabolites such as creatine or amino acids in trained mice may further validate the notion that energy metabolism is altered in SM of Lal-/- mice. Under stress conditions, these mice appear to attempt to mobilize all available resources to adequately support ATP production.

5. Summary and conclusion.

To sum up, our data provide conclusive evidence that the whole-body loss of LAL affects the phenotype, and most probably, the functions of SM due to insufficient ATP production associated with dysfunctional mitochondria and impaired energy metabolism. The described alterations result in increased expression of slow oxidative fibers in SM of Lal-/- mice. Experiments on the cell models, together with inhibition of LAL activity, confirm that the observed alterations in whole-body Lal-/- mice are the result of systemic loss of the respective enzyme, which mainly affects liver, small intestine, adipose tissue, and macrophages and thus causes systemic inflammation. Overall, although LAL plays an essential role in lipid metabolism of SM, it has only a minor impact on the processes involved in muscle differentiation and cellular energy production.

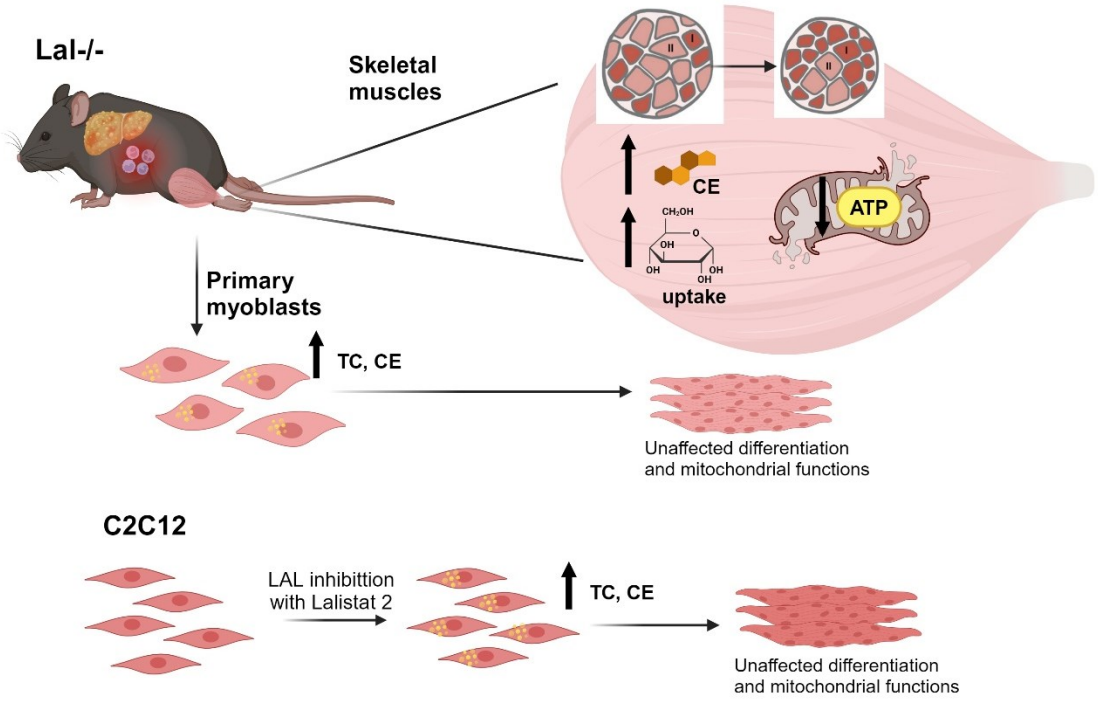

Figure 33 Graphical summary depicting the consequences of loss or inhibition of lysosomal acid lipase (LAL) across *in vivo*, *ex vivo*, and *in vitro* models.
Skeletal muscles (SM) from Lal-/- mice display elevated cholesteryl ester (CE) content and increased glucose uptake, accompanied by upregulation of proteins specific to oxidative slow (type I) fibers. However, mitochondrial function in the SM studied was diminished. The loss of LAL similarly impacted lipid content both *in vitro* and *ex vivo*. Interestingly, differentiation and mitochondrial functions remained unchanged in Lalistat-2-treated C2C12 cells and primary myoblasts isolated from Lal-/- mice. Created with Biorender.com.

6. References

1. Frontera WR, Ochala J. Skeletal muscle: a brief review of structure and function. Calcif Tissue Int. 2015;96(3):183-95.
2. Spirduso WW, Francis KL, MacRae PG. Physical dimensions of aging. 2nd ed. Champaign, Ill. ; Leeds: Human Kinetics; 2005. ix, 374 p. : ill p.
3. Celichowski J, Drzymala-Celichowska H. The number of motor units in the medial gastrocnemius muscle of male and female rats. J Physiol Pharmacol. 2007;58(4):821-8.
4. Huxley H, Hanson J. Changes in the Cross-Striations of Muscle during Contraction and Stretch and Their Structural Interpretation. Nature. 1954;173(4412):973-6.
5. Huxley HE. Fifty years of muscle and the sliding filament hypothesis. Eur J Biochem. 2004;271(8):1403-15.
6. Granger BL, Lazarides E. Desmin and Vimentin Coexist at the Periphery of the Myofibril Z-Disc. Cell. 1979;18(4):1053-63.
7. Hoh JFY. Developmental, physiologic and phylogenetic perspectives on the expression and regulation of myosin heavy chains in mammalian skeletal muscles. J Comp Physiol B. 2023;193(4):355-82.
8. Aguilar HN, Mitchell BF. Physiological pathways and molecular mechanisms regulating uterine contractility. Hum Reprod Update. 2010;16(6):725-44.
9. Houdusse A, Sweeney HL. How Myosin Generates Force on Actin Filaments. Trends Biochem Sci. 2016;41(12):989-97.
10. Huxley AF. Muscle structure and theories of contraction. Prog Biophys Biophys Chem. 1957;7:255-318.
11. Squire J. Special Issue: The Actin-Myosin Interaction in Muscle: Background and Overview. Int J Mol Sci. 2019;20(22).
12. Hartman MA, Spudich JA. The myosin superfamily at a glance. J Cell Sci. 2012;125(Pt 7):1627-32.
13. Shenkman BS. From Slow to Fast: Hypogravity-Induced Remodeling of Muscle Fiber Myosin Phenotype. Acta Naturae. 2016;8(4):47-59.
14. Needham DM. Red and white muscle. Physiological Reviews. 1926;6(1):1-27.
15. Pette D, Staron RS. Myosin isoforms, muscle fiber types, and transitions. Microsc Res Tech. 2000;50(6):500-9.
16. Lowry CV, Kimmey JS, Felder S, Chi MM, Kaiser KK, Passonneau PN, et al. Enzyme patterns in single human muscle fibers. J Biol Chem. 1978;253(22):8269-77.

17. Pette D, Staron RS. Cellular and molecular diversities of mammalian skeletal muscle fibers. Rev Physiol Biochem Pharmacol. 1990;116:1-76.
18. Allen DG, Westerblad H. Role of phosphate and calcium stores in muscle fatigue. J Physiol. 2001;536(Pt 3):657-65.
19. Schiaffino S, Reggiani C. Fiber types in Mammalian skeletal muscles. Physiological Reviews. 2011;91(4):1447-531.
20. Murgia M, Nagaraj N, Deshmukh AS, Zeiler M, Cancellara P, Moretti I, et al. Single muscle fiber proteomics reveals unexpected mitochondrial specialization. EMBO Rep. 2015;16(3):387-95.
21. Schiaffino S, Reggiani C, Kostrominova TY, Mann M, Murgia M. Mitochondrial specialization revealed by single muscle fiber proteomics: focus on the Krebs cycle. Scand J Med Sci Sports. 2015;25 Suppl 4:41-8.
22. Mori K. Maintenance of Skeletal Muscle to Counteract Sarcopenia in Patients with Advanced Chronic Kidney Disease and Especially Those Undergoing Hemodialysis. Nutrients. 2021;13(5).
23. Staron RS, Pette D. The continuum of pure and hybrid myosin heavy chain-based fibre types in rat skeletal muscle. Histochemistry. 1993;100(2):149-53.
24. Biering-Sorensen B, Kristensen IB, Kjaer M, Biering-Sorensen F. Muscle after spinal cord injury. Muscle Nerve. 2009;40(4):499-519.
25. Armstrong RB, Phelps RO. Muscle fiber type composition of the rat hindlimb. Am J Anat. 1984;171(3):259-72.
26. Augusto V, Padovani CR, Eduardo G, Campos R. Skeletal muscle fiber types in C57BL6J mice 2004;21:89-94.
27. Salmons S, Vrbova G. The influence of activity on some contractile characteristics of mammalian fast and slow muscles. J Physiol. 1969;201(3):535-49.
28. Lomo T, Westgaard RH, Dahl HA. Contractile properties of muscle: control by pattern of muscle activity in the rat. Proc R Soc Lond B Biol Sci. 1974;187(1086):99-103.
29. Pette D, Staron RS. Mammalian skeletal muscle fiber type transitions. Int Rev Cytol. 1997;170:143-223.
30. Pattullo MC, Cotter MA, Cameron NE, Barry JA. Effects of lengthened immobilization on functional and histochemical properties of rabbit tibialis anterior muscle. Exp Physiol. 1992;77(3):433-42.
31. Ianuzzo D, Patel P, Chen V, O'Brien P, Williams C. Thyroidal trophic influence on skeletal muscle myosin. Nature. 1977;270(5632):74-6.

32. Fitts RH, Winder WW, Brooke MH, Kaiser KK, Holloszy JO. Contractile, biochemical, and histochemical properties of thyrotoxic rat soleus muscle. Am J Physiol. 1980;238(1):C14-20.
33. Nwoye L, Mommaerts WF. The effects of thyroid status on some properties of rat fast-twitch muscle. J Muscle Res Cell Motil. 1981;2(3):307-20.
34. Gutmann E, Hanzlikova V, Lojda Z. Effect of androgens on histochemical fibre type. Differentiation in the temporal muscle of the guinea pig. Histochemie. 1970;24(4):287-91.
35. Lyons GE, Kelly AM, Rubinstein NA. Testosterone-induced changes in contractile protein isoforms in the sexually dimorphic temporalis muscle of the guinea pig. J Biol Chem. 1986;261(28):13278-84.
36. Catz DS, Fischer LM, Kelley DB. Androgen regulation of a laryngeal-specific myosin heavy chain mRNA isoform whose expression is sexually differentiated. Dev Biol. 1995;171(2):448-57.
37. English AW, Eason J, Schwartz G, Shirley A, Carrasco DI. Sexual dimorphism in the rabbit masseter muscle: myosin heavy chain composition of neuromuscular compartments. Cells Tissues Organs. 1999;164(4):179-91.
38. Hanzlikova V, Schiaffino S, Settembrini P. Histochemical fiber types characteristics in the normal and the persistent levator ani muscle of the rat. Histochemie. 1970;22(1):45-50.
39. Joubert Y, Tobin C, Lebart MC. Testosterone-induced masculinization of the rat levator ani muscle during puberty. Dev Biol. 1994;162(1):104-10.
40. Kadi F. Cellular and molecular mechanisms responsible for the action of testosterone on human skeletal muscle. A basis for illegal performance enhancement. Br J Pharmacol. 2008;154(3):522-8.
41. White JP, Gao S, Puppa MJ, Sato S, Welle SL, Carson JA. Testosterone regulation of Akt/mTORC1/FoxO3a signaling in skeletal muscle. Mol Cell Endocrinol. 2013;365(2):174-86.
42. Larsson L, Ansved T. Effects of ageing on the motor unit. Prog Neurobiol. 1995;45(5):397-458.
43. Ciciliot S, Rossi AC, Dyar KA, Blaauw B, Schiaffino S. Muscle type and fiber type specificity in muscle wasting. Int J Biochem Cell Biol. 2013;45(10):2191-9.
44. Miljkovic N, Lim JY, Miljkovic I, Frontera WR. Aging of skeletal muscle fibers. Ann Rehabil Med. 2015;39(2):155-62.
45. Li JB, Goldberg AL. Effects of food deprivation on protein synthesis and degradation in rat skeletal muscles. Am J Physiol. 1976;231(2):441-8.
46. Armstrong RB, Gollnick PD, Ianuzzo CD. Histochemical properties of skeletal muscle fibers in streptozotocin-diabetic rats. Cell Tissue Res. 1975;162(3):387-94.

47. Tiao G, Lieberman M, Fischer JE, Hasselgren PO. Intracellular regulation of protein degradation during sepsis is different in fast- and slow-twitch muscle. Am J Physiol. 1997;272(3 Pt 2):R849-56.
48. Acharyya S, Butchbach ME, Sahenk Z, Wang H, Saji M, Carathers M, et al. Dystrophin glycoprotein complex dysfunction: a regulatory link between muscular dystrophy and cancer cachexia. Cancer Cell. 2005;8(5):421-32.
49. Serrano AL, Jardi M, Suelves M, Klotman PE, Munoz-Canoves P. HIV-1 transgenic expression in mice induces selective atrophy of fast-glycolytic skeletal muscle fibers. Front Biosci. 2008;13:2797-805.
50. Grimby G, Broberg C, Krotkiewska I, Krotkiewski M. Muscle fiber composition in patients with traumatic cord lesion. Scand J Rehabil Med. 1976;8(1):37-42.
51. Herbison GJ, Jaweed MM, Ditunno JF. Muscle atrophy in rats following denervation, casting, inflammation, and tenotomy. Arch Phys Med Rehabil. 1979;60(9):401-4.
52. Jo YS. Long-Term Outcome of Chronic Obstructive Pulmonary Disease: A Review. Tuberc Respir Dis (Seoul). 2022;85(4):289-301.
53. Gambara G, Salanova M, Ciciliot S, Furlan S, Gutsmann M, Schiffl G, et al. Gene Expression Profiling in Slow-Type Calf Soleus Muscle of 30 Days Space-Flown Mice. PLoS One. 2017;12(1):e0169314.
54. Campione M, Ausoni S, Guezennec CY, Schiaffino S. Myosin and troponin changes in rat soleus muscle after hindlimb suspension. J Appl Physiol (1985). 1993;74(3):1156-60.
55. Dutchak PA, Estill-Terpack SJ, Plec AA, Zhao X, Yang C, Chen J, et al. Loss of a Negative Regulator of mTORC1 Induces Aerobic Glycolysis and Altered Fiber Composition in Skeletal Muscle. Cell Rep. 2018;23(7):1907-14.
56. Baylor SM, Hollingworth S. Sarcoplasmic reticulum calcium release compared in slow-twitch and fast-twitch fibres of mouse muscle. J Physiol. 2003;551(Pt 1):125-38.
57. Shen T, Liu Y, Contreras M, Hernandez-Ochoa EO, Randall WR, Schneider MF. DNA binding sites target nuclear NFATc1 to heterochromatin regions in adult skeletal muscle fibers. Histochem Cell Biol. 2010;134(4):387-402.
58. Schiaffino S. Fibre types in skeletal muscle: a personal account. Acta Physiol (Oxf). 2010;199(4):451-63.
59. Frey N, Frank D, Lippl S, Kuhn C, Kogler H, Barrientos T, et al. Calsarcin-2 deficiency increases exercise capacity in mice through calcineurin/NFAT activation. J Clin Invest. 2008;118(11):3598-608.

60. Rasbach KA, Gupta RK, Ruas JL, Wu J, Naseri E, Estall JL, Spiegelman BM. PGC-1alpha regulates a HIF2alpha-dependent switch in skeletal muscle fiber types. Proc Natl Acad Sci U S A. 2010;107(50):21866-71.
61. Winbanks CE, Chen JL, Qian HW, Liu YY, Bernardo BC, Beyer C, et al. The bone morphogenetic protein axis is a positive regulator of skeletal muscle mass. Journal of Cell Biology. 2013;203(2):345-57.
62. Yuan YA, Shi XE, Liu YG, Yang GS. FoxO1 regulates muscle fiber-type specification and inhibits calcineurin signaling during C2C12 myoblast differentiation. Mol Cell Biochem. 2011;348(1-2):77-87.
63. Azad M, Khaledi N, Hedayati M. Effect of acute and chronic eccentric exercise on FOXO1 mRNA expression as fiber type transition factor in rat skeletal muscles. Gene. 2016;584(2):180-4.
64. Shi XE, Song ZY, Yang QM, Liu YG, Yang GS. Correlation of forkhead box transcription factor O1 and myosin heavy chain isoforms in porcine skeletal muscle. Genet Mol Res. 2014;13(4):10231-40.
65. Xu M, Chen XL, Chen DW, Yu B, Huang ZQ. FoxO1: a novel insight into its molecular mechanisms in the regulation of skeletal muscle differentiation and fiber type specification. Oncotarget. 2017;8(6):10662-74.
66. van Rooij E, Quiat D, Johnson BA, Sutherland LB, Qi X, Richardson JA, et al. A family of microRNAs encoded by myosin genes governs myosin expression and muscle performance. Dev Cell. 2009;17(5):662-73.
67. Rossi AC, Mammucari C, Argentini C, Reggiani C, Schiaffino S. Two novel/ancient myosins in mammalian skeletal muscles: MYH14/7b and MYH15 are expressed in extraocular muscles and muscle spindles. J Physiol. 2010;588(Pt 2):353-64.
68. Jia HX, Zhao YX, Li TT, Zhang Y, Zhu DH. miR-30e is negatively regulated by myostatin in skeletal muscle and is functionally related to fiber-type composition. Acta Bioch Bioph Sin. 2017;49(5):392-9.
69. Spriet LL. Anaerobic metabolism in human skeletal muscle during short-term, intense activity. Can J Physiol Pharmacol. 1992;70(1):157-65.
70. Sahlin K. Muscle energetics during explosive activities and potential effects of nutrition and training. Sports Med. 2014;44 Suppl 2(Suppl 2):S167-73.
71. Hargreaves M, Spriet LL. Skeletal muscle energy metabolism during exercise. Nature Metabolism. 2020;2(9):817-28.
72. Nelson DL, Hoskins AA, Cox MM, Lehninger AL. Lehninger principles of biochemistry. 8th edition; international edition. ed. Austin: Macmillan Learning; 2021.

73. Medbo JI, Tabata I. Anaerobic energy release in working muscle during 30 s to 3 min of exhausting bicycling. J Appl Physiol (1985). 1993;75(4):1654-60.
74. Parolin ML, Chesley A, Matsos MP, Spriet LL, Jones NL, Heigenhauser GJ. Regulation of skeletal muscle glycogen phosphorylase and PDH during maximal intermittent exercise. Am J Physiol. 1999;277(5):E890-900.
75. Krogh A, Lindhard J, Liljestrand G, Andresen KG. The relative value of fat and carbohydrate as sources of muscular energy. With appendices on the correlation between standard metabolism and the respiratory quotient during rest and work. Biochem J. 1920;14(3-4):290-363.
76. Thiebaud D, Jacot E, Defronzo RA, Maeder E, Jequier E, Felber JP. The Effect of Graded Doses of Insulin on Total Glucose-Uptake, Glucose-Oxidation, and Glucose Storage in Man. Diabetes. 1982;31(11):957-63.
77. Ferrannini E, Simonson DC, Katz LD, Reichard G, Bevilacqua S, Barrett EJ, et al. The Disposal of an Oral Glucose-Load in Patients with Non-Insulin-Dependent Diabetes. Metabolism. 1988;37(1):79-85.
78. DeFronzo RA, Tripathy D. Skeletal Muscle Insulin Resistance Is the Primary Defect in Type 2 Diabetes. Diabetes Care. 2009;32:S157-S63.
79. Mueckler M, Thorens B. The SLC2 (GLUT) family of membrane transporters. Mol Aspects Med. 2013;34(2-3):121-38.
80. Klip A, Volchuk A, He LJ, Tsakiridis T. The glucose transporters of skeletal muscle. Semin Cell Dev Biol. 1996;7(2):229-37.
81. Merz KE, Thurmond DC. Role of Skeletal Muscle in Insulin Resistance and Glucose Uptake. Compr Physiol. 2020;10(3):785-809.
82. Hundal HS, Ahmed A, Guma A, Mitsumoto Y, Marette A, Rennie MJ, Klip A. Biochemical and immunocytochemical localization of the 'GLUT5 glucose transporter' in human skeletal muscle. Biochem J. 1992;286 (Pt 2)(Pt 2):339-43.
83. Granchi C, Bertini S, Macchia M, Minutolo F. Inhibitors of Lactate Dehydrogenase Isoforms and their Therapeutic Potentials. Curr Med Chem. 2010;17(7):672-97.
84. Lee TY. Lactate: a multifunctional signaling molecule. Yeungnam Univ J Med. 2021;38(3):183-93.
85. Li X, Yang Y, Zhang B, Lin X, Fu X, An Y, et al. Correction: Lactate metabolism in human health and disease. Signal Transduct Target Ther. 2022;7(1):372.
86. Hotamisligil GS, Bernlohr DA. Metabolic functions of FABPs--mechanisms and therapeutic implications. Nat Rev Endocrinol. 2015;11(10):592-605.

87. Kazantzis M, Stahl A. Fatty acid transport proteins, implications in physiology and disease. Biochim Biophys Acta. 2012;1821(5):852-7.
88. Jain SS, Luiken JJ, Snook LA, Han XX, Holloway GP, Glatz JF, Bonen A. Fatty acid transport and transporters in muscle are critically regulated by Akt2. FEBS Lett. 2015;589(19 Pt B):2769-75.
89. Morales PE, Bucarey JL, Espinosa A. Muscle lipid metabolism: Role of lipid droplets and perilipins. Journal of Diabetes Research. 2017;2017.
90. Luiken JJ, Miskovic D, Arumugam Y, Glatz JF, Bonen A. Skeletal muscle fatty acid transport and transporters. Int J Sport Nutr Exerc Metab. 2001;11 Suppl:S92-6.
91. Glatz JF, Schaap FG, Binas B, Bonen A, van der Vusse GJ, Luiken JJ. Cytoplasmic fatty acid-binding protein facilitates fatty acid utilization by skeletal muscle. Acta Physiol Scand. 2003;178(4):367-71.
92. Coort SL, Coumans WA, Bonen A, van der Vusse GJ, Glatz JF, Luiken JJ. Divergent effects of rosiglitazone on protein-mediated fatty acid uptake in adipose and in muscle tissues of Zucker rats. J Lipid Res. 2005;46(6):1295-302.
93. Fischer H, Gustafsson T, Sundberg CJ, Norrbom J, Ekman M, Johansson O, Jansson E. Fatty acid binding protein 4 in human skeletal muscle. Biochem Biophys Res Commun. 2006;346(1):125-30.
94. Jeppesen J, Albers PH, Rose AJ, Birk JB, Schjerling P, Dzamko N, et al. Contraction-induced skeletal muscle FAT/CD36 trafficking and FA uptake is AMPK independent. J Lipid Res. 2011;52(4):699-711.
95. Bonen A, Jain SS, Snook LA, Han XX, Yoshida Y, Buddo KH, et al. Extremely rapid increase in fatty acid transport and intramyocellular lipid accumulation but markedly delayed insulin resistance after high fat feeding in rats. Diabetologia. 2015;58(10):2381-91.
96. Jacob S, Machann J, Rett K, Brechtel K, Volk A, Renn W, et al. Association of increased intramyocellular lipid content with insulin resistance in lean nondiabetic offspring of type 2 diabetic subjects. Diabetes. 1999;48(5):1113-9.
97. Brons C, Grunnet LG. Mechanisms in endocrinologY: Skeletal muscle lipotoxicity in insulin resistance and type 2 diabetes: a causal mechanism or an innocent bystander? Eur J Endocrinol. 2017;176(2):R67-R78.
98. Brioche T, Pagano AF, Py G, Chopard A. Muscle wasting and aging: Experimental models, fatty infiltrations, and prevention. Mol Aspects Med. 2016;50:56-87.
99. Hoeg L, Roepstorff C, Thiele M, Richter EA, Wojtaszewski JF, Kiens B. Higher intramuscular triacylglycerol in women does not impair insulin sensitivity and proximal insulin signaling. J Appl Physiol (1985). 2009;107(3):824-31.

100. van Loon LJ, Koopman R, Manders R, van der Weegen W, van Kranenburg GP, Keizer HA. Intramyocellular lipid content in type 2 diabetes patients compared with overweight sedentary men and highly trained endurance athletes. Am J Physiol Endocrinol Metab. 2004;287(3):E558-65.
101. Dube JJ, Amati F, Stefanovic-Racic M, Toledo FG, Sauers SE, Goodpaster BH. Exercise-induced alterations in intramyocellular lipids and insulin resistance: the athlete's paradox revisited. Am J Physiol Endocrinol Metab. 2008;294(5):E882-8.
102. Yu C, Chen Y, Cline GW, Zhang D, Zong H, Wang Y, et al. Mechanism by which fatty acids inhibit insulin activation of insulin receptor substrate-1 (IRS-1)-associated phosphatidylinositol 3-kinase activity in muscle. J Biol Chem. 2002;277(52):50230-6.
103. Itani SI, Ruderman NB, Schmieder F, Boden G. Lipid-induced insulin resistance in human muscle is associated with changes in diacylglycerol, protein kinase C, and IκB-α. Diabetes. 2002;51(7):2005-11.
104. Chavez JA, Summers SA. Characterizing the effects of saturated fatty acids on insulin signaling and ceramide and diacylglycerol accumulation in 3T3-L1 adipocytes and C2C12 myotubes. Arch Biochem Biophys. 2003;419(2):101-9.
105. Amati F, Dubé JJ, Alvarez-Carnero E, Edreira MM, Chomentowski P, Coen PM, et al. Skeletal Muscle Triglycerides, Diacylglycerols, and Ceramides in Insulin Resistance Another Paradox in Endurance-Trained Athletes? Diabetes. 2011;60(10):2588-97.
106. Zechner R, Kienesberger PC, Haemmerle G, Zimmermann R, Lass A. Adipose triglyceride lipase and the lipolytic catabolism of cellular fat stores. J Lipid Res. 2009;50(1):3-21.
107. Jenkins CM, Mancuso DJ, Yan W, Sims HF, Gibson B, Gross RW. Identification, cloning, expression, and purification of three novel human calcium-independent phospholipase A2 family members possessing triacylglycerol lipase and acylglycerol transacylase activities. J Biol Chem. 2004;279(47):48968-75.
108. Zhang X, Zhang CC, Yang H, Soni KG, Wang SP, Mitchell GA, Wu JW. An Epistatic Interaction between Pnpla2 and Lipe Reveals New Pathways of Adipose Tissue Lipolysis. Cells. 2019;8(5).
109. Brejchova K, Radner FPW, Balas L, Paluchova V, Cajka T, Chodounska H, et al. Distinct roles of adipose triglyceride lipase and hormone-sensitive lipase in the catabolism of triacylglycerol estolides. Proc Natl Acad Sci U S A. 2021;118(2).
110. Fischer J, Lefevre C, Morava E, Mussini JM, Laforet P, Negre-Salvayre A, et al. The gene encoding adipose triglyceride lipase (PNPLA2) is mutated in neutral lipid storage disease with myopathy. Nat Genet. 2007;39(1):28-30.

111. Haemmerle G, Moustafa T, Woelkart G, Buttner S, Schmidt A, van de Weijer T, et al. ATGL-mediated fat catabolism regulates cardiac mitochondrial function via PPAR-alpha and PGC-1. Nat Med. 2011;17(9):1076-85.
112. Haemmerle G, Lass A, Zimmermann R, Gorkiewicz G, Meyer C, Rozman J, et al. Defective lipolysis and altered energy metabolism in mice lacking adipose triglyceride lipase. Science. 2006;312(5774):734-7.
113. Biswas D, Ghosh M, Kumar S, Chakrabarti P. PPARalpha-ATGL pathway improves muscle mitochondrial metabolism: implication in aging. FASEB J. 2016;30(11):3822-34.
114. Meex RC, Hoy AJ, Mason RM, Martin SD, McGee SL, Bruce CR, Watt MJ. ATGL-mediated triglyceride turnover and the regulation of mitochondrial capacity in skeletal muscle. Am J Physiol Endocrinol Metab. 2015;308(11):E960-70.
115. Turnbull PC, Longo AB, Ramos SV, Roy BD, Ward WE, Peters SJ. Increases in skeletal muscle ATGL and its inhibitor G0S2 following 8 weeks of endurance training in metabolically different rat skeletal muscles. Am J Physiol Regul Integr Comp Physiol. 2016;310(2):R125-33.
116. Lass A, Zimmermann R, Haemmerle G, Riederer M, Schoiswohl G, Schweiger M, et al. Adipose triglyceride lipase-mediated lipolysis of cellular fat stores is activated by CGI-58 and defective in Chanarin-Dorfman Syndrome. Cell Metab. 2006;3(5):309-19.
117. Badin PM, Loubiere C, Coonen M, Louche K, Tavernier G, Bourlier V, et al. Regulation of skeletal muscle lipolysis and oxidative metabolism by the co-lipase CGI-58. J Lipid Res. 2012;53(5):839-48.
118. Nur BG, Gencpinar P, Yuzbasioglu A, Emre SD, Mihci E. Chanarin-Dorfman syndrome: Genotype-Phenotype Correlation. Eur J Med Genet. 2015;58(4):238-42.
119. Xie P, Kadegowda AK, Ma Y, Guo F, Han X, Wang M, et al. Muscle-specific deletion of comparative gene identification-58 (CGI-58) causes muscle steatosis but improves insulin sensitivity in male mice. Endocrinology. 2015;156(5):1648-58.
120. Recazens E, Mouisel E, Langin D. Hormone-sensitive lipase: sixty years later. Prog Lipid Res. 2021;82:101084.
121. Albert JS, Yerges-Armstrong LM, Horenstein RB, Pollin TI, Sreenivasan UT, Chai S, et al. Null mutation in hormone-sensitive lipase gene and risk of type 2 diabetes. N Engl J Med. 2014;370(24):2307-15.
122. Grabner GF, Xie H, Schweiger M, Zechner R. Lipolysis: cellular mechanisms for lipid mobilization from fat stores. Nat Metab. 2021;3(11):1445-65.
123. Morigny P, Houssier M, Mairal A, Ghilain C, Mouisel E, Benhamed F, et al. Interaction between hormone-sensitive lipase and ChREBP in fat cells controls insulin sensitivity. Nature Metabolism. 2019;1(1):133-46.

124. Zimmermann R, Haemmerle G, Wagner EM, Strauss JG, Kratky D, Zechner R. Decreased fatty acid esterification compensates for the reduced lipolytic activity in hormone-sensitive lipase-deficient white adipose tissue. J Lipid Res. 2003;44(11):2089-99.
125. Mottillo EP, Bloch AE, Leff T, Granneman JG. Lipolytic products activate peroxisome proliferator-activated receptor (PPAR) alpha and delta in brown adipocytes to match fatty acid oxidation with supply. J Biol Chem. 2012;287(30):25038-48.
126. Haemmerle G, Zimmermann R, Hayn M, Theussl C, Waeg G, Wagner E, et al. Hormone-sensitive lipase deficiency in mice causes diglyceride accumulation in adipose tissue, muscle, and testis. J Biol Chem. 2002;277(7):4806-15.
127. Savinainen JR, Kansanen E, Pantsar T, Navia-Paldanius D, Parkkari T, Lehtonen M, et al. Robust hydrolysis of prostaglandin glycerol esters by human monoacylglycerol lipase (MAGL). Mol Pharmacol. 2014;86(5):522-35.
128. Grabner GF, Zimmermann R, Schicho R, Taschler U. Monoglyceride lipase as a drug target: At the crossroads of arachidonic acid metabolism and endocannabinoid signaling. Pharmacol Therapeut. 2017;175:35-46.
129. Heier C, Taschler U, Radulovic M, Aschauer P, Eichmann TO, Grond S, et al. Monoacylglycerol Lipases Act as Evolutionarily Conserved Regulators of Non-oxidative Ethanol Metabolism. Journal of Biological Chemistry. 2016;291(22):11865-75.
130. Douglass JD, Zhou YX, Wu A, Zadroga JA, Gajda AM, Lackey AI, et al. Global deletion of MGL in mice delays lipid absorption and alters energy homeostasis and diet-induced obesity. J Lipid Res. 2015;56(6):1153-71.
131. Taschler U, Radner FP, Heier C, Schreiber R, Schweiger M, Schoiswohl G, et al. Monoglyceride lipase deficiency in mice impairs lipolysis and attenuates diet-induced insulin resistance. J Biol Chem. 2011;286(20):17467-77.
132. Vujic N, Schlager S, Eichmann TO, Madreiter-Sokolowski CT, Goeritzer M, Rainer S, et al. Monoglyceride lipase deficiency modulates endocannabinoid signaling and improves plaque stability in ApoE-knockout mice. Atherosclerosis. 2016;244:9-21.
133. Vujic N, Korbelius M, Leopold C, Duta-Mare M, Rainer S, Schlager S, et al. Monoglyceride lipase deficiency affects hepatic cholesterol metabolism and lipid-dependent gut transit in ApoE-/- mice. Oncotarget. 2017;8(20):33122-36.
134. Tardelli M, Bruschi FV, Claudel T, Fuchs CD, Auer N, Kunczer V, et al. Lack of monoacylglycerol lipase prevents hepatic steatosis by favoring lipid storage in adipose tissue and intestinal malabsorption. J Lipid Res. 2019;60(7):1284-92.

135. Lake AC, Sun Y, Li JL, Kim JE, Johnson JW, Li D, et al. Expression, regulation, and triglyceride hydrolase activity of Adiponutrin family members. J Lipid Res. 2005;46(11):2477-87.
136. Gao J, Simon M. Identification of a novel keratinocyte retinyl ester hydrolase as a transacylase and lipase. J Invest Dermatol. 2005;124(6):1259-66.
137. Zhang D, Wei Y, Huang Q, Chen Y, Zeng K, Yang W, et al. Important Hormones Regulating Lipid Metabolism. Molecules. 2022;27(20).
138. Muscella A, Stefano E, Lunetti P, Capobianco L, Marsigliante S. The Regulation of Fat Metabolism During Aerobic Exercise. Biomolecules. 2020;10(12).
139. Lundsgaard AM, Fritzen AM, Kiens B. Molecular Regulation of Fatty Acid Oxidation in Skeletal Muscle during Aerobic Exercise. Trends Endocrinol Metab. 2018;29(1):18-30.
140. Li LO, Grevengoed TJ, Paul DS, Ilkayeva O, Koves TR, Pascual F, et al. Compartmentalized acyl-CoA metabolism in skeletal muscle regulates systemic glucose homeostasis. Diabetes. 2015;64(1):23-35.
141. Wicks SE, Vandanmagsar B, Haynie KR, Fuller SE, Warfel JD, Stephens JM, et al. Impaired mitochondrial fat oxidation induces adaptive remodeling of muscle metabolism. Proc Natl Acad Sci U S A. 2015;112(25):E3300-9.
142. Sidossis LS, Gastaldelli A, Klein S, Wolfe RR. Regulation of plasma fatty acid oxidation during low- and high-intensity exercise. Am J Physiol. 1997;272(6 Pt 1):E1065-70.
143. Harper AE, Miller RH, Block KP. Branched-Chain Amino-Acid-Metabolism. Annu Rev Nutr. 1984;4:409-54.
144. Shimomura Y, Obayashi M, Murakami T, Harris RA. Regulation of branched-chain amino acid catabolism:: nutritional and hormonal regulation of activity and expression of the branched-chain α-keto acid dehydrogenase kinase. Current Opinion in Clinical Nutrition and Metabolic Care. 2001;4(5):419-23.
145. Shimomura Y, Murakami T, Nakai N, Nagasaki M, Harris RA. Exercise promotes BCAA catabolism: Effects of BCAA supplementation on skeletal muscle during exercise. Journal of Nutrition. 2004;134(6):1583s-7s.
146. Kamei Y, Hatazawa Y, Uchitomi R, Yoshimura R, Miura S. Regulation of Skeletal Muscle Function by Amino Acids. Nutrients. 2020;12(1).
147. Arnold PK, Finley LWS. Regulation and function of the mammalian tricarboxylic acid cycle. J Biol Chem. 2023;299(2):102838.
148. Laffel L. Ketone bodies: a review of physiology, pathophysiology and application of monitoring to diabetes. Diabetes-Metab Res. 1999;15(6):412-26.

149. Robinson AM, Williamson DH. Physiological Roles of Ketone-Bodies as Substrates and Signals in Mammalian-Tissues. Physiological Reviews. 1980;60(1):143-87.
150. Rommel C, Bodine SC, Clarke BA, Rossman R, Nunez L, Stitt TN, et al. Mediation of IGF-1-induced skeletal myotube hypertrophy by PI(3)K/Akt/mTOR and PI(3)K/Akt/GSK3 pathways. Nature Cell Biology. 2001;3(11):1009-13.
151. Bodine SC, Stitt TN, Gonzalez M, Kline WO, Stover GL, Bauerlein R, et al. Akt/mTOR pathway is a crucial regulator of skeletal muscle hypertrophy and can prevent muscle atrophy. Nature Cell Biology. 2001;3(11):1014-9.
152. Kubica N, Crispino JL, Gallagher JW, Kimball SR, Jefferson LS. Activation of the mammalian target of rapamycin complex 1 is both necessary and sufficient to stimulate eukaryotic initiation factor 2Bvarepsilon mRNA translation and protein synthesis. Int J Biochem Cell Biol. 2008;40(11):2522-33.
153. Sartori R, Romanello V, Sandri M. Mechanisms of muscle atrophy and hypertrophy: implications in health and disease. Nat Commun. 2021;12(1):330.
154. Murgia M, Serrano AL, Calabria E, Pallafacchina G, Lomo T, Schiaffino S. Ras is involved in nerve-activity-dependent regulation of muscle genes. Nature Cell Biology. 2000;2(3):142-7.
155. Liu GY, Sabatini DM. mTOR at the nexus of nutrition, growth, ageing and disease. Nature Reviews Molecular Cell Biology. 2020;21(4):183-203.
156. Bentzinger CF, Romanino K, Cloetta D, Lin S, Mascarenhas JB, Oliveri F, et al. Skeletal Muscle-Specific Ablation of *raptor*, but Not of *rictor*, Causes Metabolic Changes and Results in Muscle Dystrophy. Cell Metabolism. 2008;8(5):411-24.
157. Risson V, Mazelin L, Roceri M, Sanchez H, Moncollin V, Corneloup C, et al. Muscle inactivation of mTOR causes metabolic and dystrophin defects leading to severe myopathy. J Cell Biol. 2009;187(6):859-74.
158. Zhang Q, Duplany A, Moncollin V, Mouradian S, Goillot E, Mazelin L, et al. Lack of muscle mTOR kinase activity causes early onset myopathy and compromises whole-body homeostasis. J Cachexia Sarcopeni. 2019;10(1):35-53.
159. Yoshida T, Delafontaine P. Mechanisms of IGF-1-Mediated Regulation of Skeletal Muscle Hypertrophy and Atrophy. Cells. 2020;9(9).
160. Kline WO, Panaro FJ, Yang HY, Bodine SC. Rapamycin inhibits the growth and muscle-sparing effects of clenbuterol. J Appl Physiol. 2007;102(2):740-7.
161. Sartori R, Milan G, Patron M, Mammucari C, Blaauw B, Abraham R, Sandri M. Smad2 and 3 transcription factors control muscle mass in adulthood. Am J Physiol Cell Physiol. 2009;296(6):C1248-57.

162. Winbanks CE, Weeks KL, Thomson RE, Sepulveda PV, Beyer C, Qian HW, et al. Follistatin-mediated skeletal muscle hypertrophy is regulated by Smad3 and mTOR independently of myostatin. Journal of Cell Biology. 2012;197(7):997-1008.
163. McPherron AC, Lawler AM, Lee SJ. Regulation of skeletal muscle mass in mice by a new TGF-beta superfamily member. Nature. 1997;387(6628):83-90.
164. Winbanks CE, Murphy KT, Bernardo BC, Qian HW, Liu YY, Sepulveda PV, et al. gene delivery prevents muscle wasting associated with cancer cachexia in mice. Sci Transl Med. 2016;8(348).
165. Templeton TJ, Hauschka SD. Fgf-Mediated Aspects of Skeletal-Muscle Growth and Differentiation Are Controlled by a High-Affinity Receptor, Fgfr1. Developmental Biology. 1992;154(1):169-81.
166. Benoit B, Meugnier E, Castelli M, Chanon S, Vieille-Marchiset A, Durand C, et al. Fibroblast growth factor 19 regulates skeletal muscle mass and ameliorates muscle wasting in mice. Nature Medicine. 2017;23(8):990-+.
167. Oost LJ, Kustermann M, Armani A, Blaauw B, Romanello V. Fibroblast growth factor 21 controls mitophagy and muscle mass. J Cachexia Sarcopeni. 2019;10(3):630-42.
168. Ali S, Garcia JM. Sarcopenia, cachexia and aging: diagnosis, mechanisms and therapeutic options - a mini-review. Gerontology. 2014;60(4):294-305.
169. Gross DN, Wan M, Birnbaum MJ. The role of FOXO in the regulation of metabolism. Curr Diabetes Rep. 2009;9(3):208-14.
170. Milan G, Romanello V, Pescatore F, Armani A, Paik JH, Frasson L, et al. Regulation of autophagy and the ubiquitin-proteasome system by the FoxO transcriptional network during muscle atrophy. Nature Communications. 2015;6.
171. Lee D, Goldberg AL. SIRT1 Protein, by Blocking the Activities of Transcription Factors FoxO1 and FoxO3, Inhibits Muscle Atrophy and Promotes Muscle Growth. Journal of Biological Chemistry. 2013;288(42):30515-26.
172. Bois PRJ, Grosveld GC. FKHR (FOXO1a) is required for myotube fusion of primary mouse myoblasts. Embo J. 2003;22(5):1147-57.
173. Hakuno F, Yamauchi Y, Kaneko G, Yoneyama Y, Nakae J, Chida K, et al. Constitutive Expression of Insulin Receptor Substrate (IRS)-1 Inhibits Myogenic Differentiation through Nuclear Exclusion of Foxo1 in L6 Myoblasts. Plos One. 2011;6(10).
174. Bodine SC, Latres E, Baumhueter S, Lai VK, Nunez L, Clarke BA, et al. Identification of ubiquitin ligases required for skeletal muscle atrophy. Science. 2001;294(5547):1704-8.
175. Bodine SC, Baehr LM. Skeletal muscle atrophy and the E3 ubiquitin ligases MuRF1 and MAFbx/atrogin-1. Am J Physiol Endocrinol Metab. 2014;307(6):E469-84.

176. Cohen S, Nathan JA, Goldberg AL. Muscle wasting in disease: molecular mechanisms and promising therapies. Nat Rev Drug Discov. 2015;14(1):58-74.
177. Cadena SM, Zhang Y, Fang J, Brachat S, Kuss P, Giorgetti E, et al. Skeletal muscle in MuRF1 null mice is not spared in low-gravity conditions, indicating atrophy proceeds by unique mechanisms in space. Sci Rep. 2019;9(1):9397.
178. Sandri M, Barberi L, Bijlsma AY, Blaauw B, Dyar KA, Milan G, et al. Signalling pathways regulating muscle mass in ageing skeletal muscle: the role of the IGF1-Akt-mTOR-FoxO pathway. Biogerontology. 2013;14(3):303-23.
179. Hwee DT, Baehr LM, Philp A, Baar K, Bodine SC. Maintenance of muscle mass and load-induced growth in Muscle RING Finger 1 null mice with age. Aging Cell. 2014;13(1):92-101.
180. Wang Y, Pessin JE. Mechanisms for fiber-type specificity of skeletal muscle atrophy. Current Opinion in Clinical Nutrition and Metabolic Care. 2013;16(3):243-50.
181. Nigro V, Savarese M. Genetic basis of limb-girdle muscular dystrophies: the 2014 update. Acta Myol. 2014;33(1):1-12.
182. Kudryashova E, Wu J, Havton LA, Spencer MJ. Deficiency of the E3 ubiquitin ligase TRIM32 in mice leads to a myopathy with a neurogenic component. Hum Mol Genet. 2009;18(7):1353-67.
183. Di Rienzo M, Antonioli M, Fusco C, Liu Y, Mari M, Orhon I, et al. Autophagy induction in atrophic muscle cells requires ULK1 activation by TRIM32 through unanchored K63-linked polyubiquitin chains. Sci Adv. 2019;5(5).
184. Paul PK, Bhatnagar S, Mishra V, Srivastava S, Darnay BG, Choi Y, Kumar A. The E3 Ubiquitin Ligase TRAF6 Intercedes in Starvation-Induced Skeletal Muscle Atrophy through Multiple Mechanisms. Molecular and Cellular Biology. 2012;32(7):1248-59.
185. Duve CD, Pressman BC, Gianetto R, Wattiaux R, Appelmans F. Tissue Fractionation Studies .6. Intracellular Distribution Patterns of Enzymes in Rat-Liver Tissue. Biochem J. 1955;60(1-4):604-17.
186. Trivedi PC, Bartlett JJ, Pulinilkunnil T. Lysosomal Biology and Function: Modern View of Cellular Debris Bin. Cells. 2020;9(5).
187. Xu HX, Ren DJ. Lysosomal Physiology. Annu Rev Physiol. 2015;77:57-80.
188. Brozzi A, Urbanelli L, Germain PL, Magini A, Emiliani C. hLGDB: a database of human lysosomal genes and their regulation. Database-Oxford. 2013.
189. Rudnik S, Damme M. The lysosomal membrane-export of metabolites and beyond. Febs Journal. 2021;288(14):4168-82.

190. Parzych KR, Klionsky DJ. An Overview of Autophagy: Morphology, Mechanism, and Regulation. Antioxid Redox Sign. 2014;20(3):460-73.
191. Neel BA, Lin YX, Pessin JE. Skeletal muscle autophagy: a new metabolic regulator. Trends Endocrin Met. 2013;24(12):635-43.
192. Xia Q, Huang X, Huang J, Zheng Y, March ME, Li J, Wei Y. The Role of Autophagy in Skeletal Muscle Diseases. Front Physiol. 2021;12:638983.
193. Raben N, Hill V, Shea L, Takikita S, Baum R, Mizushima N, et al. Suppression of autophagy in skeletal muscle uncovers the accumulation of ubiquitinated proteins and their potential role in muscle damage in Pompe disease. Human Molecular Genetics. 2008;17(24):3897-908.
194. Nemazanyy I, Blaauw B, Paolini C, Caillaud C, Protasi F, Mueller A, et al. Defects of Vps15 in skeletal muscles lead to autophagic vacuolar myopathy and lysosomal disease. Embo Mol Med. 2013;5(6):870-90.
195. Fuqua JD, Mere CP, Kronemberger A, Blomme J, Bae D, Turner KD, et al. ULK2 is essential for degradation of ubiquitinated protein aggregates and homeostasis in skeletal muscle. Faseb Journal. 2019;33(11):11735-45.
196. Bujak AL, Crane JD, Lally JS, Ford RJ, Kang SJ, Rebalka IA, et al. AMPK Activation of Muscle Autophagy Prevents Fasting-Induced Hypoglycemia and Myopathy during Aging. Cell Metabolism. 2015;21(6):883-90.
197. Castets P, Lin S, Rion N, Di Fulvio S, Romanino K, Guridi M, et al. Sustained Activation of mTORC1 in Skeletal Muscle Inhibits Constitutive and Starvation-Induced Autophagy and Causes a Severe, Late-Onset Myopathy. Cell Metabolism. 2013;17(5):731-44.
198. Carnio S, LoVerso F, Baraibar MA, Longa E, Khan MM, Maffei M, et al. Autophagy Impairment in Muscle Induces Neuromuscular Junction Degeneration and Precocious Aging. Cell Reports. 2014;8(5):1509-21.
199. Malicdan MC, Noguchi S, Nonaka I, Saftig P, Nishino I. Lysosomal myopathies: An excessive build-up in autophagosomes is too much to handle. Neuromuscular Disord. 2008;18(7):521-9.
200. Ryu D, Mouchiroud L, Andreux PA, Katsyuba E, Moullan N, Nicolet-dit-Félix AA, et al. Urolithin A induces mitophagy and prolongs lifespan in *C. elegans* and increases muscle function in rodents. Nature Medicine. 2016;22(8):879-+.
201. Zechner R, Madeo F, Kratky D. Cytosolic lipolysis and lipophagy: Two sides of the same coin. Nature Reviews Molecular Cell Biology. 2017;18(11):671-84.

202. Ameis D, Merkel M, Eckerskorn C, Greten H. Purification, characterization and molecular cloning of human hepatic lysosomal acid lipase. European Journal of Biochemistry. 1994;219(3):905-14.
203. Sando GN, Rosenbaum LM. Human lysosomal acid lipase/cholesteryl ester hydrolase. Purification and properties of the form secreted by fibroblasts in microcarrier culture. Journal of Biological Chemistry. 1985;260(28):15186-93.
204. Kaisto T, Rahkila P, Marjomäki V, Parton RG, Metsikkö K. Endocytosis in skeletal muscle fibers. Experimental Cell Research. 1999;253(2):551-60.
205. Grant BD, Donaldson JG. Pathways and mechanisms of endocytic recycling. Nature Reviews Molecular Cell Biology. 2009;10(9):597-608.
206. Tuohetahuntila M, Molenaar MR, Spee B, Brouwers JF, Wubbolts R, Houweling M, et al. Lysosome-mediated degradation of a distinct pool of lipid droplets during hepatic stellate cell activation. Journal of Biological Chemistry. 2017;292(30):12436-48.
207. Rajamohan F, Reyes AR, Tu MH, Nedoma NL, Hoth LR, Schwaid AG, et al. Crystal structure of human lysosomal acid lipase and its implications in cholesteryl ester storage disease[S]. Journal of Lipid Research. 2020;61(8):1192-202.
208. Du H, Witte DP, Grabowski GA. Tissue and cellular specific expression of murine lysosomal acid lipase mRNA and protein. Journal of Lipid Research. 1996;37(5):937-49.
209. Braulke T, Bonifacino JS. Sorting of lysosomal proteins. Bba-Mol Cell Res. 2009;1793(4):605-14.
210. Roczniak-Ferguson A, Petit CS, Froehlich F, Qian S, Ky J, Angarola B, et al. The Transcription Factor TFEB Links mTORC1 Signaling to Transcriptional Control of Lysosome Homeostasis. Sci Signal. 2012;5(228).
211. Martina JA, Chen Y, Gucek M, Puertollano R. MTORC1 functions as a transcriptional regulator of autophagy by preventing nuclear transport of TFEB. Autophagy. 2012;8(6):903-14.
212. Emanuel R, Sergin I, Bhattacharya S, Turner JN, Epelman S, Settembre C, et al. Induction of Lysosomal Biogenesis in Atherosclerotic Macrophages Can Rescue Lipid-Induced Lysosomal Dysfunction and Downstream Sequelae. Arterioscl Throm Vas. 2014;34(9):1942-52.
213. Dubland JA, Francis GA. Lysosomal acid lipase: At the crossroads of normal and atherogenic cholesterol metabolism. Frontiers in Cell and Developmental Biology. 2015;3(FEB):1-11.

214. Chakrabarti P, English T, Karki S, Qiang L, Tao R, Kim J, et al. SIRT1 controls lipolysis in adipocytes via FOXO1-mediated expression of ATGL. Journal of Lipid Research. 2011;52(9):1693-701.
215. Barbato DL, Tatulli G, Aquilano K, Ciriolo MR. FoxO1 controls lysosomal acid lipase in adipocytes: implication of lipophagy during nutrient restriction and metformin treatment. Cell Death Dis. 2013;4.
216. Zhao T, Du H, Blum JS, Yan C. Critical role of PPARγ in myeloid-derived suppressor cell-stimulated cancer cell proliferation and metastasis. Oncotarget. 2016;7(2):1529-43.
217. Tan HWS, Anjum B, Shen HM, Ghosh S, Yen PM, Sinha RA. Lysosomal inhibition attenuates peroxisomal gene transcription via suppression of PPARA and PPARGC1A levels. Autophagy. 2019;15(8):1455-9.
218. Korbelius M, Kuentzel KB, Bradić I, Vujić N, Kratky D. Recent insights into lysosomal acid lipase deficiency. Trends in Molecular Medicine: Elsevier Ltd; 2023.
219. Cox BE, Griffin EE, Ullery JC, Jerome WG. Effects of cellular cholesterol loading on macrophage foam cell lysosome acidification. Journal of Lipid Research. 2007;48(5):1012-21.
220. Li W, Yuan XM, Olsson AG, Brunk UT. Uptake of oxidized LDL by macrophages results in partial lysosomal enzyme inactivation and relocation. Arterioscl Throm Vas. 1998;18(2):177-84.
221. Griffin EE, Ullery JC, Cox BE, Jerome WG. Aggregated LDL and lipid dispersions induce lysosomal cholesteryl ester accumulation in macrophage foam cells. Journal of Lipid Research. 2005;46(10):2052-60.
222. Kuentzel KB, Bradić I, Akhmetshina A, Korbelius M, Rainer S, Kolb D, et al. Defective Lysosomal Lipolysis Causes Prenatal Lipid Accumulation and Exacerbates Immediately after Birth. International Journal of Molecular Sciences. 2021;22(19):10416-.
223. Lukacs Z, Barr M, Hamilton J. Best practice in the measurement and interpretation of lysosomal acid lipase in dried blood spots using the inhibitor Lalistat 2. Clin Chim Acta. 2017;471:201-5.
224. Brown WJ, Sgoutas DS. Purification of Rat-Liver Lysosomal Cholesteryl Ester Hydrolase. Biochimica Et Biophysica Acta. 1980;617(2):305-17.
225. Muthukottiappan P, Winter D. A proteomic view on lysosomes. Mol Omics. 2021;17(6):842-59.
226. Platt FM, d'Azzo A, Davidson BL, Neufeld EF, Tifft CJ. Lysosomal storage diseases. Nat Rev Dis Primers. 2018;4.
227. Marshall WC, Ockenden BG, Fosbrooke AS, Cumings JN. Wolman's disease. A rare lipidosis with adrenal calcification. Archives of Disease in Childhood. 1969;44(235):331-41.

228. Abramov A, Schorr S, Wolman M. Generalized xanthomatosis with calcified adrenals. Archives of Pediatrics & Adolescent Medicine. 1956;91(3):282-.
229. Pericleous M, Kelly C, Wang T, Livingstone C, Ala A. Wolman's disease and cholesteryl ester storage disorder: the phenotypic spectrum of lysosomal acid lipase deficiency. The Lancet Gastroenterology & Hepatology. 2017;2(9):670-9.
230. Jones SA, Valayannopoulos V, Schneider E, Eckert S, Banikazemi M, Bialer M, et al. Rapid progression and mortality of lysosomal acid lipase deficiency presenting in infants. Genetics in Medicine. 2016;18(5):452-8.
231. Reiner Z, Guardamagna O, Nair D, Soran H, Hovingh K, Bertolini S, et al. Lysosomal acid lipase deficiency - An under-recognized cause of dyslipidaemia and liver dysfunction. Atherosclerosis. 2014;235(1):21-30.
232. Bernstein DL, Hülkova H, Bialer MG, Desnick RJ. Cholesteryl ester storage disease: Review of the findings in 135 reported patients with an underdiagnosed disease. Journal of Hepatology. 2013;58(6):1230-43.
233. Evans TD, Zhang XY, Clark RE, Alisio A, Song E, Zhang HR, et al. Functional Characterization of LIPA (Lysosomal Acid Lipase) Variants Associated With Coronary Artery Disease. Arterioscl Throm Vas. 2019;39(12):2480-91.
234. Li F, Zhang H. Lysosomal Acid Lipase in Lipid Metabolism and beyond. Arteriosclerosis, Thrombosis, and Vascular Biology. 2019;39(5):850-6.
235. Hamilton J, Jones I, Srivastava R, Galloway P. A new method for the measurement of lysosomal acid lipase in dried blood spots using the inhibitor Lalistat 2. Clin Chim Acta. 2012;413(15-16):1207-10.
236. Bradić I, Kuentzel KB, Honeder S, Grabner GF, Vujić N, Zimmermann R, et al. Off-target effects of the lysosomal acid lipase inhibitors Lalistat-1 and Lalistat-2 on neutral lipid hydrolases. Molecular Metabolism. 2022;61(April):101510-.
237. Civallero G, De Mari J, Bittar C, Burin M, Giugliani R. Extended use of a selective inhibitor of acid lipase for the diagnosis of Wolman disease and cholesteryl ester storage disease. Gene. 2014;539(1):154-6.
238. Mayanskiy N, Brzhozovskaya E, Pushkov A, Strokova T, Vlasov N, Surkov A, et al. A kinetic assay of total lipase activity for detecting lysosomal acid lipase deficiency (LAL-D) and the molecular characterization of 18 LAL-D patients from Russia. JIMD Rep. 2019;48(1):75-82.
239. Bianco V, Kratky D. Glycoprotein Non-Metastatic Protein B (GPNMB): The Missing Link Between Lysosomes and Obesity. Exp Clin Endocrinol Diabetes. 2023;131(12):639-45.

240. Sustar U, Groselj U, Podkrajsek KT, Mlinaric M, Kovac J, Thaler M, et al. Early Discovery of Children With Lysosomal Acid Lipase Deficiency With the Universal Familial Hypercholesterolemia Screening Program. Front Genet. 2022;13.
241. Fouchier SW, Defesche JC. Lysosomal acid lipase A and the hypercholesterolaemic phenotype. Current Opinion in Lipidology. 2013;24(4):332-8.
242. Yokoyama S, Mccoy E. Long-Term Treatment of a Homozygous Cholesteryl Ester Storage Disease with Combined Cholestyramine and Lovastatin. J Inherit Metab Dis. 1992;15(2):291-2.
243. Tadiboyina VT, Liu DM, Miskie BA, Wang J, Hegele RA. Treatment of dyslipidemia with lovastatin and ezetimibe in an adolescent with cholesterol ester storage disease. Lipids Health Dis. 2005;4:26.
244. Iverson SA, Cairns SR, Ward CP, Fensom AH. Asymptomatic cholesteryl ester storage disease in an adult controlled with simvastatin. Ann Clin Biochem. 1997;34:433-6.
245. Levy R, Ostlund RE, Schonfeld G, Wong P, Semenkovich CF. Cholesteryl Ester Storage Disease - Complex Molecular Effects of Chronic Lovastatin Therapy. Journal of Lipid Research. 1992;33(7):1005-15.
246. Rutkowski JV, Burt AD, Leavitt MC, Hu W, Canty D, Quinn AG. Co-localization of macrophage aggregation and fibrosis in a rat model of lysosomal acid lipase (LAL) deficiency and the effects of enzyme replacement with SBC-102. Molecular Genetics and Metabolism. 2013;108(2):S80-S1.
247. Leavitt M, Burt AD, Hu W, Canty D, Gray M, Bray A, et al. Recombinant lysosomal acid lipase normalizes liver weight, transaminases and histopathological abnormalities in an *in vivo* model of cholesteryl ester storage disease. Journal of Hepatology. 2011;54:S358-S.
248. Burton BK, Feillet F, Furuya KN, Marulkar S, Balwani M. Sebelipase alfa in children and adults with lysosomal acid lipase deficiency: Final results of the ARISE study. Journal of Hepatology. 2022;76(3):577-87.
249. Paton DM. Sebelipase Alfa: Enzymatic Replacement Treatment for Lysosomal Acid Lipase Deficiency. Drug Today. 2016;52(5):287-93.
250. Su K, Donaldson E, Sharma R. Novel treatment options for lysosomal acid lipase deficiency: critical appraisal of sebelipase alfa. Appl Clin Genet. 2016;9:157-67.
251. Malinová V, Balwani M, Sharma R, Arnoux JB, Kane J, Whitley CB, et al. Sebelipase alfa for lysosomal acid lipase deficiency: 5-year treatment experience from a phase 2 open-label extension study. Liver Int. 2020;40(9):2203-14.

252. Balwani M, Breen C, Enns GM, Deegan PB, Honzík T, Jones S, et al. Clinical Effect and Safety Profile of Recombinant Human Lysosomal Acid Lipase in Patients With Cholesteryl Ester Storage Disease. Hepatology. 2013;58(3):950-7.
253. Yoshida H, Kuriyama M. Genetic Lipid Storage Disease with Lysosomal Acid Lipase Deficiency in Rats. Lab Anim Sci. 1990;40(5):486-9.
254. Du H, Duanmu M, Witte D, Grabowski GA. Targeted disruption of the mouse lysosomal acid lipase gene: Long-term survival with massive cholesteryl ester and triglyceride storage. Human Molecular Genetics. 1998;7(9):1347-54.
255. Koch G, Lalley PA, Mcavoy M, Shows TB. Assignment of Lipa, Associated with Human Acid Lipase Deficiency, to Human Chromosome-10 and Comparative Assignment to Mouse Chromosome-19. Somat Cell Genet. 1981;7(3):345-58.
256. Du H, Heur M, Duanmu M, Grabowski GA, Hui DY, Witte DP, Mishra J. Lysosomal acid lipase-deficient mice: Depletion of white and brown fat, severe hepatosplenomegaly, and shortened life span. Journal of Lipid Research. 2001;42(4):489-500.
257. Lam P, Ashbrook A, Zygmunt DA, Yan C, Du H, Martin PT. Therapeutic efficacy of rscAAVrh74.miniCMV. *LIPA* gene therapy in a mouse model of lysosomal acid lipase deficiency. Mol Ther-Meth Clin D. 2022;26:413-26.
258. Leopold C, Duta-Mare M, Sachdev V, Goeritzer M, Maresch LK, Kolb D, et al. Hepatocyte-specific lysosomal acid lipase deficiency protects mice from diet-induced obesity but promotes hepatic inflammation. Biochimica et Biophysica Acta (BBA) - Molecular and Cell Biology of Lipids. 2019;1864(4):500-11.
259. Bianco V, Korbelius M, Vujic N, Akhmetshina A, Amor M, Kolb D, et al. Impact of (intestinal) LAL deficiency on lipid metabolism and macrophage infiltration. Molecular Metabolism. 2023;73:101737-.
260. Sachdev V, Duta-Mare M, Korbelius M, Vujić N, Leopold C, Freark de Boer J, et al. Impaired Bile Acid Metabolism and Gut Dysbiosis in Mice Lacking Lysosomal Acid Lipase. Cells. 2021;10(10):2619-.
261. Lian X, Yan C, Yang L, Xu Y, Du H. Lysosomal acid lipase deficiency causes respiratory inflammation and destruction in the lung. American Journal of Physiology - Lung Cellular and Molecular Physiology. 2004;286(4 30-4):801-7.
262. Duta-Mare M, Sachdev V, Leopold C, Kolb D, Vujic N, Korbelius M, et al. Lysosomal acid lipase regulates fatty acid channeling in brown adipose tissue to maintain thermogenesis. Biochimica et Biophysica Acta - Molecular and Cell Biology of Lipids. 2018;1863(4):467-78.

263. Radović B, Vujić N, Leopold C, Schlager S, Goeritzer M, Patankar JV, et al. Lysosomal acid lipase regulates VLDL synthesis and insulin sensitivity in mice. Diabetologia. 2016;59(8):1743-52.
264. Crocker AC, Vawter GF, Neuhauser EBD, Rosowsky A. Wolman's disease: three new patients with a recently described lipidosis. Pediatrics. 1965;35(4):627-40.
265. Schaub J, Janka GE, Christomanou H, Sandhoff K, Permanetter W, Huebner G, Meister P. Wolman's disease: Clinical, biochemical and ultrastructural studies in an unusual case without striking adrenal calcification. European Journal of Pediatrics. 1980;135(1):45-53.
266. Meyers WF, Hoeg JM, Demosky SJ, Herbst JJ, Brewer HB. The use of parenteral hyperalimentation and elemental formula feeding in the treatment of Wolman disease. Nutrition Research. 1985;5(4):423-9.
267. Mandadzhieva A, Avdzhieva-Tzavella D, Todorov T, Tincheva S, Sinigerska V, Ivanova M, et al. Wolman Disease in Bulgarian Patients: Selective Genetic Screening in Two Presumable Endemic Regions. American Journal of Molecular Biology. 2017;07(04):1047-53.
268. Alabbas F, Elyamany G, Alanzi T, Ali TB, Albatniji F, Alfaraidi H. Wolman's disease presenting with secondary hemophagocytic lymphohistiocytosis: a case report from Saudi Arabia and literature review. BMC Pediatrics. 2021;21(1):72-.
269. Akhmetshina A, Bianco V, Bradic I, Korbelius M, Pirchheim A, Kuentzel KB, et al. Loss of lysosomal acid lipase results in mitochondrial dysfunction and fiber switch in skeletal muscles of mice. Mol Metab. 2024;79:101869.
270. Bresilla D, Habisch H, Pritišanac I, Zarse K, Parichatikanond W, Ristow M, et al. The sex-specific metabolic signature of C57BL/6NRj mice during aging. Scientific Reports. 2022;12(1):21050-.
271. Dieterle F, Ross A, Schlotterbeck G, Senn H. Probabilistic quotient normalization as robust method to account for dilution of complex biological mixtures. Application in 1H NMR metabonomics. Anal Chem. 2006;78(13):4281-90.
272. Pang Z, Chong J, Zhou G, de Lima Morais DA, Chang L, Barrette M, et al. MetaboAnalyst 5.0: narrowing the gap between raw spectra and functional insights. Nucleic Acids Res. 2021;49(W1):W388-W96.
273. Matyash V, Liebisch G, Kurzchalia TV, Shevchenko A, Schwudke D. Lipid extraction by methyl-terf-butyl ether for high-throughput lipidomics. Journal of Lipid Research. 2008;49(5):1137-46.
274. Doerrier C, Garcia-Souza LF, Krumschnabel G, Wohlfarter Y, Mészáros AT, Gnaiger E. High-Resolution FluoRespirometry and OXPHOS Protocols for Human Cells, Permeabilized

Fibers from Small Biopsies of Muscle, and Isolated Mitochondria. Methods in molecular biology (Clifton, NJ). 2018;1782:31-70.
275. Quiros PM, Goyal A, Jha P, Auwerx J. Analysis of mtDNA/nDNA Ratio in Mice. Current protocols in mouse biology. 2017;7(1):47-54.
276. Meier F, Brunner AD, Frank M, Ha A, Bludau I, Voytik E, et al. diaPASEF: parallel accumulation–serial fragmentation combined with data-independent acquisition. Nature Methods. 2020;17(12):1229-36.
277. Demichev V, Messner CB, Vernardis SI, Lilley KS, Ralser M. DIA-NN: neural networks and interference correction enable deep proteome coverage in high throughput. Nature Methods. 2020;17(1):41-4.
278. Demichev V, Szyrwiel L, Yu F, Teo GC, Rosenberger G, Niewienda A, et al. dia-PASEF data analysis using FragPipe and DIA-NN for deep proteomics of low sample amounts. Nature Communications. 2022;13(1).
279. Thomas PD, Ebert D, Muruganujan A, Mushayahama T, Albou LP, Mi H. <scp>PANTHER</scp> : Making genome-scale phylogenetics accessible to all. Protein Science. 2022;31(1):8-22.
280. Mi H, Muruganujan A, Casagrande JT, Thomas PD. Large-scale gene function analysis with the panther classification system. Nature Protocols. 2013;8(8):1551-66.
281. Putten MV, Aartsma-Rus a, Louvain L. The use of hanging wire tests to monitor muscle strength and condition over time. Treat-NmdEu. 2012(Id):1-12.
282. Schweiger M, Eichmann TO, Taschler U, Zimmermann R, Zechner R, Lass A. Measurement of lipolysis. Methods Enzymol. 2014;538:171-93.
283. Korbelius M, Vujic N, Sachdev V, Obrowsky S, Rainer S, Gottschalk B, et al. ATGL/CGI-58-Dependent Hydrolysis of a Lipid Storage Pool in Murine Enterocytes. Cell Rep. 2019;28(7):1923-34 e4.
284. Gu X, Ma Y, Liu Y, Wan Q. Measurement of mitochondrial respiration in adherent cells by Seahorse XF96 Cell Mito Stress Test. STAR Protoc. 2021;2(1):100245.
285. Sartorelli V, Fulco M. Molecular and Cellular Determinants of Skeletal Muscle Atrophy and Hypertrophy. Science's STKE. 2004;2004(244).
286. Bonaldo P, Sandri M. Cellular and molecular mechanisms of muscle atrophy. Disease Models & Mechanisms. 2013;6(1):25-39.
287. Glass DJ. Molecular mechanisms modulating muscle mass. Trends in Molecular Medicine. 2003;9(8):344-50.
288. Glass DJ. Signalling pathways that mediate skeletal muscle hypertrophy and atrophy. Nature Cell Biology. 2003;5(2):87-90.

289. Zhang P, Chen X, Fan M. Signaling mechanisms involved in disuse muscle atrophy. Medical Hypotheses. 2007;69(2):310-21.
290. Thomson DM. The Role of AMPK in the Regulation of Skeletal Muscle Size, Hypertrophy, and Regeneration. International Journal of Molecular Sciences. 2018;19(10).
291. Fujita S, Volpi E. Amino acids and muscle loss with aging. J Nutr. 2006;136(1 Suppl):277S-80S.
292. Casas M, Buvinic S, Jaimovich E. ATP signaling in skeletal muscle: from fiber plasticity to regulation of metabolism. Exerc Sport Sci Rev. 2014;42(3):110-6.
293. Zhao T, Liu S, Hanna NH, Jalal S, Ding X, Wan J, et al. LAL deficiency induced myeloid-derived suppressor cells as targets and biomarkers for lung cancer. J Immunother Cancer. 2023;11(3).
294. Schlager S, Vujic N, Korbelius M, Duta-Mare M, Dorow J, Leopold C, et al. Lysosomal lipid hydrolysis provides substrates for lipid mediator synthesis in murine macrophages. Oncotarget. 2017;8(25):40037-51.
295. Bradic I, Liesinger L, Kuentzel KB, Vujic N, Trauner M, Birner-Gruenberger R, Kratky D. Metabolic changes and propensity for inflammation, fibrosis, and cancer in livers of mice lacking lysosomal acid lipase. J Lipid Res. 2023;64(9):100427.
296. Perez-Riverol Y, Bai J, Bandla C, García-Seisdedos D, Hewapathirana S, Kamatchinathan S, et al. The PRIDE database resources in 2022: a hub for mass spectrometry-based proteomics evidences. Nucleic Acids Research. 2022;50(D1):D543-D52.
297. Haw R, Hermjakob H, D'Eustachio P, Stein L. Reactome pathway analysis to enrich biological discovery in proteomics data sets. Proteomics. 2011;11(18):3598-613.
298. Deacon RMJ. Measuring motor coordination in mice. Journal of visualized experiments : JoVE. 2013(75):1-8.
299. Ren H, Yin P, Duan C. IGFBP-5 regulates muscle cell differentiation by binding to IGF-II and switching on the IGF-II auto-regulation loop. The Journal of Cell Biology. 2008;182(5):979-91.
300. Falcieri E, Burattini S, Ferri P, Battistelli M, Curci R, Luchetti F, Falcieri° E. C2C12 murine myoblasts as a model of skeletal muscle development: morpho-functional characterization. 2004.
301. Burton BK, Deegan PB, Enns GM, Guardamagna O, Horslen S, Hovingh GK, et al. Clinical Features of Lysosomal Acid Lipase Deficiency. Journal of Pediatric Gastroenterology and Nutrition. 2015;61(6):619-25.
302. Aqul A, Lopez AM, Posey KS, Taylor AM, Repa JJ, Burns DK, Turley SD. Hepatic entrapment of esterified cholesterol drives continual expansion of whole body sterol pool in

lysosomal acid lipase-deficient mice. American Journal of Physiology-Gastrointestinal and Liver Physiology. 2014;307(8):G836-G47.
303. Lecker SH, Jagoe RT, Gilbert A, Gomes M, Baracos V, Bailey J, et al. Multiple types of skeletal muscle atrophy involve a common program of changes in gene expression. The FASEB Journal. 2004;18(1):39-51.
304. James PL, Stewart CE, Rotwein P. Insulin-like growth factor binding protein-5 modulates muscle differentiation through an insulin-like growth factor-dependent mechanism. The Journal of cell biology. 1996;133(3):683-93.
305. Mukherjee A, Wilson EM, Rotwein P. Insulin-Like Growth Factor (IGF) Binding Protein-5 Blocks Skeletal Muscle Differentiation by Inhibiting IGF Actions. Molecular Endocrinology. 2008;22(1):206-15.
306. Felig P, Owen OE, Wahren J, Cahill GF, Jr. Amino acid metabolism during prolonged starvation. J Clin Invest. 1969;48(3):584-94.
307. Yoo HC, Yu YC, Sung Y, Han JM. Glutamine reliance in cell metabolism. Exp Mol Med. 2020;52(9):1496-516.
308. Matthews DE, Marano MA, Campbell RG. Splanchnic Bed Utilization of Glutamine and Glutamic-Acid in Humans. American Journal of Physiology. 1993;264(6):E848-E54.
309. Felig P. The glucose-alanine cycle. Metabolism. 1973;22(2):179-207.
310. Jadhao SB, Yang RZ, Lin Q, Hu H, Anania FA, Shuldiner AR, Gong DW. Murine alanine aminotransferase: cDNA cloning, functional expression, and differential gene regulation in mouse fatty liver. Hepatology. 2004;39(5):1297-302.
311. Giesbertz P, Padberg I, Rein D, Ecker J, Hofle AS, Spanier B, Daniel H. Metabolite profiling in plasma and tissues of ob/ob and db/db mice identifies novel markers of obesity and type 2 diabetes. Diabetologia. 2015;58(9):2133-43.
312. Martins-Bach AB, Bloise AC, Vainzof M, Rabbani SR. Metabolic profile of dystrophic mouse muscles analyzed with in vitro magnetic resonance spectroscopy (MRS). Magn Reson Imaging. 2012;30(8):1167-76.
313. Fazelzadeh P, Hangelbroek RWJ, Tieland M, de Groot LCPGM, Verdijk LB, van Loon LJC, et al. The Muscle Metabolome Differs between Healthy and Frail Older Adults. J Proteome Res. 2016;15(2):499-509.
314. Wang WW, Wu ZL, Dai ZL, Yang Y, Wang JJ, Wu GY. Glycine metabolism in animals and humans: implications for nutrition and health. Amino Acids. 2013;45(3):463-77.
315. Kelly B, Pearce EL. Amino Assests: How Amino Acids Support Immunity. Cell Metabolism. 2020;32(2):154-75.

316. Ye ZH, Wang SY, Zhang CM, Zhao Y. Coordinated Modulation of Energy Metabolism and Inflammation by Branched-Chain Amino Acids and Fatty Acids. Frontiers in Endocrinology. 2020;11.
317. Newgard CB. Metabolomics and Metabolic Diseases: Where Do We Stand? Cell Metabolism. 2017;25(1):43-56.
318. Ling ZN, Jiang YF, Ru JN, Lu JH, Ding B, Wu J. Amino acid metabolism in health and disease. Signal Transduct Target Ther. 2023;8(1):345.
319. Kjobsted R, Hingst JR, Fentz J, Foretz M, Sanz MN, Pehmoller C, et al. AMPK in skeletal muscle function and metabolism. Faseb Journal. 2018;32(4):1741-77.
320. Liu T, Zhang LY, Joo D, Sun SC. NF-κB signaling in inflammation. Signal Transduct Tar. 2017;2.
321. Donadelli R, Abbate M, Zanchi C, Corna D, Tomasoni S, Benigni A, et al. Protein traffic activates NF-kB gene signaling and promotes MCP-1-dependent interstitial inflammation. Am J Kidney Dis. 2000;36(6):1226-41.
322. Hebert DN, Molinari M. In and out of the ER: Protein folding, quality control, degradation, and related human diseases. Physiological Reviews. 2007;87(4):1377-408.
323. Poothong J, Jang I, Kaufman RJ. Defects in Protein Folding and/or Quality Control Cause Protein Aggregation in the Endoplasmic Reticulum. 2021. p. 115-43.
324. van Wessel T, de Haan A, van der Laarse WJ, Jaspers RT. The muscle fiber type–fiber size paradox: hypertrophy or oxidative metabolism? European Journal of Applied Physiology. 2010;110(4):665-94.
325. Blaauw B, Schiaffino S, Reggiani C. Mechanisms Modulating Skeletal Muscle Phenotype. Comprehensive Physiology: Wiley; 2013. p. 1645-87.
326. Goh YQ, Cheam GX, Wang YL. Understanding Choline Bioavailability and Utilization: First Step Toward Personalizing Choline Nutrition. J Agr Food Chem. 2021;69(37):10774-89.
327. Gallo M, Gámiz F. Choline: An Essential Nutrient for Human Health. Nutrients. 2023;15(13).
328. Perim P, Marticorena FM, Ribeiro F, Barreto G, Gobbi N, Kerksick C, et al. Can the Skeletal Muscle Carnosine Response to Beta-Alanine Supplementation Be Optimized? Front Nutr. 2019;6.
329. Baguet A, Bourgois J, Vanhee L, Achten E, Derave W. Important role of muscle carnosine in rowing performance. J Appl Physiol. 2010;109(4):1096-101.
330. Honda Y, Kuriyama M, Higachi I, Fujiyama J, Yoshida H, Osame M. Muscular involvement in lysosomal acid lipase deficiency in rats. Journal of the Neurological Sciences. 1992;108(2):189-95.

331. Li L, Wang X. The relationship between cholesterol metabolism and mitochondrial function in chronic obstructive pulmonary diseases. Clinical and Translational Discovery. 2022;2(3).
332. Jundi B, Ahmed H, Reece J, Geraghty P. The Relationship of Cholesterol Responses to Mitochondrial Dysfunction and Lung Inflammation in Chronic Obstructive Pulmonary Disease. Medicina. 2023;59(2):253-.
333. Migliavacca E, Tay SKH, Patel HP, Sonntag T, Civiletto G, McFarlane C, et al. Mitochondrial oxidative capacity and NAD+ biosynthesis are reduced in human sarcopenia across ethnicities. Nature Communications. 2019;10(1):5808-.
334. Hui X, Zhu W, Wang Y, Lam KSL, Zhang J, Wu D, et al. Major urinary protein-1 increases energy expenditure and improves glucose intolerance through enhancing mitochondrial function in skeletal muscle of diabetic mice. The Journal of biological chemistry. 2009;284(21):14050-7.
335. Patel HJ, Patel BM. TNF-α and cancer cachexia: Molecular insights and clinical implications. Life Sciences. 2017;170:56-63.
336. Chen JL, Walton KL, Winbanks CE, Murphy KT, Thomson RE, Makanji Y, et al. Elevated expression of activins promotes muscle wasting and cachexia. Faseb Journal. 2014;28(4):1711-23.
337. Ji YA, Li M, Chang MY, Liu RQ, Qiu JY, Wang KX, et al. Inflammation: Roles in Skeletal Muscle Atrophy. Antioxidants-Basel. 2022;11(9).
338. Shen YT, Li M, Wang KX, Qi GD, Liu H, Wang W, et al. Diabetic Muscular Atrophy: Molecular Mechanisms and Promising Therapies. Frontiers in Endocrinology. 2022;13.
339. Bassil MS, Gougeon R. Muscle protein anabolism in type 2 diabetes. Current Opinion in Clinical Nutrition and Metabolic Care. 2013;16(1):83-8.
340. Hansen MJ, Chen H, Jones JE, Langenbach SY, Vlahos R, Gualano RC, et al. The Lung Inflammation and Skeletal Muscle Wasting Induced by Subchronic Cigarette Smoke Exposure Are Not Altered by a High-Fat Diet in Mice. Plos One. 2013;8(11).
341. Langen RCJ, Schols AMWJ, Kelders MCJM, van der Velden JLJ, Wouters EFM, Janssen-Heininger YMW. Muscle wasting and impaired muscle regeneration in a murine model of chronic pulmonary inflammation. Am J Resp Cell Mol. 2006;35(6):689-96.
342. Bayol S, Loughna PT, Brownson C. Phenotypic Expression of IGF Binding Protein Transcripts in Muscle, in Vitro and in Vivo. Biochemical and Biophysical Research Communications. 2000;273(1):282-6.

7. Appendix

7.1 Permissions granted by the publishers to use their figures in this doctoral thesis

Figure number	Licensed content publisher and granted license number
Figures 7-10, 13-16, 18, 20-43 (parts or complete figure)	Permission is not required; the article is available under the terms of the Creative Commons Attribution License (CC BY 4.0) and I am free to share and adapt the material(https://creativecommons.org/licenses/by/4.0/). The article is available under DOI: 10.1016/j.molmet.2023.101869

Note: Detailed PDF copies of the license documents will be furbished upon request.

7.2 List of Figures

7.3 List of Tables